Masterarbeit

An Ion Microscope for spatially resolved Rydberg Atom Detection

Thomas Dieterle

November 2, 2017

Hauptberichter: Prof. Dr. Tilman Pfau
Mitberichter: Prof. Dr. Gert Denninger
5. Physikalisches Institut
Universität Stuttgart

Declaration

I hereby declare that this thesis is my own work and that, to the best of my knowledge and belief, it contains no material previously published or written by another person, except where due acknowledgement has been made.

place date signature

Zusammenfassung

Im Rahmen dieser Arbeit wurde ein Ionenmikroskop entwickelt und mithilfe von Simulationen charakterisiert. Das Mikroskop wird in ein Experiment zur Erzeugung und Untersuchung ultrakalter Rydbergatome integriert. Bei Rydbergatomen handelt es sich um Atome, bei denen sich mindestens ein Elektron in einem Zustand mit hoher Hauptquantenzahl befindet [Gal05]. Die Detektion von Rydbergatomen kann zum Beispiel über die Abnahme der Grundzustandsbesetzung oder durch Rückumwandlung der Rydbergpopulation in den detektierbaren Grundzustand erfolgen [Sch+15]. Die häufigste Methode Rydbergatome zu detektieren ist jedoch, diese zu ionisieren und die entstandenen Ionen auf einer Mikrokanalplatte (MCP) zeitaufgelöst zu messen. Durch Hinzufügen eines Phosphor-Schirms oder eines *Delay Line Detektors* hinter der MCP können die Ionen zusätzlich ortsaufgelöst detektiert werden. Die Auflösung solcher Delay Line Detektoren beträgt 50 bis 100 µm. Die für Rydbergphysik typische Größenskala liegt allerdings im Bereich von wenigen hundert Nanometern bis zu einigen Mikrometern. Deshalb wurde in dieser Arbeit ein Ionenmikroskop entwickelt, um so die ortsaufgelöste Beobachtung dieser Rydbergphysik zu ermöglichen.

Der Hauptteil dieser Arbeit bestand in der Entwicklung und der Charakterisierung des Ionenmikroskops. Wichtigstes Hilfsmittel war dabei ein Programm zur Simulation von Elektron- und Ionenoptiken. Die Erweiterung dieses Programms um einen selbstgeschriebenen, leistungsfähigen Algorithmus erlaubte es, unter einer Vielzahl von Geometrien und aus einem weiten Parameterbereich die optimale Geometrie zusammen mit den optimalen Betriebsparametern herauszufinden. Das endgültige Design des Ionenmikroskops besteht aus drei elektrostatischen Linsen mit Innendurchmessern von 8.6 mm, 10 mm und 30 mm, welche durch Driftrohre miteinander verbunden sind. Die Abbildung erfolgt dabei über zwei Zwischenbilder, welche dann jeweils weiter vergrößert werden. Es wurde durch Simulationen gezeigt, dass chromatische Aberrationen, welche die endgültige Auflösung der Abbildung limitieren, durch geeignete Wahl der Zwischenbildpositionen kompensiert werden können. Dadurch ist es möglich, in einem Bereich von Vergrößerungen zwischen 80 und 1250 scharfe Abbildungen zu erstellen.

In den Simulationen wurden außerdem mechanische Asymmetrien sowie Versätze einzelner Linsenzylinder und gesamter Linsen und Spannungsrauschen durch die Netzgeräte berücksichtigt. Durch Simulation des Spannungsrauschens konnten die Anforderungen an die benötigten Netzgeräte ermittelt werden. Es wurde gezeigt, dass laterale Versätze von Linsenzylindern zu Strahlversätzen und Aberrationen führen, weshalb nach jeder Linse vier zylindrische Deflektorplatten entwickelt wurden, um Strahlversätze sowie Versätze einzelner Linsen zueinander, welche bei der Montage entstehen können, zu kompensieren.

Es wurde weiterhin das tatsächliche mechanische Design des Ionenmikroskops mithilfe eines 3D-CAD-Konstruktionsprogramms erstellt. Die einzelnen Linsen werden dabei unabhängig voneinander gehaltert und über Driftrohre miteinander verbunden. Um die erforderlichen Konzentrizitäten der Linsenzylinder zueinander zu gewährleisten, wurde eine Kugellagerung mit jeweils drei hochpräzisen Keramikkugeln gewählt, die sowohl den Abstand zwischen zwei Zylindern als auch deren Ausrichtung zueinander festlegen.

Es wurde ein Prototyp einer elektrostatischen Linse in der fakultätseigenen Mechanik-

werkstatt gefertigt und mit einem 3D-Koordinatenmessgerät vermessen. Dies ergab, dass die Fertigung präzise genug ist, um die in Simulationen ermittelten Anforderungen zu erfüllen.
Der nächste Schritt besteht nun im Zusammenbau und der experimentellen Charakterisierung des Ionenmikroskops.

Contents

List of Figures

List of Tables

1. Introduction

The invention of laser-cooling of atoms in the second half of the past century opened the way to a whole new field of ultracold atomic physics: the study of dilute quantum gases [KDS99; KZ08]. Starting from its early days where atoms could be cooled to temperatures on the order of 1 K by the usage of Zeeman slowers [PPM82] and optical molasses to enter the microkelvin regime [DC89], improvements and new techniques of laser cooling governed the research field of atomic physics for many more years. Magneto-optical trapping allowed scientists not only to cool atoms but to trap them at temperatures well in the microkelvin regime. In 1995, with the development of evaporative cooling in magnetic traps, the first Bose-Einstein condensates of rubidium and sodium, respectively, could be observed at the University of Colorado [And+95] and at MIT [Dav+95]. Today, not just alkali atoms have been cooled to degeneracy but also alkaline earth metals, chromium, helium and the lanthanides dysprosium, erbium and ytterbium to study quantum many body physics, Bose-Hubbard physics or dipolar many body physics. Quantum degeneracy was not only achieved for bosons but also for fermions and various techniques to study the properties and interactions of ultracold gases have been established.

One system that earned considerable interest in the past years is the excitation of Rydberg atoms in ultracold gases. Rydberg atoms are atoms with at least one electron in a state with high principal quantum number [Gal05]. They are used to study many-body quantum physics [Bal+13; Kar+15; Sch+16; Cam+17], for quantum simulation [Ber+17; Lab+16], quantum information processing [SWM10] or quantum optics [Gor+14; Pey+12]. Furthermore, Rydberg atoms allow for the creation of Rydberg molecules where at least one neutral atom sits within the orbit of a Rydberg electron. These Rydberg molecules were first predicted by Greene, Dickinson and Sadeghpour in the year 2000 [GDS00] and were first observed in Stuttgart by Bendkowsky et al. [Ben+09].

The advent of laser cooling not just enabled the cooling of atoms but also made it possible to manipulate the internal and external degrees of freedom of trapped ions [Lei+03]. The trapping of ions is most commonly realized with Paul traps making use of radio-frequency electric quadrupole fields to trap the ion [Pau90]. The development of ion trapping techniques was awarded the Nobel Prize in Physics in 1989 [Pau90; Deh90] and 2012 [Win13].

With the ability to provide cold atoms as well as cold ions, interaction between both species have been studied extensively. So far, substantial work has been done in the cold, but essentially classical regime in hybrid ion-atom traps. These traps combine a Paul trap for the ion with an optical and/or a magnetic trap for the atoms. Hybrid ion-atom traps were used to study elastic and inelastic collisions for various ion-atom-combinations [HH14][ZW18][Tom+17]. However, the micromotion-induced limit in the Paul trap on the minimum collision energy that can be reached [CGV12], so far prevented the study of ion-atom collisions in the ultracold, quantum regime, i. e. the S-wave collision regime. However, Rydberg molecules provide excellent starting conditions to extend the investigation of ion-atom scattering to this so far unexplored quantum regime [Sch+17]. The Rydberg molecule is photo-ionized to start the scattering event between the Rydberg ionic core and the ground state atom. To experimentally determine the relevant quantity, the

S-wave scattering length, the freely moving scattered ion of a single ultracold-scattering event is imaged onto a time- and position-sensitive single-ion detector. After many repetitions, the scattered ion-atom wavepacket can be reconstructed either in momentum space or in real space.

The most common method to image samples of ultracold atoms is absorption imaging through illumination of the atomic cloud with a resonant laser beam [KDM99]. Another common imaging method is fluorescence imaging. However, fluorescence imaging typically requires long exposure times making it feasible only in deep trapping structures like optical lattices. A non-destructive method to image a sample of ultracold atoms is for example phase-contrast imaging [Hig+05; Mep+10; KDM99] for single atom sensitivity. A major step forward in imaging cold atom samples could be achieved with “quantum gas microscopes” where a light-optical system is placed close to the atomic sample and spatial resolutions below 1 µm became possible with single-atom and single-site sensitivity in two dimensional optical lattices [Bak+09].

All of the imaging methods presented so far rely on cycling transitions where multiple photons can be scattered. However, for Rydberg atoms a direct application of these imaging techniques is aggravated. The imaging of Rydberg atoms can be either realized by detecting losses in the ground state population (indirect approach) or by transferring the Rydberg population back to the detectable ground state [Sch+15]. However, Rydberg atoms are preferably detected by ionization. The Rydberg ion is recorded with high temporal resolution using microchannel plates (MCP). For additional spatial resolution either a phosphor screen or a delay line detector (DLD) can be added. However, the spatial resolution of these delay line detectors is not high enough for investigation of Rydberg physics, especially Rydberg blockade effects, that emerge on the µm scale [SWM10].

As a consequence, ion-optical elements are necessary to magnify the ionized Rydberg atoms on the detector to overcome the resolution limit provided by the detector. With the foundations of electron optics, which had its beginning in the late 1920s, this imaging approach was facilitated. Hans Busch stated that magnetic as well as electrostatic rotationally symmetric fields focus cathode rays [Bus26; Bus27]. The possibility of an electrostatic lens as an imaging element was first put forward by Brüche [Brü30]. A comprehensive treatment of charged particle optics theory together with the principles of lens designs was given by Brüche and Scherzer in 1934 [BO34], only seven years after the birth of the charged-particle optics research field. Interest in electrostatic optics was revived around 1970 owing to increasing demands on electrostatic lenses in electron [RT90; Ers95] and mass spectrometers [Lie89]. The most prominent use of charged particle optics, however, was and still lies in electron microscopy. From its beginnings in the late 1930s with the first developments of transmission electron microscopes by Knoll and Ruska [KR32], over fundamental theorems by Scherzer [Sch47] demonstrating that correction of aberrations is possible by abandoning rotational symmetry or by introducing time-varying fields and multipole correctors, the quest for better and better resolution occupied researchers over many more decades. Today, a resolution of below 50 pm is possible at the electron microscope PICO at the research center in Jülich [ME15].

Electrostatic lenses can not only be used for electrons but also to focus massive particles such as ions and, unlike round magnetic lenses, the behavior of electrostatic lenses is independent of the particle mass. Spatially resolved detection of Rydberg atoms has been demonstrated using a field emission tip with a magnification of 300 and a resolution of up to 0.5 µm [Sch+13]. As recently demonstrated, a system of electrostatic lenses can be used as a microscope for ultracold ground state and Rydberg atoms with magnifications of up to 1000 [Ste+17].

About this thesis: This thesis reports on the design of an ion microscope consisting of three electrostatic lenses that allows to image photo-ionized Rydberg atoms with magnifications of up to 1250 and theoretical resolutions around 100 nm. In section 2 of this thesis the basic principles of charged-particle-optics are presented, different types of electrostatic lenses are introduced and the most common types of aberrations are described. In section 3 the development of the microscope design is explained. First, the experimental requirements are outlined followed by a description of the electric field control which is used to compensate electric stray fields. The focus of this section lies in the simulation process to obtain the final microscope design. In section 4 the characterization of the electric field control and the ion microscope is described. The characterization includes achievable magnifications, necessary lens voltages and resolution tests of the ion-optical column. To make the characterization realistic, the simulations account for mechanical asymmetries in the system, misalignments of lens cylinders and voltage instabilities of the power supplies. Finally, section 5 introduces the actual mechanical realization of the ion microscope. First, the complete setup including the mounting of different microscope parts is described. Then, mechanical details of the setup are presented including the fabrication of an ion lens prototype.

2. Theory of charged-particle optics

From its start in the 1930's till today charged particle optics has been an active field of research. Key element of electron- or ion-optical systems are lenses, either electrostatic or magnetic ones, used to focus, collimate or image the charged particle beams. In this chapter, different types of electrostatic lenses are discussed together with their functionality and imaging properties.

2.1. Basics of charged particle systems

This section serves as an introduction to charged-particle systems. The characteristics of charged particle beams in electrostatic fields are discussed.

2.1.1. Charged particles in electrostatic fields - The paraxial ray equation

The motion of charged particles in an electrostatic field can be deduced from the Laplace equation. For simplicity and because most electrostatic lenses are axisymmetric, the equation can be best described with cylindrical coordinates where the y-axis is the axis of symmetry of the ion-optical system. Thus, the Laplace equation reads [Hed00]:

$$\frac{\partial^2 V}{\partial y^2} + \frac{1}{r}\frac{\partial}{\partial r}\left(r\frac{\partial V}{\partial r}\right) = 0. \tag{2.1}$$

In this equation $V(r, y)$ is the electrostatic potential. Making use of the rotational symmetry the potential can be expanded in even powers of r as

$$V(r, y) = \sum_{n=0}^{\infty} A_n(y) r^{2n}. \tag{2.2}$$

Then the two terms of the Laplace equation equation are given by:

$$\frac{1}{r}\frac{\partial}{\partial r}\left(r\frac{\partial V}{\partial r}\right) = \sum_{n=0}^{\infty} 4n^2 A_n(y) r^{2n-2} \tag{2.3}$$

and

$$\frac{\partial^2 V}{\partial y^2} = \sum_{n=0}^{\infty} A_n''(y) r^{2n} \tag{2.4}$$

where the primes ($'$) indicate a differentiation with respect to y. To fulfill the Laplace Equation 2.1, the sum of the coefficients of each power of r has to be zero and a recurrence relation can be deduced

$$A_{n+1}(y) = -\frac{A_n''(y)}{4(n+1)^2} \tag{2.5}$$

thus yielding

$$V(r,y) = A_0(y) - \frac{A_0''(y)}{2^2} r^2 + \frac{A_0^{(4)}(y)}{2^2 \cdot 4^2} r^4 + ... \tag{2.6}$$

With the axial potential $V(y) = A_0(y)$, the axial and radial components of the on-axis electric field resulting from the gradient of the potential can be written as

$$E_y(y, r=0) = -\frac{\partial V}{\partial y} = -V^{'}(y, r=0) \tag{2.7}$$

and

$$E_r = -\frac{\partial V}{\partial r} = \frac{r}{2} V''. \tag{2.8}$$

In this case the explicit reference to y is omitted and only terms up to second order are retained. This is valid when considering only paraxial rays. If aberrations of electrostatic lenses shall be considered, higher order terms must be allowed.
For the case that the axial velocity of the particles is much greater than the radial velocity, the total energy of the particle is given by

$$\frac{1}{2} m \left(\frac{\mathrm{d}y}{\mathrm{d}t}\right)^2 + qV = 0. \tag{2.9}$$

The equation of radial motion then writes

$$m \frac{\mathrm{d}^2 r}{\mathrm{d}t^2} = qE_r = \frac{qr}{2} V'' \tag{2.10}$$

where q is the charge of the particle. The sign of the charge is only of importance as it must be opposite to the potential. To eliminate the time t from the above Equation 2.10 the derivative with respect to t can be written as:

$$\frac{\mathrm{d}^2 r}{\mathrm{d}t^2} = \frac{\mathrm{d}y}{\mathrm{d}t} \frac{\mathrm{d}}{\mathrm{d}y} \left(\frac{\mathrm{d}y}{\mathrm{d}t} \frac{\mathrm{d}r}{\mathrm{d}y}\right) \tag{2.11}$$

yielding for Equation 2.10

$$\left(\frac{-2qV}{m}\right)^{1/2} \frac{\mathrm{d}}{\mathrm{d}y} \left[\left(\frac{-2qV}{m}\right)^{1/2} \frac{\mathrm{d}r}{\mathrm{d}y}\right] = \frac{qr}{2m} V''. \tag{2.12}$$

This reduces to

$$\frac{\mathrm{d}^2 r}{\mathrm{d}y^2} + \frac{1}{2} \frac{V^{'}}{V} \frac{\mathrm{d}r}{\mathrm{d}y} = -\frac{r}{4} \frac{V''}{V} \tag{2.13}$$

which is known as the *paraxial ray equation*. Neither the particles charge nor it's mass appear in Equation 2.13. It is therefore valid for positively and negatively charged particles irrespective of their mass. To ensure a positive total energy the only constraint to this equation is that the potential V and the charge q have opposite signs. To deduce the equation of motion precise knowledge of the axial potential up to its second derivative is required. For simplification a *reduced radius* R can be introduced by $R = rV^{1/4}$ where V must be read as $|V|$ for positively charged particles. Differentiation of this expression yields

$$\frac{\mathrm{d}R}{\mathrm{d}y} = V^{1/4}\frac{\mathrm{d}r}{\mathrm{d}y} + \frac{1}{4}V^{-3/4}V'r \tag{2.14}$$

$$\frac{\mathrm{d}^2R}{\mathrm{d}y^2} = V^{1/4}\left[\underbrace{\frac{\mathrm{d}^2r}{\mathrm{d}y^2} + \frac{1}{2}\frac{V'}{V}\frac{\mathrm{d}r}{\mathrm{d}y} + \frac{r}{4}\frac{V''}{V}}_{=0} - \frac{3r}{16}\left(\frac{V'}{V}\right)^2\right]. \tag{2.15}$$

Using Equation 2.13 the grouped terms sum to zero and the expression reduces to the simple equation of motion

$$\frac{\mathrm{d}^2R}{\mathrm{d}y^2} = -\frac{3}{16}R\left(\frac{V'}{V}\right)^2. \tag{2.16}$$

This is known as the Picht equation [Pic32].
The only independent variable in this equation is the ratio of the axial potential gradient V' to the potential V itself. Introducing $T(y) = (V'(y)/V(y))$ Picht's equation reads

$$\frac{\mathrm{d}^2R}{\mathrm{d}y^2} = -\frac{3}{16}R\,(T(y))^2 \tag{2.17}$$

In the following, some general results will be discussed, mainly giving an approximate expression for the focal lengths of an electrostatic lens via integration of the Picht equation. Considering a ray which is incident parallel to the optical axis with a reduced radius R_1 that shall not change whilst passing the lens, a formal integration of the Picht equation yields:

$$\int_{-\infty}^{\infty} R''(y)dy = R_2' - R_1' = -\frac{3}{16}R_1\int_{-\infty}^{\infty} T^2 dy \tag{2.18}$$

Naturally, the actual radius of the incident beam does change throughout the lens, otherwise there would not be any lens action, but the change in the potential V acts in the opposite sense. As the incident ray is assumed to be parallel to the optical axis, $R_1' = 0$. From

$$R_2' = r_2'V_2^{1/4} + \frac{r_2}{4}V_2^{-3/4}V_2' \tag{2.19}$$

it can be seen that r_2' has the same sign as R_2' noting that V_2' will be zero away from the lens proper and that $V_2^{1/4}$ is intrinsically positive. Together with Equation 2.18 it can thus be seen that for a ray which is initially above the optical axis the emergent ray moves towards the axis with the lens acting *convergent*. Lenses for which object and image positions lie in regions of uniform potential ($V^{'} = 0$) are called *immersion lenses*. Approximate expressions for the focal lengths f_1 and f_2 can now be given:

$$\frac{1}{f_2} = -\frac{r_2^{'}}{r_1} = -\frac{R_2^{'}}{R_1}\left(\frac{V_1}{V_2}\right)^{1/4} = \frac{3}{16}\left(\frac{V_1}{V_2}\right)^{1/4} \int_{-\infty}^{\infty} \left(\frac{V^{'}}{V}\right)^2 dy. \tag{2.20}$$

Tracing a ray incident parallel to the optical axis, but from the other side, yields

$$\frac{1}{f_1} = -\frac{r_1^{'}}{r_2} = -\frac{R_1^{'}}{R_2}\left(\frac{V_2}{V_1}\right)^{1/4} = \frac{3}{16}\left(\frac{V_2}{V_1}\right)^{1/4} \int_{-\infty}^{\infty} \left(\frac{V^{'}}{V}\right)^2 dy. \tag{2.21}$$

The ratio of both focal lengths is then given by

$$\left(\frac{f_1}{f_2}\right) = -\left(\frac{V_1}{V_2}\right)^{1/2} = -\frac{n_1}{n_2}. \tag{2.22}$$

where n_1 and n_2 can be referred to as refractive indices on either side of the lens. The ratio in Equation 2.22 is negative because the integrals in Equation 2.20 and Equation 2.21 have opposite signs.

2.1.2. Snell's law

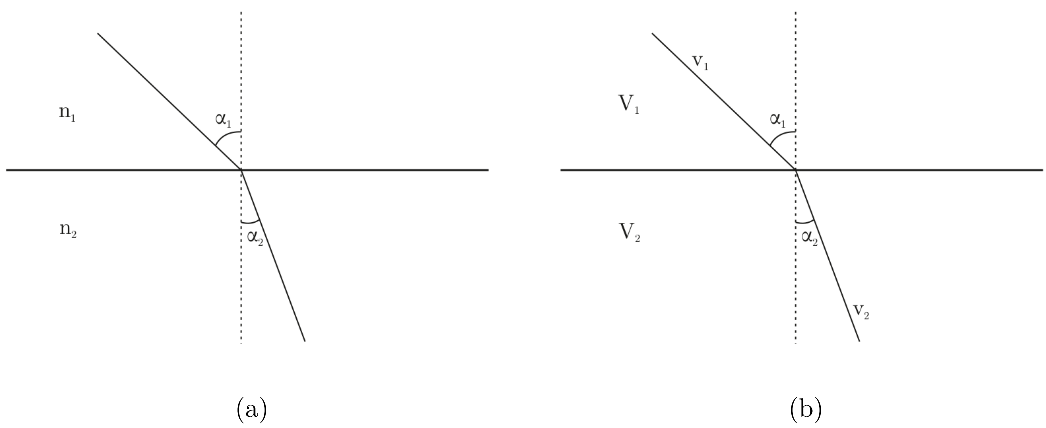

Figure 2.1: (a)Refraction of light at a plane boundary between two media having refractive indices n_1 and n_2. (b) Deviation of a beam of charged particles at a plane boundary separating regions having potentials V_1 and V_2.

In light optics the path of a ray of light incident non-normally onto a boundary separating two regions of different refractive index is changed whilst crossing the boundary. The incoming and outgoing angles are thereby related by Snell's law. In charged particle optics the analogue is a boundary separating two regions at different electrostatic potentials. Considering a particle having a velocity v_1 in the first region and v_2 in the second region, the velocities are related to the potentials V_1 and V_2 in the respective regions by

$$\frac{1}{2}mv_1^2 + qV_1 = \frac{1}{2}mv_2^2 + qV_2 = 0 \tag{2.23}$$

where m is the mass of the particle and q its charge. This expression defines the zero of potential as that for which the particle is at rest. The potential is assumed to change abruptly at the boundary, but there is no change parallel to the boundary and therefore no force parallel to the boundary acts on the particle. Thus, the component of momentum parallel to the boundary is unchanged yielding

$$mv_1 \sin\alpha_1 = mv_2 \sin\alpha_2 \tag{2.24}$$

where α_1 and α_2 are the angles between the normal to the boundary and the path of the particle in the two regions. Equation 2.23 and Equation 2.24 together yield

$$\sqrt{V_1}\sin\alpha_1 = \sqrt{V_2}\sin\alpha_2. \tag{2.25}$$

This is exactly Snell's law with $\sqrt{V}$ playing the role of the refractive index. This example however is rather artificial because abrupt changes of potential do not occur in free space. Nevertheless the general behavior of particle trajectories inside electrostatic lenses can be vividly explained using Snell's law.

2.1.3. Windows and Pupils (Beam and Pencil Angles)

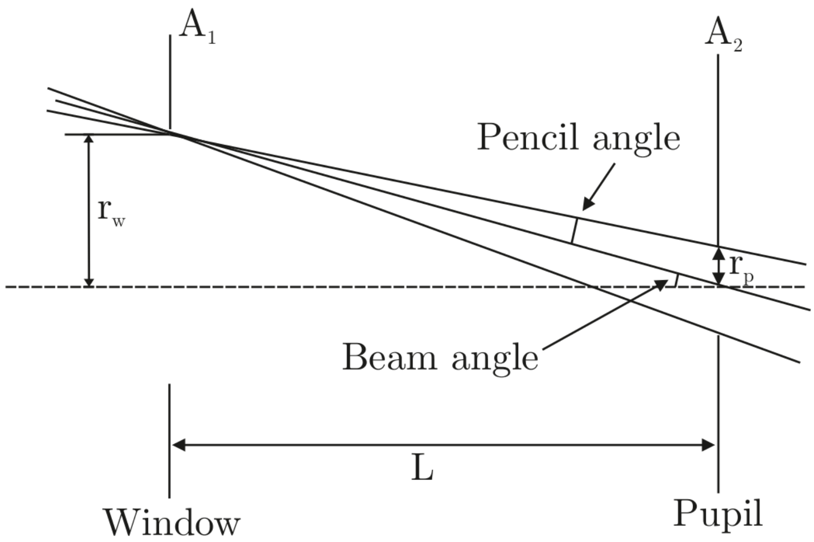

Figure 2.2: Schematic illustration of the radial and angular definition of a charged particle beam via a window and a pupil. The beam is thoroughly defined by the use of two physical defining apertures A_1 and A_2

For all practical applications it is necessary to define the spatial as well as the angular extension of the charged particle beam of interest. By defining two physical apertures [CKi95], this can be accomplished as shown in Figure 2.2. The first aperture A_1 defines the radial size of the beam. It is called the *window* of the system. Particles are emitted from every point within the window. It is assumed that any particle will be emitted isotropically. The second important aperture A_2 consequently defines the angular extent of the beam of particles that are transmitted through it. This is called the *pupil* of the system. Each point within the window defines a *pencil of rays* with half-angles Θ_p that are approximately given by $\Theta_p = r_p/L$, where r_p defines the radius of the pupil aperture and L is the distance between window and pupil. Usually L is much larger than r_p which means that the pencils of rays from all points within the window have approximately the same angle Θ_p. This beam angle varies for points across the window but usually the maximum value is quoted. It is important to note that these two physical apertures completely define a beam of charged particles.

2.1.4. The Helmholtz-Lagrange-law

Electrostatic lenses produce images of the physical apertures that define the beam, as described in the previous section. The design of an electrostatic lens may therefore be

considered in terms of these windows and pupils and their respective images. This is illustrated in Figure 2.3.
The lens produces an image of the window, which is often referred to as a virtual window. The radius r_2 of the image is related to the radius of the initial window r_1 by the linear magnification $M = r_2/r_1$. When passing through the lens, from potential V_1 to V_2, not only the radius r changes, but also the pencil angle $\Theta_p \equiv \Theta$ and the beam angle Θ_b. To relate all these quantities the law of Helmholtz-Lagrange can be considered giving

$$r_1 \Theta_1 V_1^{1/2} = r_2 \Theta_2 V_2^{1/2} \tag{2.26}$$

where the product $r\Theta V$ is conserved. The angles in this equation relate to the pencil angles, not to the beam angles.

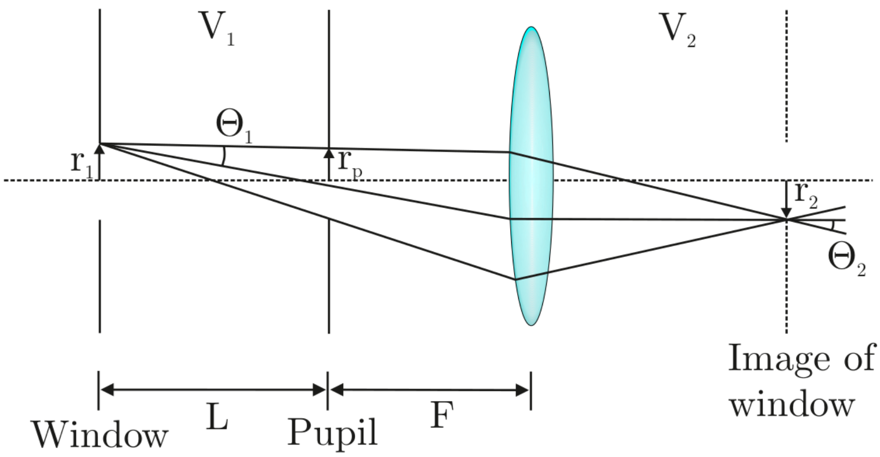

Figure 2.3: Schematic illustration of the Helmholtz-Lagrange-law with the positioning of a pupil to produce a beam angle $\Theta = 0$ at the image plane. V_1 and V_2 describe the regions of different electrostatic potential.

With Equation 2.26 the pencil angle is defined at every point of the optical system once at some point it is defined by the physical apertures. On the other hand this also means that controlling the beam angles is possible by positioning of the defining apertures. Equation 2.26 also shows that the pencil angle increases as the beam energy decreases.

2.1.5. The thick-lens-representation

In light optics, the refraction of an incident ray can be often assumed to occur abruptly at a single reference plane located at the center of the lens (thin-lens-approximation). In electrostatic lens systems however, the refraction of a ray takes place over an extended distance. In analogy to light optics, the system hence can be described as a thick lens,

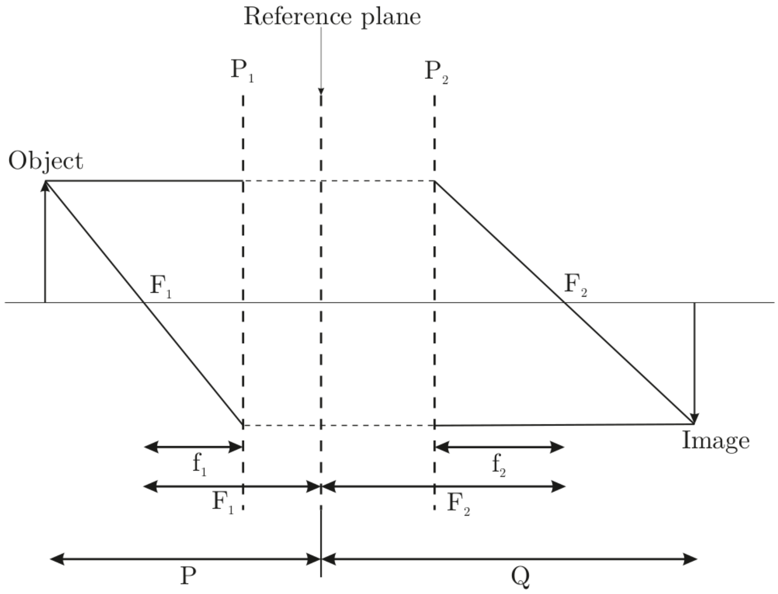

Figure 2.4: Schematic illustration of the thick-lens-representation of an electrostatic lens. The lens is defined by two principles planes P_1 and P_2 with their respective focal lengths f_1 and f_2. All positions of the principal planes, the focal points F_1 and F_2, as well as the object distance (P) and the image distance (Q) are measured with respect to a reference plane defined by the mechanical symmetry axis of the lens.

see Figure 2.4.
The thick lens representation does not include any details of the particle trajectories within the region of lens action. Instead, only asymptotic rays are considered and the whole lens can be represented by two principle planes, called P_1 and P_2. Each of these principal planes has a corresponding focal length, f_1 and f_2 with the respective focal points F_1 and F_2. All positions of the principal planes, the focal points F_1 and F_2, as well as the object distance (P) and the image distance (Q) are measured with respect to a reference plane. This reference plane is usually chosen to be the actual mechanical symmetry plane of the lens. The reference plane of a two-cylinder-lens would therefore, for example, lie at the center of the gap between the two electrodes. The distances F_1 and F_2 are often referred to as the mid-focal lengths of the lens.
Determination of the asymptotic trajectories illustrated in Figure 2.4 is accomplished as follows:

1. A particle entering the lens parallel to the optical axis follows a straight line trajectory to principal plane P_2. At P_2 the trajectory is refracted such that it leaves

the lens trough the focal point F_2.

2. A particle passing through the focal point F_1 follows a straight line trajectory to principal plane P_1 and is then refracted in such a way that it leaves the lens parallel to the optical axis.

3. Trajectories that are parallel at the entrance side of the lens, cross each other at the same point in the focal plane, F_2.

With the thick lens representation, shown in Figure 2.4, relationships between the introduced lens parameters can be defined:

$$(P - F_1)(Q - F_2) = f_1 f_2 \tag{2.27}$$

$$M = \frac{-f_1}{(P - F_1)} = -\frac{(Q - F_2)}{f_2} \tag{2.28}$$

where M is the linear magnification of the lens defined by $M = r_2/r_1$. The linear magnification of a real image is negative but in practice the sign of the magnification is often ignored and assumed to be positive.

2.2. Electrostatic Lenses

The following section introduces types of electrostatic lenses and there use in charged-particle optics. Apart from that, the operating modes of electrostatic lenses will be discussed.

2.2.1. Types of electrostatic lenses

Electrostatic lenses appear in a variety of configurations [HRB76]. Single apertures [Lie49] can be used as well as double-cylinder lenses or types with multiple electrodes. The lenses of most common use in ion-optical applications are two-electrode lenses [RAS71], immersion lenses, of which for example the aperture lens is a type [Vin60], and mostly three-electrode lenses such as the three-cylinder lens [AR72; HK70; EE70]. Of less importance but still proposed for flexible applications are multi-electrode designs [SUD05; TKH90; Tra+90; HP84; Rea83].

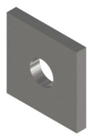

(a) Single-aperture-lens

(b) Double-cylinder-lens

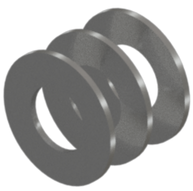

(c) Three-aperture-lens

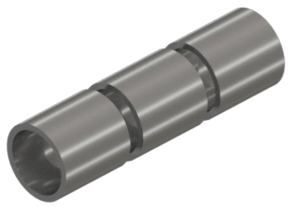

(d) Three-cylinder-lens

Figure 2.5: Some examples for simple electrostatic lens systems with one, two or three elements.

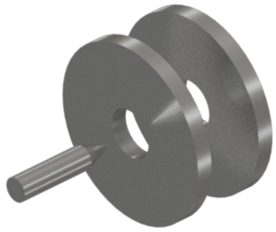

(a) Two-element lens to focus ions from a field emission tip

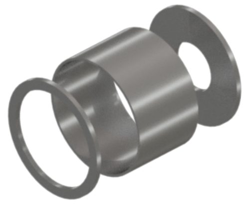

(b) Longitudinally asymmetric

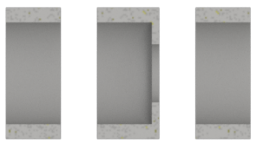

(c) Cut through a three-electrode mechanically asymmetric lens

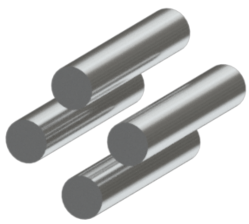

(d) Quadrupole-lens

Figure 2.6: Further types of electrostatic lenses including mechanically asymmetric lenses (still possessing rotational symmetry) and non-rotational symmetric lenses (quadrupole-lens).

Apart from that, there are mechanically asymmetric types of lenses that can be used for correction purposes or designed such, that chromatic or spherical aberration coefficients are minimal [OS79]. Figure 2.5(a) shows an example of a single aperture lens, Figure 2.5(b) a double-cylinder lens. The single aperture lens is of little use for practical purposes as it works with different potentials on each side of the lens. However this type of electrostatic lens can be used to emulate effects of individual mesh holes in mesh electrodes or it is used as an element combined with other (plane) electrodes in immersion lens systems. A double-cylinder lens can be used when it is required that object and image lie in regions of different potential. Object and image planes can be held fix if the ratio of the potentials of the two cylinders is in proportion to the ion energies being imaged. Figure 2.5(c) and Figure 2.5(d) illustrate forms of the most commonly used electrostatic lenses namely the three-aperture lens and the three-cylinder lens. Both lenses are type of the rotationally symmetric three-electrode lenses.

Three-cylinder-lenses are generally used for high quality imaging finding a use in cathode ray tubes or electron microscopes. These lenses can be operated in two ways. In the so-called *einzel mode*, the potential at the entrance and exit of the lens is equal, i. e $V_1 = V_3$. In the so-called *asymmetric mode* all three lens voltages are different ($V_1 \neq V_2 \neq V_3$).

Figure 2.6 shows some further examples of electrostatic lenses. Figure 2.6(a), for example, shows an immersion lens system where ions can be extracted through two apertures via a field emission tip. Figure 2.6(b) illustrates the shape of a longitudinally-asymmetric but (still) rotationally symmetric lens. Figure 2.6(c) shows a cut through a mechanically asymmetric lens. It has been shown that aberration coefficients of lenses can be reduced by introducing axial mechanical asymmetries into lenses of rotational symmetry [OS79; Rid78]. Figure 2.6(d) shows a so-called quadrupole lens. This lens can be important because its spherical aberrations can be of opposite sign to those of rotationally symmetric lenses that have been previously introduced (e.g. the three-cylinder-lens). In such lenses, rays far away from the optical axis have a longer rather than a shorter focal length compared with rays close to the axis. The fact, that conducting electrodes which run along the optical axis cause one or more discontinuities in the axial potential, leads to this so called "anti-aberration" property. This can be used to correct or reduce spherical aberrations of a system of different lenses.

2.2.2. Operating lens modes of three-cylinder lenses

Three-cylinder-lenses can be operated in different modes. As previously mentioned, the so-called *einzel mode* of a lens corresponds to the operation where the potential at the entrance and exit of the lens is equal, i.e. $V_1 = V_3$. All lens parameters are only dependent on the single voltage ratio V_2/V_1. However, three-cylinder-lenses can also be operated asymmetrically, meaning that all three lens voltages are different ($V_1 \neq V_2 \neq V_3$). In this mode the three-cylinder-lens is an immersion lens, making a transition between two regions of different potential.

Apart from that, electrostatic three-cylinder lenses can be run in a retarding (or decelerating) and accelerating mode with the central electrode of the lens retarding the ions as they enter the lens and accelerating them as they leave or accelerating ions when entering and retarding them at the exit of the lens. Ion trajectories through a decelerating and accelerating lens are illustrated in Figure 2.7.

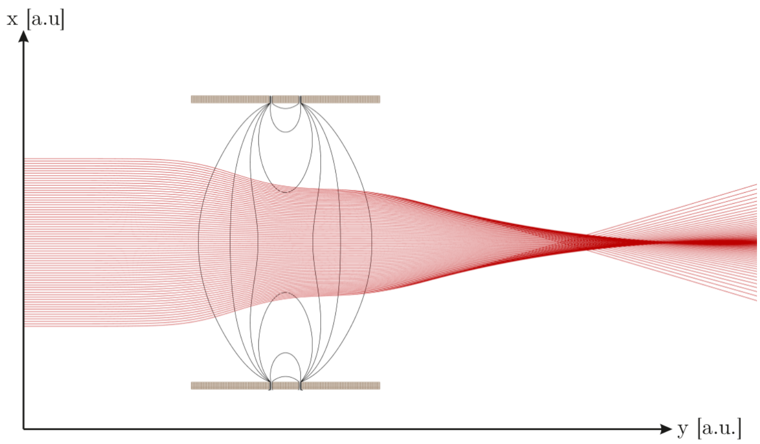

(a) Accelerating mode

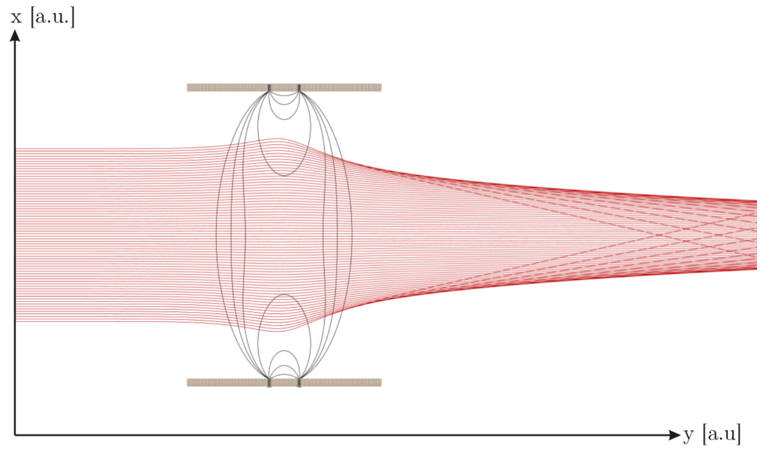

(b) Decelerating mode

Figure 2.7: Ion trajectories through a three-cylinder lens in two different operating lens modes. Equipotential lines are drawn in black. (a) Accelerating mode: Ions are accelerated between the first and second electrode of the lens, pass a potential minimum and are then decelerated when passing the region between second and third cylinder. (b) Decelerating mode: Ions are decelerated between first and second electrode and accelerated when passing the region between second and third cylinder.

With both operating modes, retarding and accelerating, the same focal properties can be achieved. However, the voltage applied to the middle electrode has to be much higher in the accelerating, than in the decelerating mode when aiming for a similar focal length. The accelerating type of lens nevertheless usually has a lower spherical aberration coefficient for a given focal length as the ion trajectories are bend inwards to the optical axis when entering the region of lens action. Apart from that, ions move faster inside the lens than outside of the lens. Thus, they will suffer less from the effects of stray magnetic fields or space charge. In general, the disadvantages associated with applying much higher voltages outweigh the advantages of the accelerating lens mode which means that in microscope applications retarding (or decelerating) lenses are more often used.

Higher-order operating ranges In most applications electrostatic lenses are operated as weak converging lenses where the principal planes coincide and a "thin-lens-representation" can be applied. However with increasing lens excitation ("strength of the lens") the principal planes move apart from each other and a "thick-lens-representation" is required. In strong lenses the point of intersection of parallel incident rays can move inside the lens, so as to produce a second or even a third crossover with the optical axis by subsequent focusing [EE70]. According to the number of existing crossovers the operating ranges of the lens will be of first, second or third order, respectively. In the operating range of even order, negative focal lengths occur [HL67].

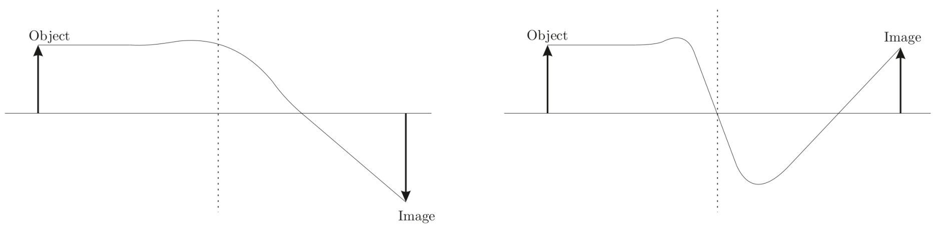

(a) First order operating range (b) Second order operating range

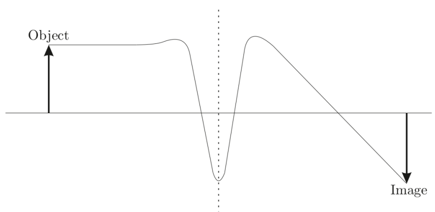

(c) Third order operating range

Figure 2.8: Schematic illustration of different operating ranges of an electrostatic lens. (a) first operating range (b) second operating range (c) third operating range.

2.3. Aberrations

The operation of axially symmetric ion lenses, like the commonly used three-cylinder lens, is based on the paraxial theory which is a *first-order* theory. However, particle trajectories in ion-optical systems always suffer from finite displacements and finite slopes with respect to the optical axis. Omitting higher-order terms in the series-expansion leading to the paraxial ray equation, as shortly introduced in subsection 2.1.1, will therefore cause some errors. The paraxial theory is just an approximation and errors due to higher-order terms are commonly known as *geometrical aberrations*. In practice, a point object will in fact not be imaged onto a conjugate point but to a blurred spot with finite size. This phenomenon is known as geometrical aberration. Errors may not only occur from finite distances of particles from the optical axis (and in consequence the paraxial region) but may also arise from different velocities the particles may have. An initial energy spread of the particles therefore results in different foci even if the paraxial approximation in this case would be exactly valid. This effect is called *chromatic aberration* equivalent to the fact that in light optics the index of refraction is different for photons of different frequencies (energies). Chromatic aberrations may also occur owing to variations caused by voltage instabilities.
Another source of image defect is *space charge*. Electrostatic repulsion prevents particles of the same charge to be focused exactly into a point. In consequence, again even in the paraxial approximation and in the absence of any initial energy spread an ideal point image can only exist if the beam current is negligibly small.
Finally practical problems like *material inhomogeneities* and *mechanical imperfections* have to be taken into account.
The following section will introduce monochromatic as well as chromatic aberrations of electrostatic lenses. These aberrations are unavoidable even for static, rotationally symmetric electrostatic lenses free of space charge, that produce a real image of a real object and for which the potential $V(y)$ as well as $V^{'}(y)/V(y)$ are continuous. This is called Scherzer's theorem [Sch36].
Thus, particle lenses are subject to the same aberrations as optical lenses.

2.3.1. Spherical aberrations

The effect that off-axis rays with a larger opening angle are refracted stronger than near-axis rays is called *spherical aberration*. For particle beams near the optical axis (which is usually the case in charged-particle optics) spherical aberrations are normally of much greater importance than off-axis aberrations like coma, astigmatism or distortion. As illustrated in Figure 2.9, off-axis rays with larger opening angle are refracted stronger then near-axis rays resulting in a shorter focal length. This can be vividly understood by taking into account that the radial electric field component E_r increases with increasing distance to the optical axis and hence also the field component $E_\perp$ which is perpendicular to the propagation direction of the ions leading to a smaller radius of curvature of the ion trajectory.

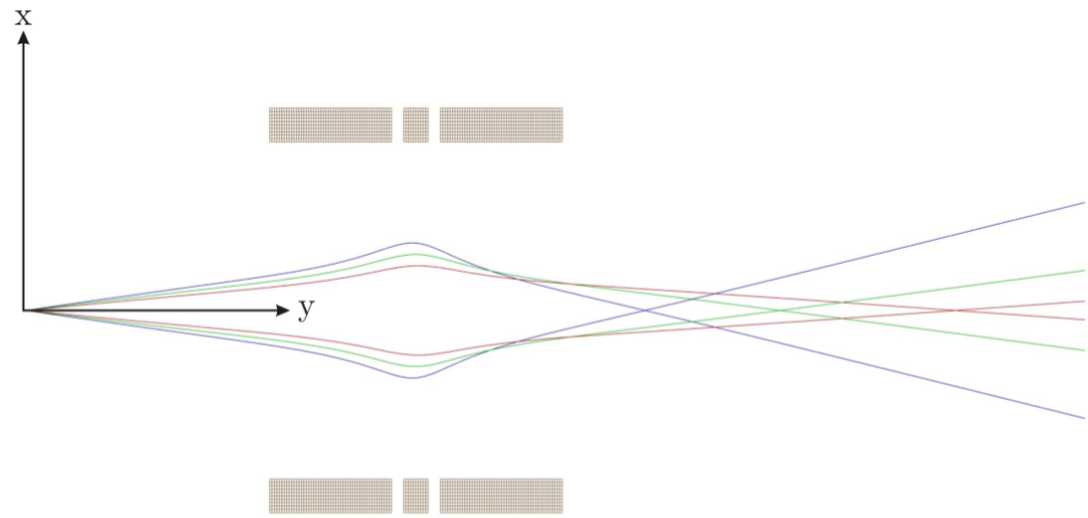

Figure 2.9: Illustration of the effect of spherical aberration. Ion trajectories with larger opening angle α_0 (blue) are focused stronger than near-axis beams with lower opening angle (red). For rotationally symmetric electrostatic lenses the spherical aberration coefficient C_s is always positive.

The radius Δr_s of the disc of least confusion due to spherical aberration for a lens operated with magnification M is defined by

$$\Delta r_s = -MC_s(M)\alpha_0^3 \tag{2.29}$$

where α_0 is the opening angle of the particle beam. The spherical aberration coefficient $C_s(M)$ can be expressed as a fourth order polynomial in the magnification M

$$C_s(M) = C_{s_0} + C_{s1}/M + C_{s_2}/M^2 + C_{s_3}/M^3 + C_{s_4}/M^4. \tag{2.30}$$

The C_{s_i} are properties of the lens itself. Reduction of these parameters by optimization of the geometry of the lens leads to lower spherical aberration. Apart from that, spherical aberrations can be reduced by reducing the opening angle α_0 of the particle beam entering the lens. Using several electrostatic lenses can be helpful to distribute the refractivity and as a consequence being able to keep the opening angle minimal. Correction of spherical aberrations can be accomplished by using non-rotational symmetric lens shapes that can have negative spherical aberration coefficients. Using such types of lenses, e.g. quadrupoles, in combination with lenses with positive spherical aberration coefficient can thus compensate spherical aberrations in an ion-optical system.

2.3.2. Coma

The coma is the next important aberration after the spherical aberration in high performance electron and ion-optical systems as it affects the resolution of off-axis points located within the imaged object centered around the optical axis. The effect of coma is illustrated in Figure 2.10 where particles starting with an opening angle α_0 in a distance r from the optical axis are imaged through an electrostatic three-cylinder lens.

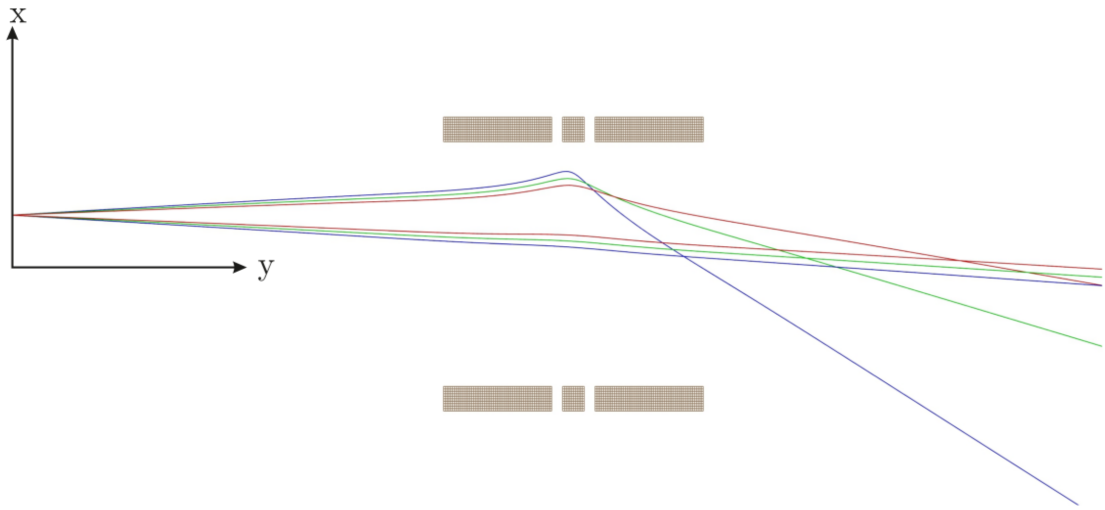

Figure 2.10: Illustration of coma: Particles starting with an opening angle α_0 and a distance r from the optical axis are imaged via a three-cylinder-lens. The coma results in a comet-tail like distortion of the object points in the image plane.

The refractivity of the electrostatic lens, dependent on the distance from the optical axis, leads to a comet-tail like distortion of the objects points. The disc of least confusion due to coma, resulting from imaging of a point-like object, is given by

$$r_c = C_{\text{co}} M \alpha_0^2 r \tag{2.31}$$

It can be seen that coma scales quadratically with the opening angle α_0 and linearly with the distance r from the optical axis.

2.3.3. Astigmatism

When an object point lies at a distance r from the optical axis, the incident cone of rays will strike the lens asymmetrically giving rise to an aberration known as astigmatism. The word derives from the Greek *a-*, meaning not, and *stigma*, meaning spot or point. To facilitate the description of this type of aberration it is convenient to introduce two planes, the *meridional* and the *sagittal* plane. The sagittal plane contains the ion beam and the optical axis. The meridional plane contains the ion beam and is perpendicular to the sagittal plane.

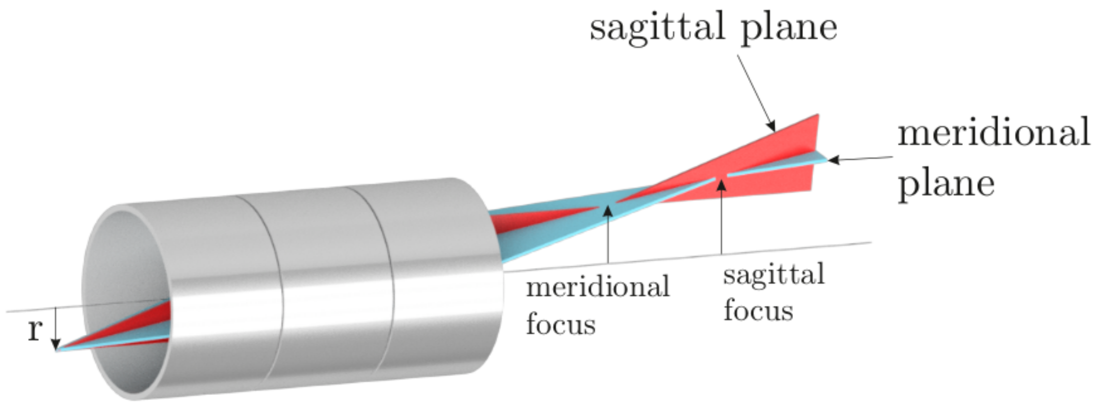

Figure 2.11: Astigmatism causes an off-axis beam with distance r to the optical axis to have two different focal lengths in the sagittal and meridional plane.

The focal lengths in these two planes will differ. In effect, the meridional rays are tilted more with respect to the lens than the sagittal rays resulting in a shorter focal length. In light optics it can be shown, using Fermat's principle, that the focal length difference depends on the power of the lens and the angle at which the rays are inclined. The effect of astigmatism leads to the fact, that an incidentally off-axis beam with opening angle α_0 can not be focused onto a single point. The cross-section of a bundle of beams with different opening angles is initially circular, but it becomes elliptical with the major axis in the sagittal plane until the ellipse degenerates into a "line" at the meridional focus. This "line" is actually a complicated elongated diffraction pattern that becomes more line-like the more astigmatism is present. All rays from the object point have to traverse this "line" which is commonly known as the *primary image*. Beyond this primary image point, the cross section of the ion beam rapidly opens until it gets circular again. This point where the image is a circular blur, is known as the *circle of least confusion*. The radius of this circle is given by

$$r_a = C_a M \alpha_0 r^2 \tag{2.32}$$

where α_0 is again the opening angle, M the linear magnification and r the initial distance to the optical axis. Moving even farther from the lens, the beam's cross section will deform again into a "line", called the *secondary image*. This time it is in the meridional plane at the so-called *sagittal focus*.

In charged-particle optics, a different form of astigmatism is of most concern, the *axial* astigmatism. In electrostatic lenses that are not perfectly rotational symmetric with respect to the optical axis, even a bundle of rays parallel to the optical axis will be imaged with astigmatic errors leading to the focusing of a single object point to a line.

2.3.4. Field curvature and distortion

Field curvature results as a direct consequence of the dependance of the radial field component E_r on the distance to the optical axis in rotationally symmetric electrostatic lenses. The image plane gets shifted rotationally symmetric in dependance of the distance from the optical axis and the opening angle α_0. The image curvature bulges the images field and stigmatic image points are located in a rotationally symmetric paraboloid which touches the central region of the Gaussian plane. A sharp image can therefore only be found on a bent surface, the so called Petzval-surface. This is illustrated in Figure 2.12.

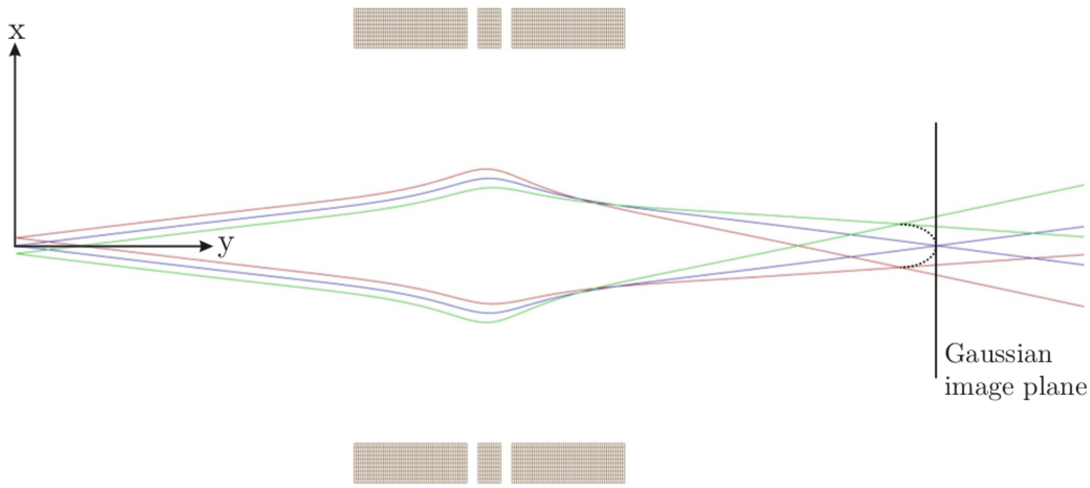

Figure 2.12: Illustration of field curvature: a sharp image can only be found on a bent surface, the Petzval-surface.

Distortion is the last of the five primary, monochromatic aberrations. It is a consequence of the fact that the transverse magnification M is dependent on the off-axis image distance. Thus, this distance differs from what is expected in paraxial theory in which the magnification is constant. This means that distortion arises because different areas of the lens have different focal lengths and magnifications. The 2D trajectories of a distorted image resulting from a square array in the object plane are shown in Figure 2.13. If no other form of aberration is present, distortion manifests itself in a mis-shaping of the image as a whole, even though every point of the image is sharply focused. As depicted in Figure 2.14(a) and (b) a square array deforms as a consequence of positive or pincushion distortion. Each image point is displaced radially outward from the center, with the most distant points moving the greatest amount. This means that the transverse magnification increases with the axial distance r. Similarly, negative or barrel distortion corresponds to the decrease of M with the axial distance r as depicted in Figure 2.14(c). Each point on the image moves radially inward towards the center.

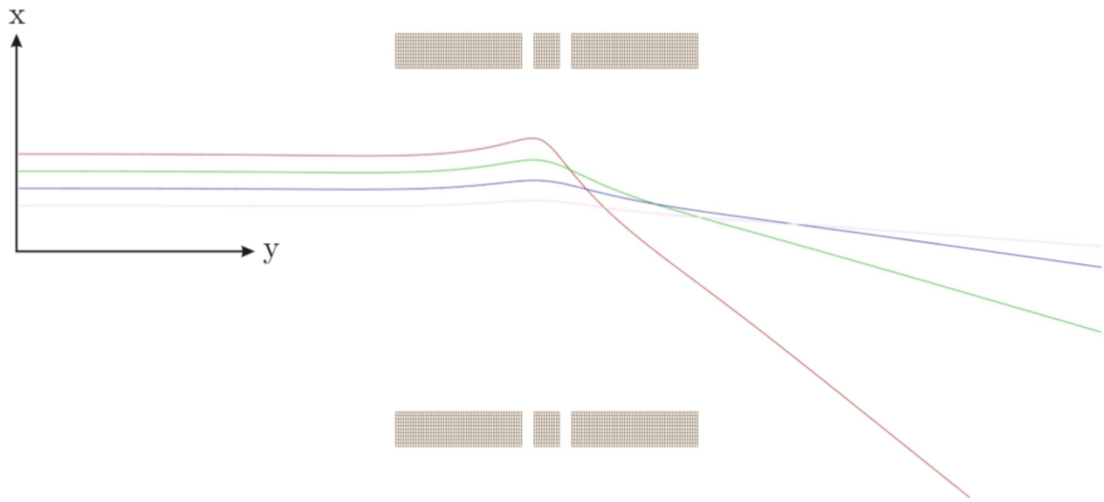

Figure 2.13: 2D trajectories of a square array in the object plane resulting in a positively distorted image.

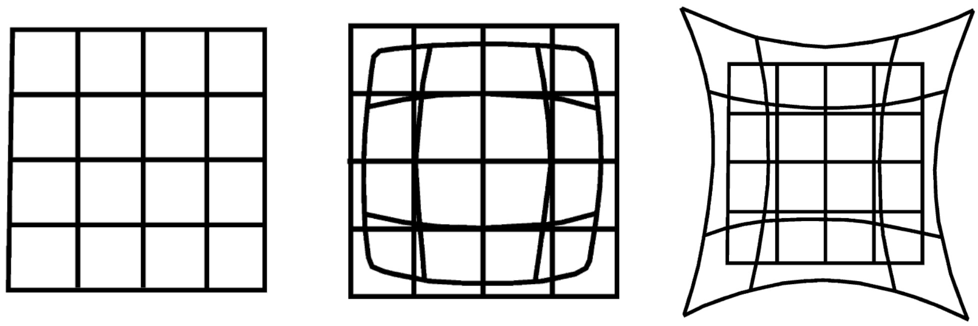

Figure 2.14: Distortion of the image of a square array. (a) ideal imaging, (b) positive or pincushion distortion: the transverse magnification increases with the axial distance, (c) negative or barrel distortion: the transverse magnification decreases with the axial distance [HRo09].

2.3.5. Chromatic aberrations

The focal properties of an electrostatic lens depend on the initial kinetic energy of the particles when entering the lens. Particles with higher kinetic energy E_{kin} are focused less than particles with lower kinetic energy. The energy spread ΔE of the initial energy E therefore leads to a chromatic aberration where the chromatic disc of least confusion is given by [SUD07]:

$$r_c = C_c M \alpha_0 \frac{\Delta E}{E} \tag{2.33}$$

The effect of chromatic aberration is illustrated in Figure 2.15. Ions with higher kinetic energy E_b (blue) are focused less stronger than ions with lower kinetic energy $E_r < E_b$ (red).

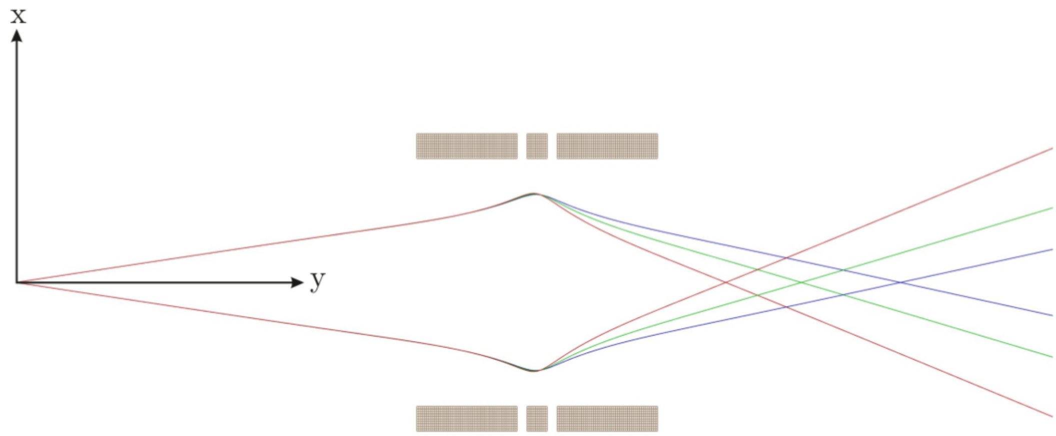

Figure 2.15: Illustration of the effect of chromatic aberration. Particles with higher energy E_b (blue) entering an electrostatic lens are focused less strongly than ions with a lower kinetic energy E_r (red).

In ion optical systems the chromatic aberration at the image plane consists of two kinds: the axial chromatic aberration and the chromatic distortion. The axial chromatic aberration affects the resolution of the imaging whereas the chromatic distortion represents the chromaticity of the magnification. By arranging and exciting the intermediate lenses properly, it is possible to compensate the chromatic distortion which is essential for high resolution imaging purposes [HRo09].
The chromatic aberration with its coefficient C_c is of most concern in objective lenses, where the incident angles are comparatively large. The chromatic distortion with coefficient C_D mainly affects projector lenses, where the angles of the particles with respect to the optical axis are small but the rays are farther away from the optical axis.

2.4. General considerations concerning ion-optical devices

This section should serve as a short summary listing practical details when designing an ion-optical system. Generally, one has to keep in mind that for an electrostatic system the inter-electrode spacings must be sufficiently large to avoid breakdown and suitable tracking distances along insulating materials have to be chosen. For polished electrode surfaces, the spacing between electrodes should be more than 1 mm per 10 kV for electrons and 1 mm per 6 kV for ions in vacuum [Dru84]. For ion-optical systems, the breakdown distances are larger than for electrons because the interaction of ions with the metal surface leads to the production of secondary electrons and thus increases the chances of an electrical breakdown. Apart from that, ions can also sputter off neutral atoms which can build up on insulators as a metallic film. A common way to insulate different lens cylinders from each other is to use high precision ceramic balls. As a rule of thumb the dimensioning of these balls has to be chosen such, that the diameter in mm corresponds at least to the maximum potential difference in kV between two electrodes. Then, the voltage drop per length unit along the ceramic spheres' surface is less than 1.3 kV/mm, assuming one fourth of the spheres circumference as insulating distance.

Suitable materials for electrodes are generally non-magnetic stainless steels and some non-magnetic aluminium alloys. For ions the magnetic screening is significantly less than for electrons and therefore residual permeabilities of electrode materials are less relevant. However, care must be taken to ensure that the ions in the beam cannot “see” any insulating material to avoid charging-up phenomena that can lead to astigmatism and instabilities in the beam current.

Another aspect to consider is the effect of mechanical tolerances, i. e. the circularity of bores and the accuracy of the alignment of electrostatic lenses. If the lens bores are non-circular or displaced laterally with respect to each other, astigmatism and deviations of particle trajectories from their paraxial paths can be introduced. In high resolution imaging applications the ellipticity of the final lens bore should not be greater than the spatial resolution expected of the system.

3. Design of the ion microscope

The work of this thesis aims at designing, simulating and developing a high-resolution ion microscope for ultra-cold atom experiments. The goal was to reach a maximum magnification of at least $M = 1000$ and a final resolution better than 1 µm. The experiment is designed in a way that ultra-cold atoms can be prepared in an optical dipole trap where they can get excited to Rydberg states. The Rydberg atom will be photo-ionized and extracted into the ion microscope with two plates of opposite polarity. The microscope itself consists of three electrostatic lenses.
This chapter outlines the development of the microscope design. First the experimental requirements are outlined followed by a description of the electric field control. The focus of this section lies on the simulation process to obtain the final microscope design.

3.1. Objectives of the ion microscope

For the design of the ion-optical system several aspects concerning the objectives of the microscope itself have to be considered. This implies a sharp imaging over an extended volume given by typical sizes of ultracold atom samples. For the design of the microscope a depth of start of 25 µm is assumed, over which a sharp imaging can be performed. Furthermore, the field of view in radial direction in which a high-resolution image can be achieved, should only be limited by the size of the active area of the detector in conjunction with the magnification of the microscope.
One of the goals of the experiment is to extend the investigation of ion-atom scattering from the so far studied cold, but essentially classical regime to the quantum regime using Rydberg molecules [Sch+17]. The Rydberg molecule is thereby photo-ionized to start the scattering event between the Rydberg ionic core and the ground state atom. To experimentally determine the S-wave scattering length, the freely moving scattered ion of a single scattering event is imaged onto the detector. After many repetitions, the scattered wavepacket can be reconstructed either in momentum or in real space. To image the shape of the scattered wavepacket after a short free evolution time a sub-µm resolution is required. Since the resolution of the detector is limited to around 50 - 100 µm [Hon+16; Hoe+13; Cos+05], the ion microscope has to deliver a maximum magnification of at least $M = 1000$. Apart from this, Rydberg blockade effects emerge on the µm scale [SWM10] and the ion microscope can be used as a tool to further explore the involved phenomena.

3.2. The cold Rydberg apparatus

The experiment is designed to be a dual-species Rydberg experiment enabling the study of various combinations of Rydberg molecules out of Rubidium and Lithium. Rubidium and/or Lithium atoms out of a reservoir, are pre-cooled using a dual-species Zeeman slower and trapped in a magneto-optical trap in a first experiment chamber: the MOT chamber. The cold atoms are then loaded in an optical-dipole trap in which they are transported optically to another vacuum chamber: the science chamber. The optical transport is realized with an optical lens mounted on a translation stage to continuously move the focus of the trap between the two chambers.

3.3. Experimental requirements

For the design of the ion optics several aspects concerning the geometry of the experimental setup had to be considered. As shown in Figure 3.1, atoms, pre-cooled in a magneto-optical-trap (MOT), are optically transported into the science chamber. To this end, the atoms are trapped in an optical dipole trap and a translation stage is used to accomplish the transport. All ion-optical elements need to guarantee access for the optical beams

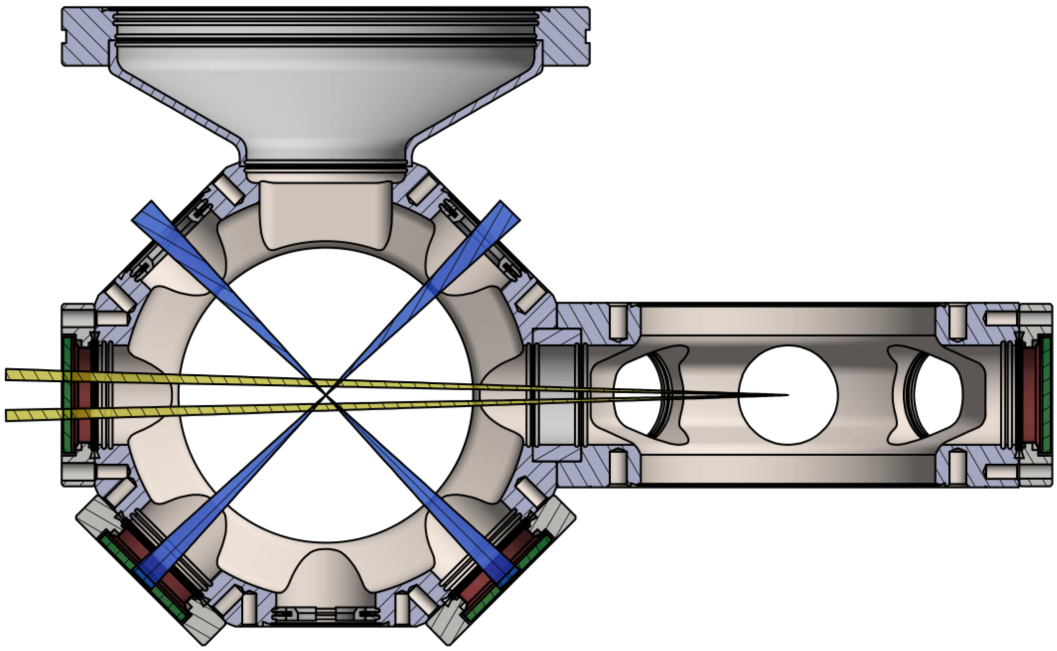

Figure 3.1: Cross section of the two experiment chambers: Cold atoms will be transported from the MOT chamber (right) into the science chamber (left) in a dipole trap via optical transport. Optical beams in blue are schematically drawn to illustrate the optical access through the diagonal ports of the chamber. Dipole trap beams are shown in yellow. The ion microscope will be mounted in the vertical direction through the depicted funnel.

forming the dipole trap, the photo-ionization, the excitation and the imaging of Rydberg atoms. The purpose of the science chamber is the preparation and manipulation of Rydberg atoms. It features nine windows to allow for optical access for trapping, exciting, photo-ionizing and imaging Rydberg atoms. On the vertical axis, a high numerical aperture (NA) in-vacuum lens is planned. For precise experimental work with Rydberg atoms, electric stray fields have to be well compensated in the mV/cm regime. When

working with ions the electric field sensitivity is even higher. The required ion-optical elements should therefore include an electrode geometry in the science chamber that is capable of compensating electric stray fields in arbitrary directions and still provides the ability to effectively extract photo-ionized Rydberg atoms into the ion-optical column. The maximum length of the microscope is only limited to 1.5 m by the height of the ceiling. However, to avoid mechanical instabilities due to vibrations and to keep mechanical tolerances as small as possible, it is desirable to construct the ion-optical-column in a way that provides a maximum magnification of $M = 1000$ but minimizes the length of the electrode stack. Since the housing of the ion optics and the ion lenses contribute a large fraction of the total outgassing area in the vacuum system, a goal was to separate most of the ion optics from the science chamber by a differential pumping stage. This leads to a lower pressure in the science chamber compared to the upper vacuum part. For maintenance of the detector without breaking the high vacuum in the science chamber a valve is planned. The ion microscope is therefore split in two parts with a gap of 25 mm in between, given by the size of the valve.
Finally the ion optics need to guarantee optical access in the vertical direction for e. g. absorption imaging. The ion microscope therefore has to be interrupted in a way that guarantees this optical access but simultaneously does not disturb the imaging properties of the microscope itself.

3.4. Electric field control

With the polarizability of Rydberg atoms scaling with the effective principal quantum number n^{*7}, a precise control over electric fields and the ability to compensate residual electric stray field down to the mV/cm level is essential. Therefore the central region of the experiment chamber, containing the position of the atom cloud, has to be surrounded by an electrode configuration that is on the one hand capable of compensating electric stray fields in arbitrary directions and on the other hand offers the ability to effectively extract photo-ionized Rydberg atoms into the ion microscope. Contrary to previously used cloverleaf configurations with eight electrodes [Löw+12], the new electric field control consists of six electrodes in a rotationally symmetric configuration. This is important to prevent inducing astigmatism in the ion optics. Furthermore, optical lens, electric field control and first ion lens are well centered and intrinsically aligned.

3.5. Simulating charged-particle optics

The program used to create, simulate and characterize different microscope geometries is the charged-particle optics simulation program “SIMION”. The program is capable of calculating the electrostatic potential for every point within the simulated volume by solving the Laplace equation under reasonable boundary conditions. Furthermore, SIMION solves the equation of motion for charged particles within the given electrode geometries and is hence capable of simulating particle trajectories for given electrode geometries and voltage settings.

SIMION makes use of 2D symmetrical and/or 3D asymmetrical electrostatic and/or magnetic potential arrays and calculates potential values on every grid point by using a finite difference method called over-relaxation [MD08]. This technique is applied to two or three dimensional potential arrays of points representing electrode and non-electrode regions. Relaxation techniques generally use iteration for successive approximation. With these methods normal numerical computation errors are minimized and solutions are quite stable. However, the exact number of iterations required for a given level of accuracy is quite variable and initially unknown for each specific solution.

3.6. The imaging system

The imaging system consists of three electrostatic lenses that image an initial ion via two intermediate images onto the detector. The number of electrostatic lenses is chosen such that a magnification of $M = 1000$ is reached under the constraint of a total length of $L < 1500$ mm. With three lenses spherical aberrations are kept small due to small angles of incidence of ion trajectories when entering the lenses.
The imaging process happens with two intermediate images with image distances $x\mathrm{Im}_1$ and $x\mathrm{Im}_2$ measured from the center of the atomic cloud where the Rydberg excitation takes place. The first lens produces an intermediate image in front of the second lens which is then magnified by the second lens to produce an intermediate image in front of the third lens. This second intermediate image is then magnified to the final image on the detector. The detector consists of a micro-channel-plate (MCP) in conjunction with a delay line detector for spatial resolution.

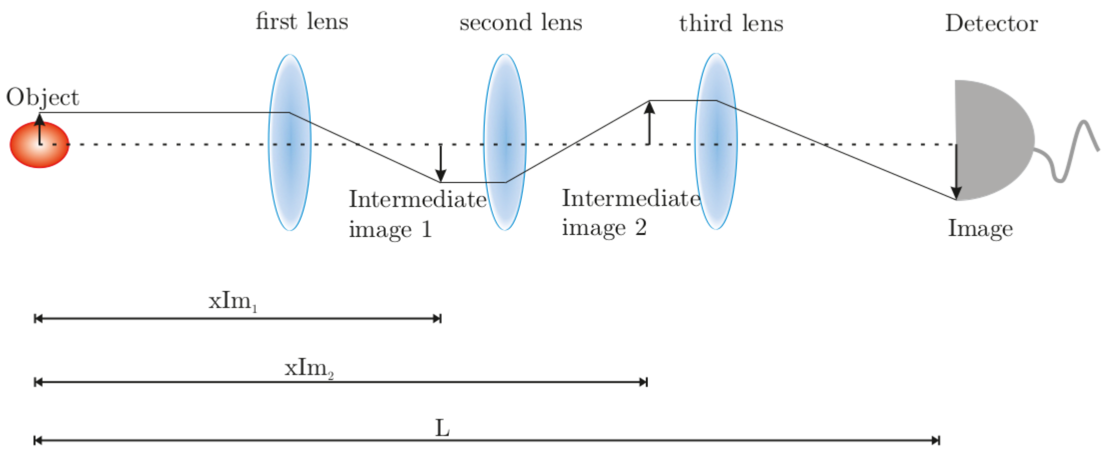

Figure 3.2: Schematic illustration of the imaging system. The ion microscope consists of three electrostatic lenses that image an initial ion via two intermediate images onto the detector (MCP and delay line detector).

3.7. The simulation procedure

To find, simulate and characterize the most suitable and best performing design of the ion microscope, a comprehensive and powerful program was written which programmatically controls SIMION and allows for the fully automated characterization of different geometries and scans over large parameter spaces. The functionality and capabilities of this SIMION intern user program written in the programming language "lua" are outlined in the following.
In a first step, the geometry of a given lens system is loaded and refined. In the refining process, SIMION solves the Laplace equation for the electrode geometry at every grid point within the given volume. Default values of the electrode voltages are then set by the program. To find the correct intermediate and final image positions and the corresponding lens voltages an algorithm evaluating the trajectories of 15 particles has been developed.

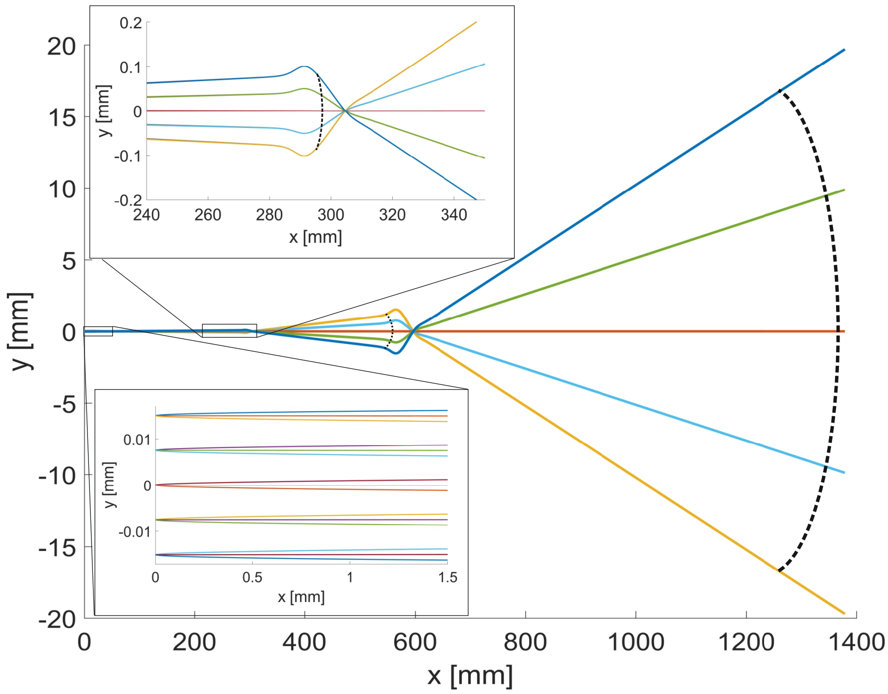

Figure 3.3: Illustration of how the image positions are calculated with the help of SIMION. Five bundles consisting of three rays each and starting with positive, zero and negative elevation angle, are propagated through the current geometry. The intersections of each bundle of rays are determined yielding the intermediate image positions $x\mathrm{Im}_1$ and $x\mathrm{Im}_2$ as well as the final image position in the detector plane. Lower inset demonstrates the ions initial conditions, upper inset shows the first intermediate image. Curved dashed lines indicate the positions of all images.

Ions with a mass of $m = 87u$, where u is the atomic mass unit, start in sets of three particles at different starting positions, offset by different distances from the optical axis (see Figure 3.3). In each bundle of particles, ions start in $+y$, $-y$ and $+x$ direction respectively, with an initial energy of $E_{\text{kin}} = 1 \cdot 10^{-5}$ eV giving rise to small initial starting angles for each upper and lower particle. The initial situation is illustrated in the first inset in Figure 3.3. For most of the simulations, the ions are extracted and accelerated with the repeller plate at +500 V and the extractor plate at -500 V typical. The electrostatic lenses are connected via drift tubes where every drift tube voltage is set to -2400 V according to the operating voltage of the front plate of the micro-channel-plate detector (MCP) used in the experiment. Lens voltages at each middle cylinder of the three-cylinder-lenses are tuned automatically to produce images at pre-defined intermediate and final image positions. For a given voltage configuration, the image positions are found by the evaluation of the intersections of trajectories of particles starting in the same bundle. With this, the Petzval surface of the image (s. subsection 2.3) can be determined and the Gaussian image plane is calculated using the three central beams starting on the optical axis. In Figure 3.3 the Petzval surface is outlined as a dashed line for both the intermediate images and the final image. A searching algorithm has been developed to tune the lens voltages in the correct direction to shift the image at the desired position.

The algorithm is capable to differ between *accelerating* and *decelerating* lens modes (s. subsection 2.2.2). Figure 3.4 illustrates how image position and magnification vary with the applied lens voltage V using the example of a three cylinder lens. By comparing the image position for two different lens voltages, the lens mode can be determined. For positive ions in the accelerating branch, the image position increases when increasing the (high) negative voltage on the middle cylinder of the lens. In the decelerating branch the image position increases when decreasing the (low) negative voltage on the middle cylinder of the lens. To exclude higher order operating lens modes the parity of the ion trajectories, defined by the normalized gradient, is determined and a parity change is required for the searching algorithm to continue (s. subsection 2.2.2). It is desired to operate the lenses only as weak converging lenses in first order.

With the intermediate and the final image being at the correct positions, the magnification of the current geometry and voltage configuration is easily determined from the image in the detector plane.

To characterize the quality of the image in each configuration, the algorithm propagates another set of ions through the lens system. As illustrated in Figure 3.5, two groups of particles are generated which are separated by a small distance, and share a large offset from the optical axis. While the offset from the optical axis resembles the maximum field of view, the small separation between the groups is used to characterize the resolution of the system. This spacing $s(M)$ is scaled with the magnification according to the resolution limit of the detector ($\approx 100\,\mu\text{m}$ [Kha+16; Hon+16; Hoe+13; Cos+05]). The initial kinetic energy is chosen to be $E_{\text{kin}} = 9.3$ neV corresponding to the approximate energy of $^{87}\text{Rb}^{+}$ ions at a temperature on the order of $160\,\mu\text{K}$. The initial kinetic energy however is negligible compared to the large extraction voltage in the microscope. A

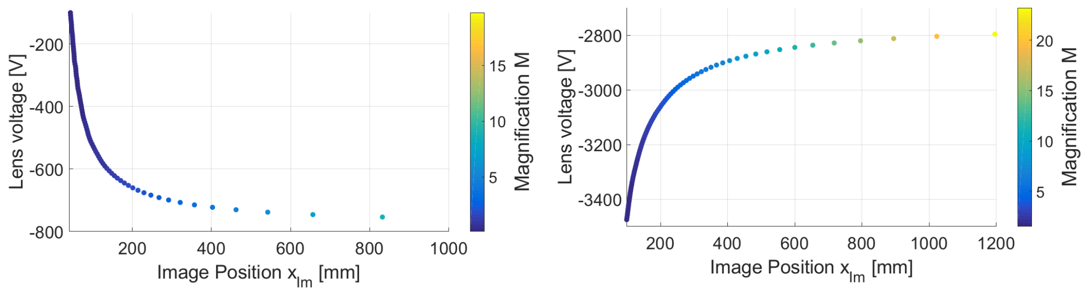

(a) Decelerating branch of the electrostatic three-cylinder lens.

(b) Accelerating branch of the electrostatic three-cylinder lens.

Figure 3.4: Lens voltage versus image position considering the example of the first lens of the ion microscope. The colorbar indicates the magnification. (a) Decelerating branch of the electrostatic lens: the image position increases when decreasing the lens voltage. (b) Accelerating branch of the lens: the image position increases when increasing the lens voltage. The image searching algorithm recognizes the branch and varies the lens voltages for $V_1 = -500\,\mathrm{V}$ and $V_3 = -2400\,\mathrm{V}$ in the right direction to tune the image position.

contrast characterizing the image quality is then calculated counting the number of ions within (N_{in}) and outside (N_{out}) their expected final positions given by the initial *FoV* and spacing, multiplied with the current magnification. The contrast [1] is then defined by

$$C = \frac{N_{\mathrm{in}} - N_{\mathrm{out}}}{N_{\mathrm{in}} + N_{\mathrm{out}}}. \tag{3.1}$$

With this method negative "contrasts" are possible, values of C are in the range $-1 \leq C \leq 1$. As a criterion for a good configuration a contrast $C > 0.9$ was chosen. Thus each configuration is characterized by the magnification M and the contrast C. After each run, either the geometry itself or the intermediate image positions are changed and M and C are recalculated.

3.8. Geometry and voltage optimization

To determine the final geometry two different approaches were chosen. First, different geometries with varying lens positions, diameters or electrode lengths were tested to reduce aberrations and optimize the quality of the imaging system. In the course of this procedure asymmetric lens designs have been allowed. With three electrostatic lenses a variety of configurations has been tested. This involves the optimization of the individual lens positions, multi-electrode-lens designs or asymmetric lenses.
However, of greater importance to optimize the performance of the ion-optical column is the choice of intermediate image positions. Within the operating range of the lenses

[1]Note that the used definition of the contrast differs from the common definition of contrast making use of intensity values

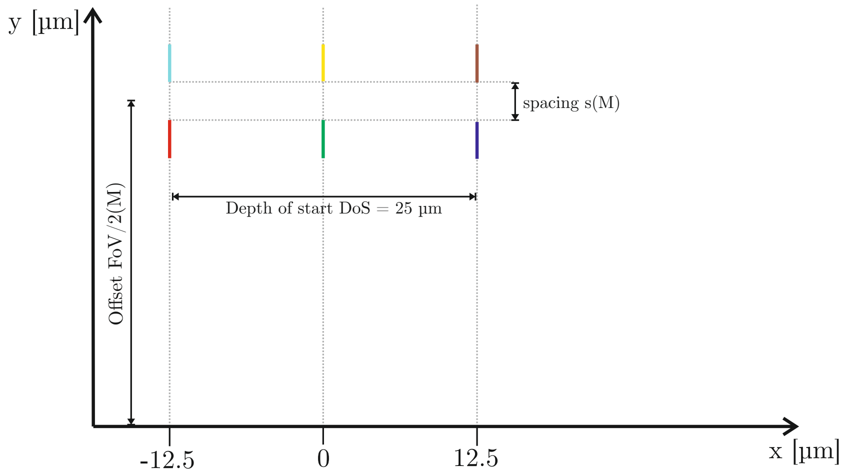

Figure 3.5: Schematic illustration how the contrast is determined. Ions start in six stripes with a depth of start of 25 µm and with a common offset, scaled by the magnification to resemble the maximum field of view. The six stripes are divided into two groups, spaced by a spacing $s(M)$, that is scaled with the magnification according to the detectors resolution limit (100 µm). The initial kinetic energy is KE = 9.3 neV (corresponding to a temperature of $T \approx 160\,\mu\text{K}$ for Rubidium).

that are used, one of the two intermediate image positions can be chosen freely in order to reach a certain magnification. The simulations showed that this degree of freedom can be used to correct for chromatic aberrations in the system. Using a setup with three rotationally symmetric three-cylinder-lenses, it is possible to reach a multitude of magnifications between 80 and 1000 obtaining a high contrast on the detector by shifting the intermediate image position in front of the second lens appropriately.
During the experiment, photo-ionized Rydberg atoms will be extracted from the center of the electric field control by pulsing both the repeller and extractor field plate on ± 500 V, respectively. The initial depth of start of 25 µm, corresponding to the approximate excitation region of Rydberg atoms, causes ions initially slightly further away from the extractor plate to have a higher kinetic energy than ions initially slightly closer to the extractor electrode. This initial energy spread leads to a chromatic aberration that dominates over any other monochromatic effect, for example spherical aberrations in our system. As mentioned in detail in subsection 2.3.5 the chromatic aberration in ion-optical systems consists of two kinds. The axial chromatic aberration with its aberration coefficient C_C which is of most concern when incident angles are large and the chromatic distortion with coefficient C_D, representing the chromaticity of the magnification, which

is of concern when the angles of particle trajectories with respect to the optical axis are small but the rays are comparatively far away from the optical axis.
In the case under consideration the chromatic distortion is the dominant error as incident angles are small due to the fast extraction of ions compared to their initial energy in the neV-regime causing the ion trajectories to be almost parallel to the optical axis when entering the first lens. As described by Rose [HRo09] and Weitsch [Wei60] the chromatic distortion can be compensated using an additional lens and exciting this intermediate lens appropriately. In the case at hand, this means that the contrast can be optimized by shifting the intermediate image in front of the third lens by tuning the voltage at the middle cylinder of the second three-cylinder-lens. The first lens is used to adjust the magnification of the whole microscope by defining the first intermediate image position, automatically setting the proximate object distance to the second lens.

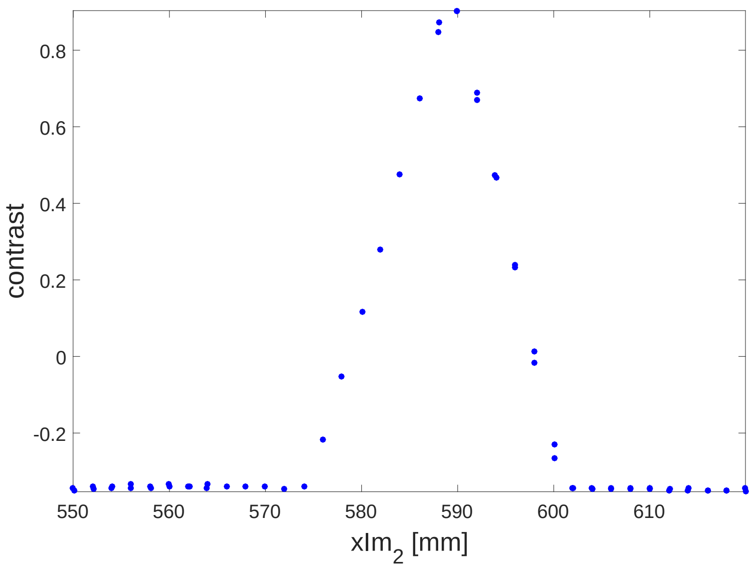

Figure 3.6: Contrast calculated out of the stripe pattern for a fixed intermediate image position $x\mathrm{Im}_1$ as a function of the second intermediate image distance $x\mathrm{Im}_2$. The image position is tuned such that the contrast is maximal by compensating errors arising from the chromaticity of the magnification.

An example of how this voltage tuning affects the contrast in the detector plane is shown in Figure 3.6. The first intermediate image position $x\mathrm{Im}_1$ is fixed thereby approximately determining the magnification, whereas the second intermediate image position $x\mathrm{Im}_2$ is tuned until a maximum contrast of $C > 0.9$ is reached. It can be seen that for each specific intermediate image position $x\mathrm{Im}_1$ a position of the second intermediate image $x\mathrm{Im}_2$ exists where the error arising from the chromatic distortion is best compensated. It should be mentioned that for the determination of the second intermediate image the third lens is turned off. Since the position of the second intermediate image lies inside the third lens, the lens itself influences the position of the intermediate image when it is turned on.

3.9. Alternative imaging methods

An alternative way to image ions with the microscope without being limited in resolution by chromatic aberrations, is to minimize the initial energy spread of ions as a consequence of the extraction with the repeller and extractor plates.

Low extraction voltages One way to minimize the chromatic aberrations in the system is to decrease the extraction voltage. As a consequence, the linear extraction field flattens leading to a smaller kinetic energy difference for ions starting further away from the first lens with respect to ions starting closer to the first lens. It should be mentioned, that the first drift tube voltage has to be adjusted to prevent higher order operating ranges of the first lens. In this case, the MCP potential is reached after the third lens. With low extraction voltages, e. g $\pm$ 10 V, it is possible to image ions with high resolution without needing to shift the second intermediate image inside the third lens to compensate the chromatic distortion. However, ions are more susceptible to stray electric fields.

Pulsed extraction Another way to minimize the initial energy spread is to not only switch on the extraction field, but to ramp it down again before the particles reach the first lens. As a consequence, ions starting at different positions accumulate the same kinetic energy as they are exposed to the extraction field for the same time. Figure 3.7 illustrated the extraction potential for the normal and pulsed mode as well as the kinetic energy the ions accumulate in the extraction potential. It can be seen, that in the pulsed case, the extraction potential suddenly jumps to zero when the field is switched off. In the normal case, the extraction potential is linear over the whole distance to the first lens and ions starting further away accumulate more kinetic energy than ions starting closer to the lens.

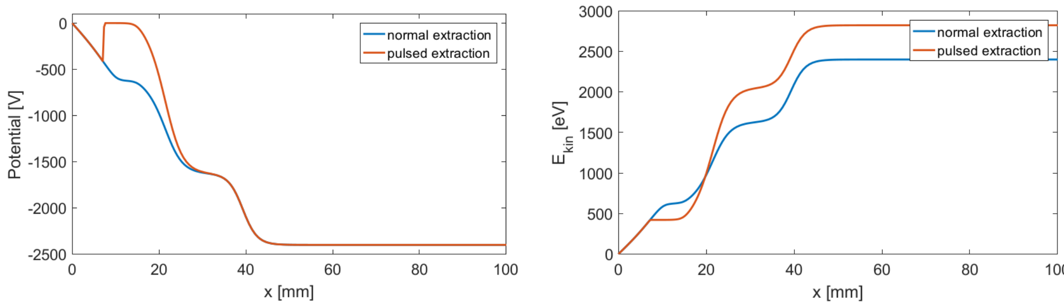

(a) Extraction potential for normal and pulsed mode.

(b) Kinetic energy for normal and pulsed extraction mode.

Figure 3.7: (a) Comparison of the extraction potential in the normal and pulsed extraction mode. (b) Kinetic energy of ions for normal and pulsed extraction mode. Ions accumulate the same kinetic energy independent of their initial position.

In the pulsed extraction mode the kinetic energy difference for an ion starting in the middle of the chamber compared to an ion starting at $x = -12.5\,\mu\text{m}$ can be thereby reduced from 0.65 eV in the normal case to 0.15 eV in the pulsed case. By further adjusting the timing of the switching ramps, this kinetic energy difference is most likely further reduced. Extraction times of ions for e.g. $\pm$ 500 V are on the order of 650 ns from the center of the chamber to the entrance of the first lens.

3.10. Geometry of the ion-optical system

The final geometry that resulted from the simulation described previously consists of three electrostatic three-cylinder lenses. Asymmetric lens designs showed no considerable advantage compared to a rotationally symmetric design as the chromatic aberrations are best compensated by proper choice of the intermediate image positions. A cross section through the final rotationally symmetric electrode geometry used in the simulations to characterize the performance of the ion-optical system is shown in Figure 3.8. To minimize the computational effort, this geometry has been generated using a SIMION ".gem" geometry file with rotational symmetry. Additional elements breaking the rotational symmetry will be discussed later.

The simulated geometry consists of an electric field control with two round plates, the repeller and extractor electrode and a ring resembling the electric field control. In the actual experiment the electric field control consists of six plates. For the simulation this was neglected to maintain the rotational symmetry.

The microscope itself consists of three electrostatic three-cylinder lenses with inner radii of 4.3 mm, 5 mm and 15 mm, respectively. The length from the center of the electric field control, in which the Rydberg atoms are prepared, to the detector plane amounts to 1350 mm.

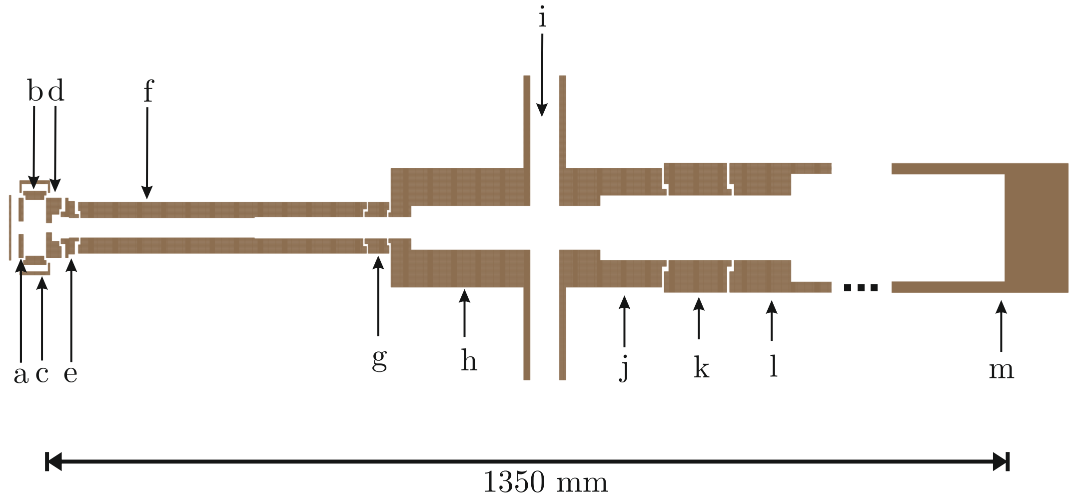

Figure 3.8: Cross section of the simulated rotational symmetric electrode geometry: a) positive repeller electrode, b) electric field control, c) electric field control housing, d) negative extraction electrode, e) first lens, f) drift tube 1, g) second lens, h) drift tube 2, i) valve gap, j) drift tube 3, k) third lens, l) drift tube 4, m) detector plane.

3.10.1. Dimensioning

The exact dimensioning of the electrode geometry used to simulate the performance of the rotationally symmetric setup is listed in Table 3.1. Of importance for the simulation are mainly the inner diameters and lengths of the individual elements.

Element	Inner radius r_i	Length	Distance
Extraction electrode	3.75 mm	3.1 mm	-
Electric field control	13 mm	16 mm	2 mm
Repeller electrode	2 mm 6.2 mm	5 mm 6.5 mm	2 mm 0 mm
First lens	5 mm 4.3 mm	7.2 mm 8.8 mm	1.2 mm 0 mm
Drift tube 1	4.3 mm 5 mm	44.1 mm 7.5 mm	1.2 mm 0 mm
Second lens	5 mm	19.5 mm	1.2
Drift tube 2	5 mm 10 mm	65 mm 57 mm	1.2 mm 0 mm
Lower valve plate	10 mm	6 mm	0 mm
Upper valve plate	10 mm	6 mm	25 mm
Drift tube 3	10 mm 15 mm	20 mm 62.4 mm	0 mm 0 mm
Third lens	15 mm	55 mm	2 mm
Drift tube 4	15 mm 130 mm	104.5 mm 629.5 mm	2 mm 0 mm
Detector	0 mm	3 mm	5 mm

Table 3.1: Dimensions of the ion-optical elements. Only inner radii, lengths and distances between the elements are of importance for the performance of the microscope.

The outer diameter of the upper and lower valve plate with $r_a = 70.5$ mm was chosen such that the ion path is well shielded from the ground given by the outer vacuum parts.

Extraction electrodes The first part of the ion microscope is formed by two round plates with small apertures, the *repeller* and *extractor* plate (Figure 3.8(a) and (d)). The lower repeller electrode is operated with a positive voltage accelerating ions away from this electrode towards the ion microscope itself. The upper extractor electrode is set to a negative voltage attracting ions and routing them through a small aperture into the ion microscope.

Electrostatic lenses The negative extraction electrode simultaneously forms the outer electrode of the first three cylinder lens. The first lens is operated asymmetrically serving as an immersion lens to put the ions on the potential of the first drift tube (which is typically on MCP potential). The lens is the only lens in the system that can be operated in the accelerating mode without requiring voltages exceeding 5 kV. The middle cylinder of the first lens is operated at voltages between -2.7 kV and -3.2 kV. The distance between the individual lens cylinders is 1.2 mm which is large enough to avoid breakdowns (6 kV/mm in UHV [Dru84]). The second and third lens of the microscope are both operated as retarding lenses to avoid voltages above 5 kV. The inner diameters of each lens (8.6

mm, 10 mm and 30 mm) are chosen such that the extend of the ion beam is always at least ten times smaller than the aperture diameter. Larger diameters however lead to larger focal lengths of the lens at constant voltage, setting a limit to maintain the total length of $L = 1350$ mm with a maximum magnification of $M_{\text{max}} \leq 1000$.

Drift tubes The individual lenses are connected with drift tubes. For most of the simulations, the drift tubes are all on the potential of the MCP at -2.4 kV. However, it is possible to operate the drift tubes between first and second lens and second and third lens at a different voltage than the last drift tube that connects the third lens with the detector. The last drift tube is followed by a shielding ring to shield the ion optics from potentials arising from the rear MCP plate and the delay line anode. The drift tube between second and third lens is interrupted due to the valve separating the lower part including the science chamber from the large upper part including the detector. Above and below the valve, two plates with large outer diameters of 70.5 mm are mounted that are also set on the drift tube potential to prevent leakage from the outer ground into the region of particle flux.

4. Characterization of the ion microscope

This section deals with the characterization of the design of the electric field control and the ion microscope which was found via the optimization procedures described in section 3. Of most importance for the performance of the ion microscope are reachable magnifications as well as the achievable resolution for each magnification. The characterization includes necessary lens voltages and resolution tests of the ion-optical column. To make the characterization realistic, the simulations account for mechanical asymmetries in the system, misalignments of lens cylinders and voltage instabilities of the power supplies.

4.1. Electric field control

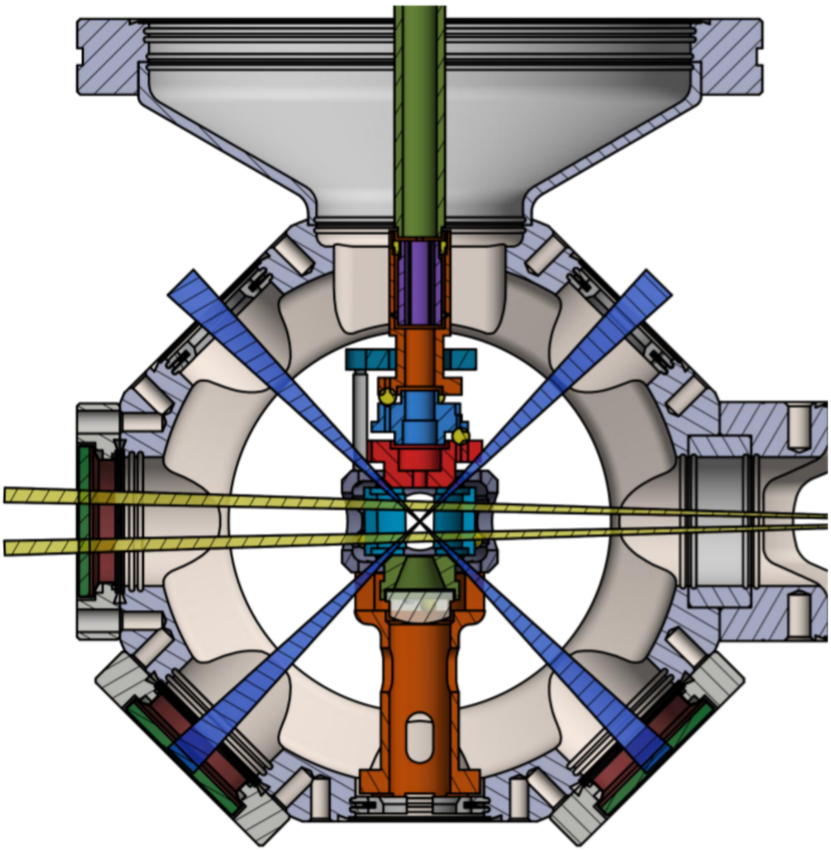

Figure 4.1: Electric field control with six electrodes in total, two round plates to extract ions and four additional plates placed in a ring around the center of the chamber. In-vacuum lens, electric field control and ion-lens are intrinsically aligned and the configuration is almost rotationally symmetric.

A cut through the electric field control is depicted in Figure 4.1. It consists of six electrodes in total, two round plates with small apertures and four additional plates placed on a ring around the center of the science chamber. The lower part of the electric field control consists of a *repeller* electrode from which ions will be repelled and accelerated towards the first ion lens. Beneath this repeller electrode, a high NA in-vacuum lens is mounted. To compensate electric stray fields, four additional field plates (blue) are planned, designed in a way, that still guarantees optical access through the diagonal ports of the science chamber. To extract the ions into the microscope, the last electrode of the electric field control, the *extraction* electrode, is used. This electrode simultaneously forms the first electrode of the first ion lens. To define the aperture size of the extraction electrode, a compromise between shielding the center of the electric field control from fields arising from the middle cylinder of the first ion lens has to be found. However, aberrations introduced by the small diameter of the lens have to be avoided.

Characterization of the electric field control To characterize the electric field control, the electrode configuration was simulated using SIMION. The main objective of these simulations was the determination of the field homogeneity in the center of the chamber.
The conversion factors between applied electrode voltages and electric field in the center of the chamber are listed in Equation 4.1-Equation 4.3 for the three room dimensions. To generate for example a field in $y-$direction a positive voltage has to be applied to the repeller plate and a voltage of negative polarity to the extractor plate.

$$E_x(U)\left[\frac{\mathrm{V}}{\mathrm{cm}}\right] \widehat{=} 0.67\frac{1}{\mathrm{cm}}\cdot U[\mathrm{V}] \tag{4.1}$$

$$E_y(U)\left[\frac{\mathrm{V}}{\mathrm{cm}}\right] \widehat{=} 0.85\frac{1}{\mathrm{cm}}\cdot U[\mathrm{V}] \tag{4.2}$$

$$E_z(U)\left[\frac{\mathrm{V}}{\mathrm{cm}}\right] \widehat{=} 0.66\frac{1}{\mathrm{cm}}\cdot U[\mathrm{V}] \tag{4.3}$$

The residual field in the center of the electric field control when applying 1 V to the first ion lens is $E_x = -2.0\cdot 10^{-6}$ V/cm, $E_y = 1.1\cdot 10^{-6}$ V/cm and $E_z = -1.5\cdot 10^{-7}$ V/cm. Similarly the residual fields in the middle of the chamber when applying 1 V to the planned ITO-coating of the optical lens are $E_x = 1.2\cdot 10^{-8}$ V/cm, $E_y = 1.6\cdot 10^{-8}$ V/cm and $E_z = -2.5\cdot 10^{-10}$ V/cm. These values define the shielding factor of either repeller or extractor plate.

To characterize the homogeneity of electric fields in $x-$, $y-$, and $z-$direction, the maximum and mean deviation from a predefined homogeneous field are calculated using an algorithm that minimizes the deviation from the desired field and unwanted fields in the other two coordinate directions by setting the electrode voltages of the six field plates. Furthermore, the algorithm maximizes a symmetry parameter quantifying the symmetry of the resulting field configuration. The results of this optimization for electric fields in $x-$, $y-$, and $z-$direction are listed in table 4.1 for the two cases when the first

	Max. field deviation			Max. stray fields		
	x	y	z	x	y	z
Ion lens off	$1.8 \cdot 10^{-3}$	$6.3 \cdot 10^{-4}$	$1.5 \cdot 10^{-3}$	$1.9 \cdot 10^{-3}$	$6.3 \cdot 10^{-4}$	$2.0 \cdot 10^{-3}$
Ion lens on	$2.3 \cdot 10^{-3}$	$6.9 \cdot 10^{-4}$	$2.3 \cdot 10^{-3}$	$2.3 \cdot 10^{-3}$	$1.1 \cdot 10^{-3}$	$2.3 \cdot 10^{-3}$
	Mean field deviation			**Mean stray fields**		
	x	y	z	x	y	z
Ion lens off	$8.4 \cdot 10^{-4}$	$2.3 \cdot 10^{-4}$	$5.8 \cdot 10^{-4}$	$6.4 \cdot 10^{-4}$	$2.0 \cdot 10^{-4}$	$6.4 \cdot 10^{-4}$
Ion lens on	$7.6 \cdot 10^{-4}$	$2.5 \cdot 10^{-4}$	$7.1 \cdot 10^{-4}$	$6.8 \cdot 10^{-4}$	$2.9 \cdot 10^{-4}$	$6.7 \cdot 10^{-4}$

Table 4.1: Deviations from desired electric field when applying fields in $x-$, $y-$, and $z-$direction when the ion lens is turned off an when the ion lens is set to $-3.3\,\mathrm{kV}$. Deviations are calculated using an algorithm that minimizes the deviation from the desired field and minimizes unwanted fields in the other two coordinate directions by setting the electrode voltages of the six field plates. The values refer to a volume of $\mathrm{V} = (600\,\mu\mathrm{m})^3$ around the center of the science chamber. Besides, the algorithm maximizes a symmetry parameter quantifying the symmetry of the resulting field configuration.

ion lens is switched on or off. The values refer to a volume of $\mathrm{V} = (600\,\mu\mathrm{m})^3$ around the center of the science chamber.

4.2. Benchmarking the microscope

To characterize the performance of the ion microscope, the previously introduced simulation procedure is used. Figure 4.2 shows the lattice constant ($s(M)$) and the field of view (FoV) employed in the simulations as a function of the total magnification M.
The lattice constant and the offset of the stripe pattern (defining the field of view) are thereby scaled according to the magnification, the resolution limit of the detector (assumed to be $50\,\mu\mathrm{m}$) and the size of the active detection area which has a diameter of $d = 40\,\mathrm{mm}$. Thus, for a magnification of $M = 1000$ the lattice constant is $50\,\mathrm{nm}$ and the offset of the pattern is $FoV/2 = 17\,\mathrm{mm}$. The assumed diameter of $d = 34\,\mathrm{mm}$ is thereby smaller than the active area of the detector with 40 mm, hence avoiding the outer most region of the detector. Simulated field of views lie in the range of $400\,\mu\mathrm{m}$ for low magnifications around $M = 100$ down to $\approx 30\,\mu\mathrm{m}$ for $M > 1000$. The offset of the stripe pattern is defined by the maximum field of view to be imaged on the detector. The simulated lattice constants are in the range of $600\,\mathrm{nm}$ for $M \approx 68$ and $40\,\mathrm{nm}$ for $M \approx 1250$, hence determining the theoretical resolution of the microscope to this minimum lattice constant. However, it should be pointed out, that the actual resolution will be limited by mechanical asymmetries resulting from the alignment of the microscope or voltage instabilities of the power supplies. Effects diminishing the actual resolution of the ion microscope will be discussed below.

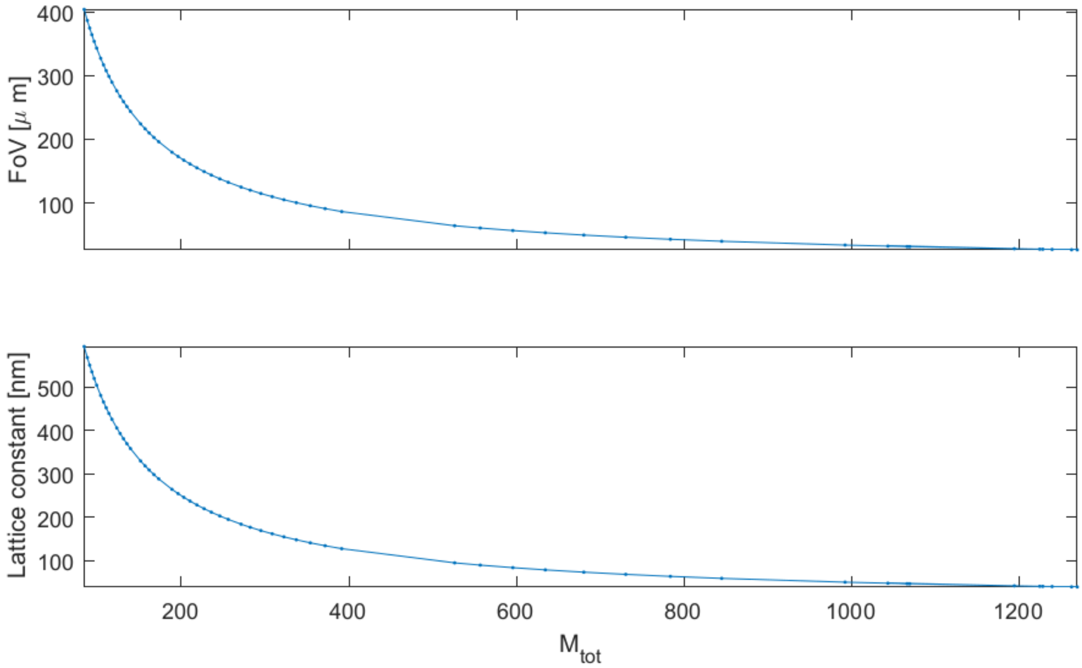

Figure 4.2: Field of view and lattice constant as a function of the total magnification M_{tot}. Both quantities are scaled with the magnification according to the detector size and detector resolution expected. In the ideal rotationally symmetric systems structures with distances down to around 40 nm could be imaged with the highest possible magnification.

4.3. Magnifications

In Figure 4.3 the magnifications after the first lens (M_1), second lens (M_2), third lens (M_3), the total magnification M_{tot} and the second intermediate image distance $x\text{Im}_2$ are plotted versus the first intermediate image distance $x\text{Im}_1$. Both intermediate image distances are measured with respect to the center of the electric field control ($x = 0$). All of the plotted configurations of $x\text{Im}_1$ and $x\text{Im}_2$ exhibit a contrast of $C > 0.9$ when propagating the beforehand mentioned stripe pattern.
It can be seen that the second intermediate image distance $x\text{Im}_2$ decreases when increasing the first intermediate image distance $x\text{Im}_1$, tantamount with increasing the magnification. The position of the third lens is fixed at $x_{\text{L}} = 554$ mm from the center of the electric field control meaning that the second intermediate image has to be shifted inside the third lens, into the region where the electric field strongly varies, to compensate for the chromatic distortion in the setup. Furthermore it is conspicuous, that for lower magnifications the position of the second intermediate image has to be far inside the third lens whereas for large magnifications ($M > 800$) the second intermediate image position has to lie near the entrance of the third lens. All the image positions are calculated with the next respective lens turned off. Since the position of the second intermediate image

lies inside the third lens, the lens itself influences the position of the intermediate image when it is turned on.
In addition, Figure 4.3 elucidates how the total magnification M_{tot} is distributed on the three lenses. The magnification of the first lens M_1 is mainly fixed by the object distance as the ion optic can not be placed any closer to the atomic cloud to maintain optical access for laser manipulation of the atoms. Therefore the first magnification is comparatively small. The second and third lens both possess a maximum magnification of around $M \approx 16$. By varying the intermediate image position in front of the second lens, a wide range of magnifications $2.5 \leq M_2 \leq 16$ can be covered to adjust the total magnification of the ion microscope.

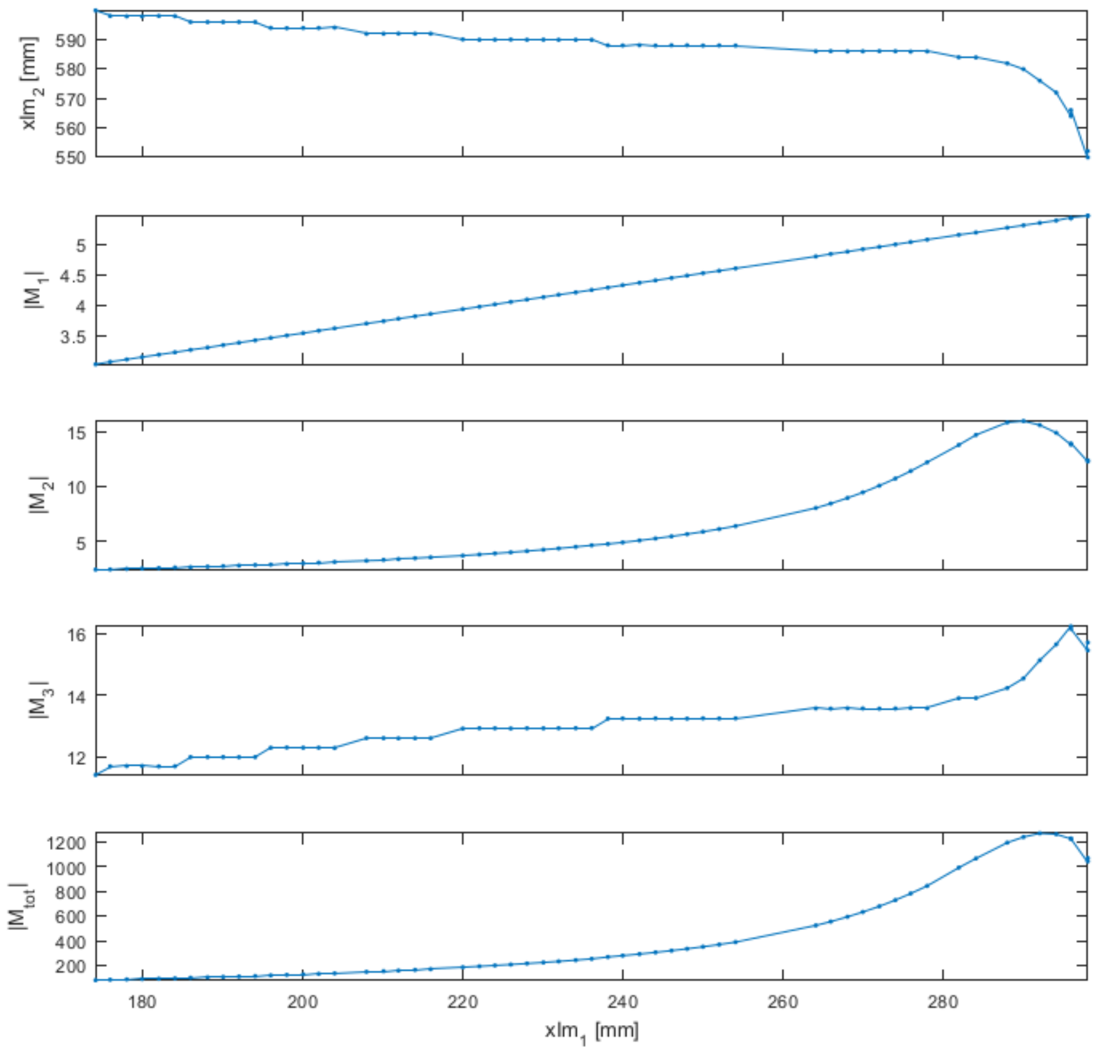

Figure 4.3: Intermediate image distance $x\mathrm{Im}_2$ and magnifications M_1 after the first lens, M_2 after the second lens, M_3 after the third lens and M_{tot} as the total magnification of the ion microscope as a function of the intermediate image distance $x\mathrm{Im}_1$. $x\mathrm{Im}_1$ is used to tune the magnification. Magnifications up to around $M = 1250$ are possible. For all simulated points, the contrast C is larger than 0.9.

Between $M_{\mathrm{tot}} = 390$ and $M_{\mathrm{tot}} = 530$ a gap occurs where the contrast of the stripe pattern does not reach values above $C > 0.9$, most likely attributed to an artifact of the simulation algorithm.
Table 4.2 highlights the range of possible magnifications and summarizes the corresponding lens voltages on each middle cylinder of the three lenses. In every configuration the extractor and repeller plate are set to ± 500 V respectively and every drift tube voltage

is set to $-2.4\,\text{kV}$.

Magnification M	x**Im**$_1$ **[mm]**	x**Im**$_2$ **[mm]**	V_1 **[V]**	V_2 **[V]**	V_3 **[V]**
84	174	600	-3116.2	-1297.7	-88.8
114	192	596	-3077.1	-1253.2	-94.8
203	224	590	-3024.9	-1119.5	-106.0
309	244	588	-2999.9	-994.0	-110.5
391	254	588	-2989.1	-906.7	-110.5
526	264	586	-2979.1	-790.9	-115.2
729	274	586	-2970.0	-633.6	-115.1
988	282	584	-2963.3	-465.1	-120.6
1265	292	876	-2955.3	-238.4	-147.6

Table 4.2: Extract of possible magnifications of the ion microscope with the respective intermediate image positions $x\text{Im}_1$ and $x\text{Im}_2$ and the lens voltages on the middle cylinders of each three-cylinder lens V_1, V_2 and V_3.

4.4. Lens voltages

In Figure 4.4 the lens voltages for the lens cylinders of all three electrostatic lenses V_1,V_2 and V_3 are shown as a function of the total magnification M_{tot}. The first lens is the only lens that can be operated in the accelerating lens mode. Lens voltages vary between $-3100\,\text{V} \leq V_1 \leq -2950\,\text{V}$. With increasing magnification the voltage of the first lens decreases. As a consequence, the focal length increases and the first intermediate image shifts closer to the next lens leading to a shorter second object distance and hence a larger magnification of the following lens. Both second and third lens are operated in the retarding lens mode with voltages ranging from $-1.3\,\text{kV}$ to around $-300\,\text{V}$ for the second lens and $-150\,\text{V}$ to about $-90\,\text{V}$ for the third lens. Accelerating lens voltages for both lenses would exceed $10\,\text{kV}$ which is not feasible for practical applications in the existing setup. The voltage of the third lens is the only voltage that has to be increased with increasing magnification. At the same time, the second intermediate image position decreases for large magnifications. This is most likely attributed to the fact that the two lenses can not be treated independently as the second intermediate image is located far inside the third lens. Thus, the third lens itself influences the second intermediate image when turned on.

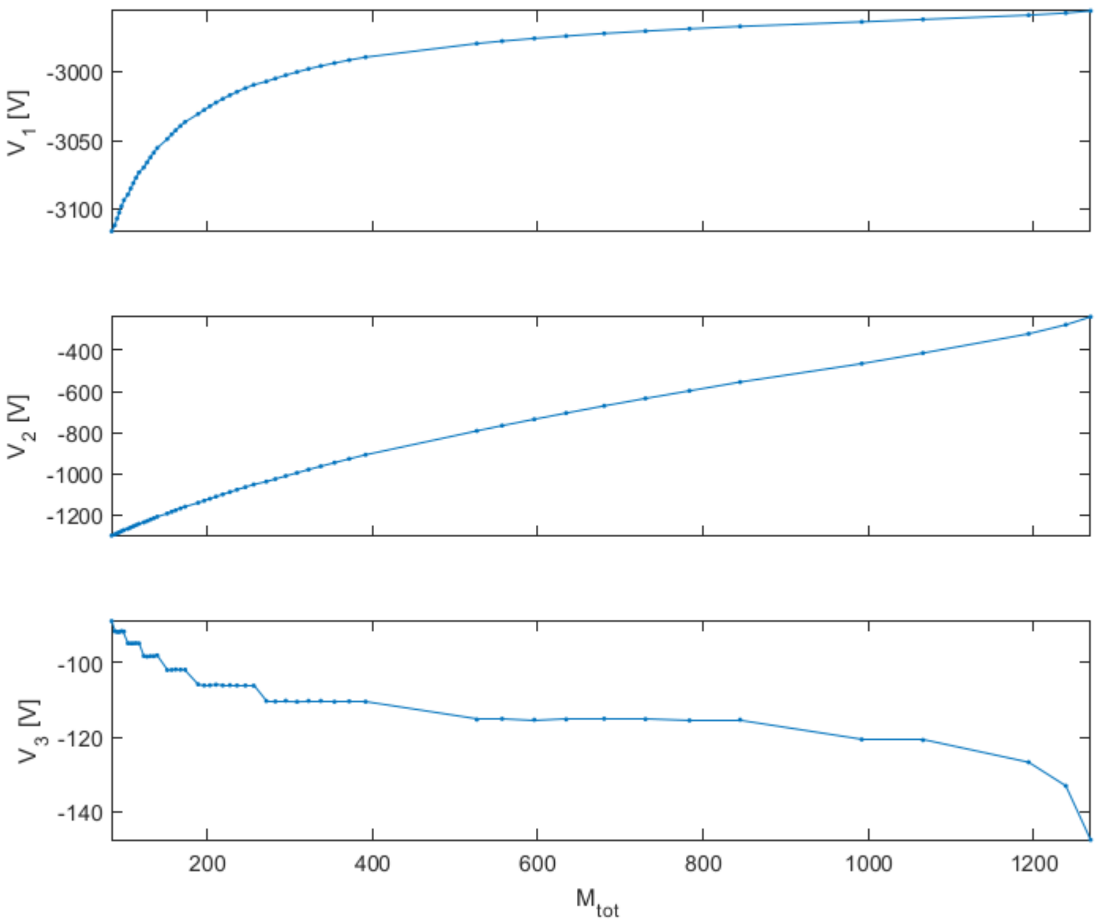

Figure 4.4: Lens voltages for the lens cylinders of all three electrostatic-lenses V_1,V_2 and V_3 as a function of the total magnification M_{tot} of the microscope. Only the first lens is operated in the accelerating lens mode with voltages on the order of $-3\,\mathrm{kV}$. The second and third lens are both operated in the retarding mode with voltages ranging from $-1.3\,\mathrm{kV}$ to around $-300\,\mathrm{V}$ for the second lens and $-150\,\mathrm{V}$ to about $-90\,\mathrm{V}$ for the third lens. Accelerating lens voltages for second and third lens would be above $10\,\mathrm{kV}$.

4.5. Electrostatic potential

Figure 4.5 shows the variation of the potential on the optical axis ($y = z = 0$) through the whole electrode geometry for five different magnifications. Ions are extracted with a linear potential and accelerated into the first lens. The three lens transitions reflect in drastic changes of the electric potential. In the regions between the lenses the electrostatic potential is constant and given by the drift tube voltage.

A more illustrative representation in the two dimensional case is shown in Figure 4.6. It shows the potential landscape of the electrode geometry as simulated by SIMION.

Electrodes are drawn in black and the ion trajectories lie on a surface whose height is given by the potential resulting from the voltages applied to the electrodes. As an example a configuration with $M = 1250$ is shown. The representation with equipotential lines reveals the spatial progression of the potential energy of the system. It is apparent that the interruption of the drift tube between second and third lens, evoked by the valve to separate the lower from the upper vacuum part, has no influence on the ion trajectories due to the fact that the large plates ensure a constant potential around the optical axis.

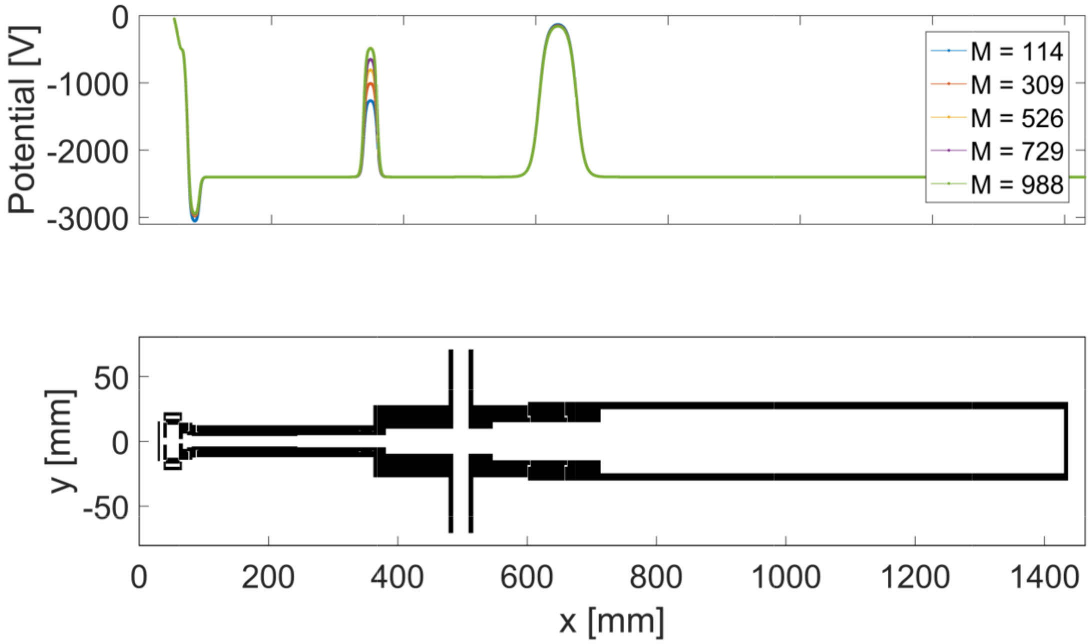

Figure 4.5: Upper part:Electric potential along the optical axis ($y = z = 0$) of the ion microscope for five different magnifications. The three lens transitions manifest themselves in a drastic change in the electric potential. In between the lenses the potential is constant and given by the drift tube voltage of $-2.4\,\mathrm{kV}$. Lower part: Geometry of the ion microscope to reference the lens positions.

4.6. Image deviations

An imaging error that can not be easily compensated is the field curvature. As described in subsection 3.7 the propagation of different particle groups allows the determination of the Gaussian image plane and besides gives a measure for the field curvature of the final image. The image deviation, shown for the two intermediate images and the final image on the detector in Figure 4.7 is calculated by taking the maximum difference (in the horizontal direction) of intersecting beams in the individual bundles of three rays.

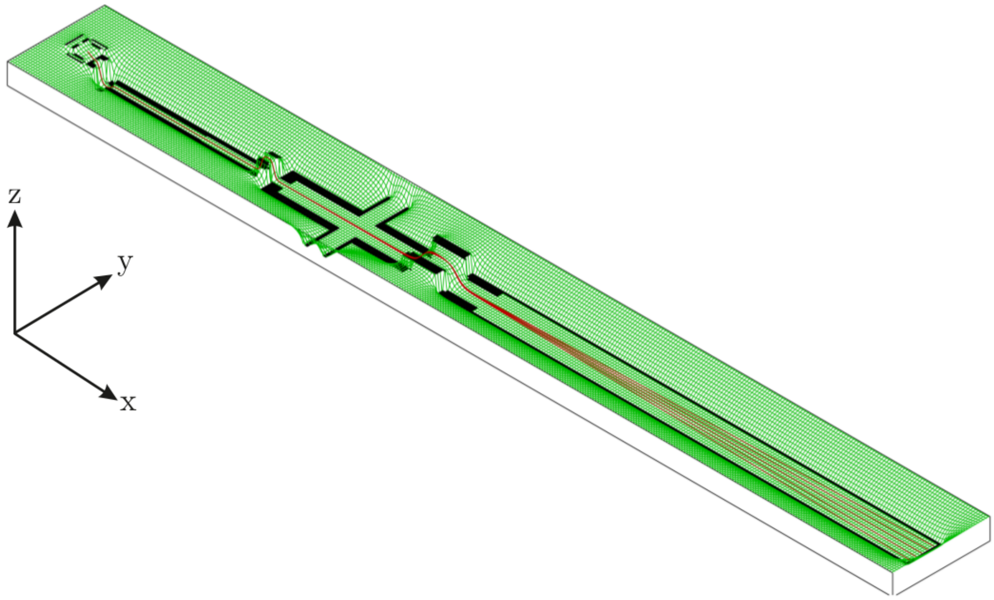

Figure 4.6: Potential landscape through the ion microscope for the maximum magnification of $M \approx 1250$: the image shows he potential landscape of the electrode geometry as simulated by SIMION. Ion trajectories are shown in red. The height of the surface corresponds to the potential energy inside the ion microscope.

Note, that this value does not represent the radius of the Petzval surface, however it still gives a measure for the curvature of the final image. In Figure 4.7 it can be seen that the curvature of the image increases with growing number of intermediate images and that the final image suffers from large image deviations and therefore field curvature. It shall be pointed out, that the calculation of the image deviation, especially for the last image, suffers from the finite simulation quality that was used to keep the simulation time reasonable. However, the present field curvature is negligible in the special case at hand as image rays are almost parallel after the extraction in the science chamber.

Propagation dynamics Another property of the imaging system which is worth to mention are the propagation dynamics. Figure 4.8 shows the arrival times of three test patterns on the detector. The three test patterns start at $x = -12.5\,\mu\text{m}$, $x = 0\,\mu\text{m}$ and $x = 12.5\,\mu\text{m}$ and consist of three circles, with an initial extend to completely fill a diameter of $d = 34\,\text{mm}$ on the detector at the chosen magnification of $M = 1263$. They

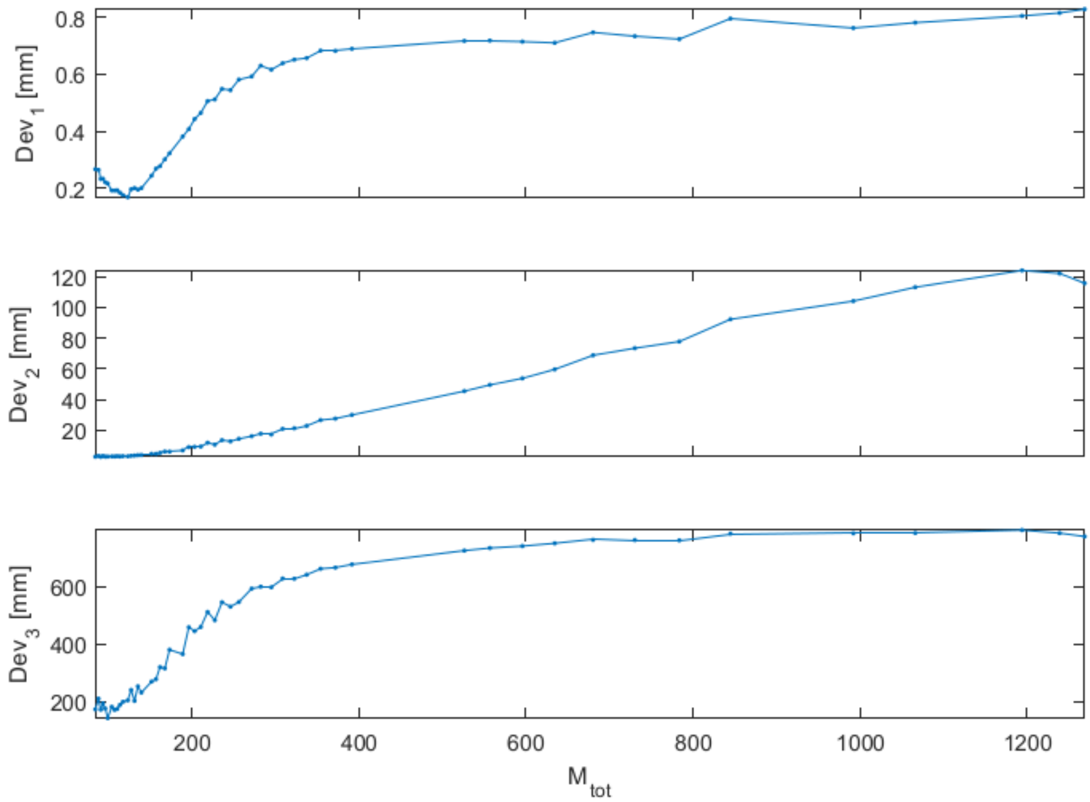

Figure 4.7: Calculated image deviations for the first, second and last image as a function of the total magnification M_{tot}. The deviations are calculated as the maximum difference between the image position and the crossing points of outer image rays. Despite these large image deviations, the present field curvature is negligible in the special case at hand as image rays are almost parallel after the extraction in the science chamber.

are propagated through the rotationally symmetric setup. Figure 4.8(a) shows the initial and final test pattern in the y-z plane (detector plane).

Figure 4.8(b) illustrates the difference in arrival times for particles at different starting positions. Ions closer to the optical axis reach the detector plane faster than ions further away from the optical axis. The temporal difference in arrival times for the inner and outer circle is on the order of 4 ns. Ions initially starting further away from the first lens reach the detector faster than ions starting at $x = 12.5\,\mu\text{m}$, initially closer to the ion lens. At the first moment counter-intuitive, this fact can be easily explained by the larger amount of kinetic energy ions accumulate if they are initially further away from the ion lens.

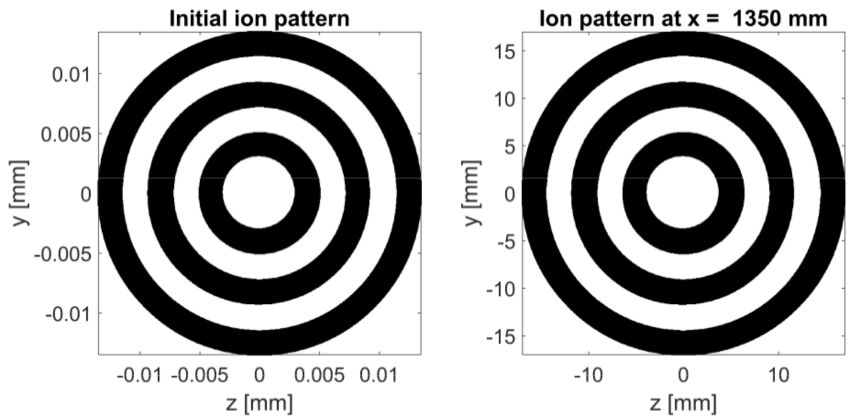

(a) Initial and final test pattern with three circles.

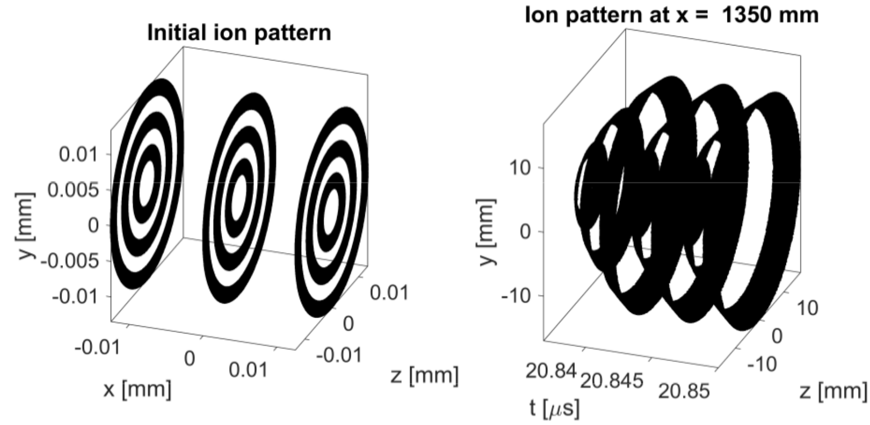

(b) Initial and final test patterns of three circles. Left: Three test patterns are propagated starting at $x = -12.5\,\mu\text{m}$, $x = 0\,\mu\text{m}$ and $x = 12.5\,\mu\text{m}$. Right: Final positions in x and y versus arrival time in µs.

Figure 4.8: (a) Image of three test patterns before and after propagation through the setup, each consisting of three circles starting at $x = -12.5\,\mu\text{m}$, $x = 0\,\mu\text{m}$ and $x = 12.5\,\mu\text{m}$. The initial extend of the circles was chosen to fill the active area of the detector at the chosen magnification of $M = 1260$. (b) Left: Initial test patterns at their respective starting position giving a total depth of start of $25\,\mu\text{m}$. Right: Final positions of ions in the pattern and their arrival times on the detector. Ions starting further away from the first lens reach the detector faster than ions initially closer to the first ion lens.

4.7. Tolerance requirements

In the following subsection effects that diminish the resolution of the imaging are discussed. This includes mechanical asymmetries that have to be included into the setup to ensure optical access through the diagonal ports as well on the microscope axis. Besides, effects of lateral displacements of individual lens cylinders are outlined. These displacements affect the ion trajectories and the imaging quality. Furthermore, electronic stability criteria like the manageable noise characteristics of voltage supplies or the effect of switching the extraction voltage with finite rise times are investigated.

4.7.1. Mechanical asymmetries

The alignment accuracy of the individual lens cylinders is limited by the manufacturing precision of the CNC lathe and milling machine used to fabricate the electrodes. The final concentricity of the lens however sets the actual performance to be achieved in practice. Lateral displacements to the optical axis, especially of the middle cylinder of each lens, introduce beam displacements, coma and astigmatism [Orl08; Mun88]. In fact, the beam displacement caused by lateral displacement of the middle cylinder in the case under consideration, especially concerning the first lens, is severe. For 50 µm lateral displacement of the middle cylinder of the first lens operating at the maximum voltage of $V_1 = -3050\,\mathrm{V}$, the beam shifts 4.96 µm radially per mm distance in axial direction. This displacement corresponds approximately to the precision that can be achieved with the available machining precision in the faculty-own mechanics workshop. The beam displacement thereby depends on the applied voltage on the lens and is higher the stronger the lens is operated. Over the whole distance of the microscope this corresponds to a lateral displacement of an initially central beam starting on the optical axis of $\Delta y = 6.7\,\mathrm{mm}$ on the detector. This simulation however assumes that both second and third lens are in perfect concentric alignment. Therefore, it is essential to be capable of correcting any beam displacements arising from lateral misalignment of lens cylinders. The simplest way is to add deflecting elements after each lens, whose design and operation principle will be discussed below.

4.7.2. Deflection elements

The ability to correct beam displacement introduced by lateral misalignment of lens cylinders can be provided by using deflection elements after each lens. The idea is to have four plates comparatively close after each lens to correct the position of the ion beam to centrically enter the next lens. In its simplest embodiment, an electrostatic deflector consists merely of two parallel plates of differing electrostatic potential [Ard62; BRW87]. Although such simple deflector designs do deflect the ion beams, they typically add undesirable beam distortion effects [DAW99].

An ideal ion beam deflector adds a transverse velocity component to each ion passing through it that is some fixed percentage of the ion's axial velocity component through the deflector. However, beam distortion in simple deflection geometries arises from the entry transition field that differentially changes the kinetic energy of each ion to match the potential at its point of entry in the transverse deflection field. In consequence, ions will be differentially accelerated or decelerated according to their transverse position when entering the deflector. Decelerated ions take longer to traverse the deflector and gain a higher transverse velocity component than accelerated ions. Thus, the focal point of an electrostatic lens will be shifted back towards the deflector due to the transverse velocity difference.

The key to reduce this type of deflector distortion is therefore to reduce the differences in transverse ion velocities for different entry positions. The fractional change in transverse velocity ($\Delta v_T/v_{T0}$) between an ion offset at a distance r from an ion located on the axis in a transverse electrostatic field of E can be approximated with

$$\frac{\Delta v_T}{v_{T0}} = \frac{1}{\sqrt{1+\frac{\Delta E_{\mathrm{kin}}}{E_{\mathrm{kin},0}}}} - 1 = \frac{1}{\sqrt{1+\frac{Er}{E_{\mathrm{kin},0}}}} - 1 \tag{4.4}$$

$$\frac{\Delta v_T}{v_{T0}} \approx -\frac{1}{2}\frac{\Delta E_{\mathrm{kin}}}{E_{\mathrm{kin},0}} = -\frac{1}{2}\frac{Er}{E_{\mathrm{kin},0}} \tag{4.5}$$

where ΔE_{kin} is the change in ion kinetic energy relative to the ion on the optical axis with energy $E_{\mathrm{kin},0}$ and velocity v_{T0}.

Equation 4.4 and Equation 4.5 show that the easiest way to reduce the induced fractional kinetic energy difference is to lower the transverse electrostatic potential gradient (E) of the deflector. This implies that the deflector length must be increased to retain the same beam deflection. Besides, it should be guaranteed that the electrostatic field between the deflection plates is linear, hence avoiding penetration of external fields into the region between the plates. Therefore, field termination electrodes are desirable at the entrance and exit of a deflection stage. In case of the ion microscope design this means, that the deflection stages have to be sufficiently far away from the lens transitions to ensure a linear deflection element but yet have to be close enough to keep the beam displacement introduced by the lateral misalignment of the lens cylinders as small as possible, ensuring that correcting the beam angle with one deflector set after each lens is sufficient.

The final design of the deflection elements, that are implemented after each lens, is shown in Figure 4.9. It consists of four plates in a cylindrical configuration with an inner diameter of $d_i = 10\,\mathrm{mm}$ and a length of $L = 25\,\mathrm{mm}$ in a distance of $d = 25\,\mathrm{mm}$ from the middle of the first lens and second lens, respectively. For the third lens the inner diameter is $d_i = 30\,\mathrm{mm}$ and the length $L = 50\,\mathrm{mm}$. The deflection unit is placed in a distance of $d = 50\,\mathrm{mm}$ away from the middle of the third lens. Figure 4.9 shows a drawing of the first microscope part as well as the geometry that is used for further simulations with SIMION.

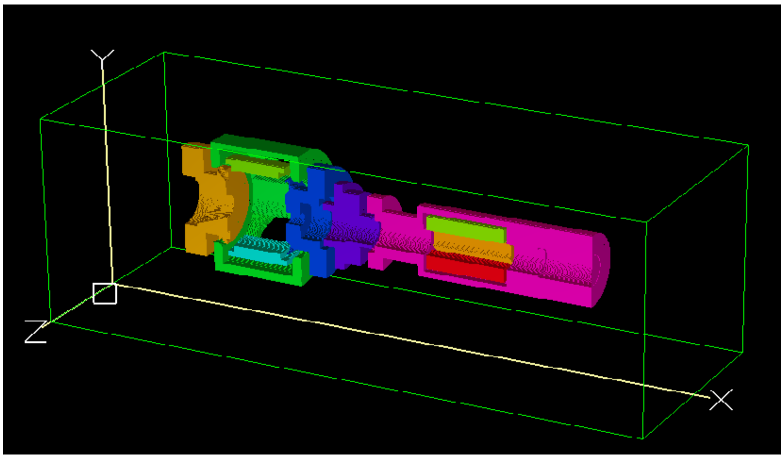

Figure 4.9: Geometry used for the simulations in SIMION. Four deflection plates after the each lens are included to correct for lateral misalignments of lens cylinders.

Adjustment of the simulated geometry The introduction of deflection plates to the simulated geometry breaks the rotational symmetry that was used to minimize computational effort. To adapt a realistic design of the final geometry, holes in the electrode housing as well as in repeller and extractor plate are included for optical access. Besides, the electric field control is split into four field-plates. Deflection plates are added after each of the three lenses with inner diameters to match the diameter of the respective lens.

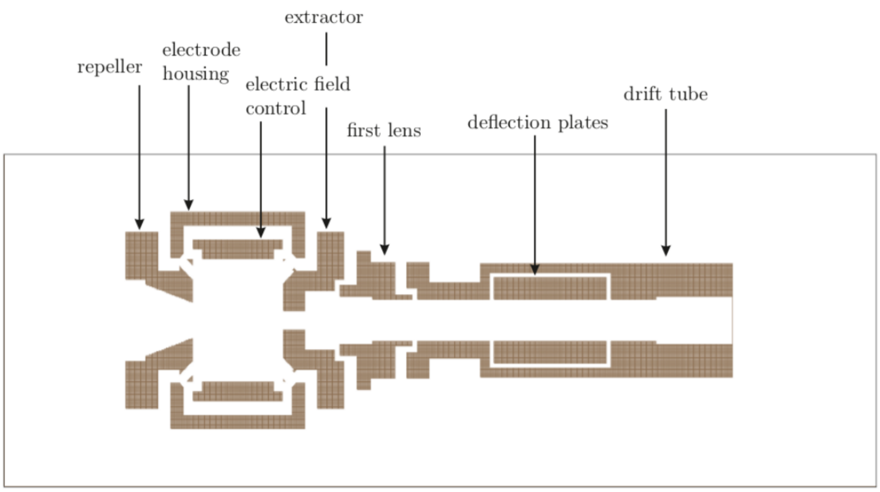

Figure 4.10: Cut throw the first part of the setup. Repeller and extractor plate including diagonal holes for optical access are shown as well as the first lens and the first four deflection plates after the lens to correct for mechanical asymmetries influencing the ion trajectories through the setup.

Figure 4.10 shows a cut through the first part of the setup where the diagonal holes through repeller and extractor are explicitly illustrated.

4.7.3. Misalignments of lens cylinders and total lenses

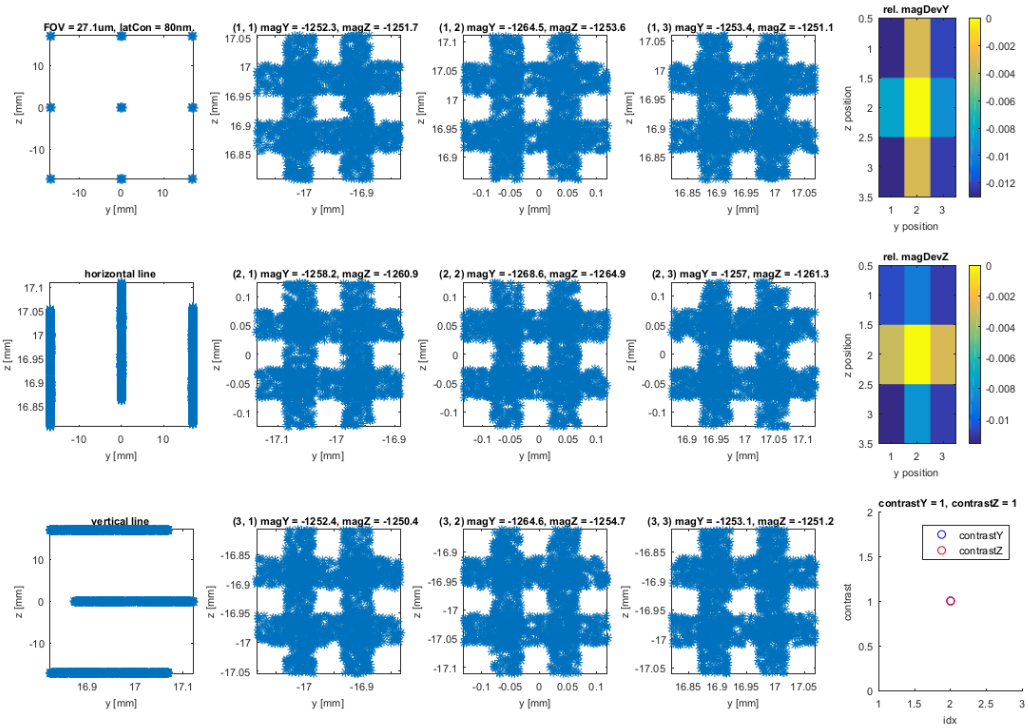

Figure 4.11: Example of a propagated test pattern consisting of nine rhombi with 400 ions per stripe at a magnification of $M = 1250$. For each rhombus a local magnification is calculated as well as a contrast in $y-$ and $z-$direction with two rhombi per stripe. The contrast given in the bottom right corner is the average of all individual rhombi contrasts.

The impact of mechanical asymmetries on the resolution of the ion microscope is simulated by displacing individual lens cylinders. Thus, the performance of the deflection elements after each lens is characterized. To probe the resolution of the system another method extending the contrast evaluation via a simple stripe pattern (see section 4) has been developed using nine rhombi consisting of 400 ions per stripe, i.e. 1600 ions per rhombus. The rhombi are placed with equal spacing between $-FoV/2 \leq y \leq + FoV/2$ and $-FoV/2 \leq z \leq + FoV/2$. The lattice constant scales again with the magnification according to the detector resolution. With this test pattern a contrast in $y-$ as well as in $z-$direction can be evaluated giving rise to imaging errors like astigmatism or coma. An example of a propagated test pattern at a magnification of $M \approx 1250$ is shown in Figure 4.11. For each rhombus a local magnification is calculated and the deviation to the magnification of the central rhombus is evaluated giving a measure for the spatial dependance of the magnification.

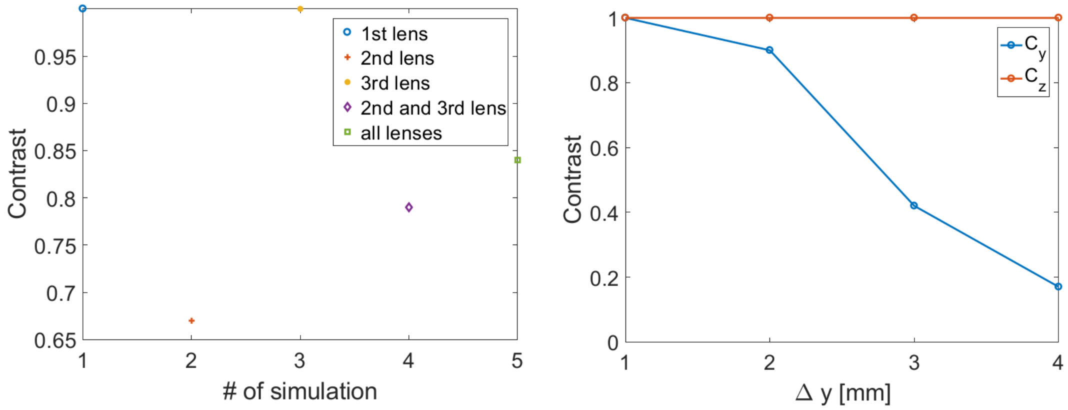

(a) Effect of lateral displacement of lens cylinders on the contrast.

(b) Effect of displacing the whole upper microscope part with respect to the lower part

Figure 4.12: Testing the ion microscope on mechanical displacements. (a) Lateral displacement of individual lens cylinders by $\Delta y = 50\,\mu\text{m}$. (b) Total displacement of the upper microscope part (above the valve) with respect to the lower microscope part in y-direction.

Figure 4.12(a) illustrates the effect of a lateral displacement of the middle cylinder of each lens by $\Delta y = 50\,\mu\text{m}$ on the contrast. A displacement of single cylinders (first lens, second and third lens separately), a displacement of two of three lens cylinders and the displacement of all three lens cylinders are simulated. The lateral displacement of $50\,\mu\text{m}$ corresponds to the approximate precision for the concentricity of the lens cylinders to be achieved. It can be seen, that the displacement is most critical for the middle cylinder of the second lens which can be explained with the combination of the small diameter of the lens bores and the larger image to lens diameter ratio compared to the first lens. For the third lens, lateral displacement is least critical as the inner diameter of the lens is three times larger than for the first and second lens. The deflection plates are used to correct the induced beam displacement by centering the ion beam to the intermediate image position of the next lens. Using four deflection plates after each lens offers the ability to correct either for displacement or for angular deviations. Therefore, the deflection plates are placed as close as possible after the lenses keeping the induced beam angle small.

Figure 4.12(b) illustrates the effect of a total displacement of the upper microscope part containing the third lens and the detector with respect to the lower part below the valve. It can be seen that the deflection plates allow for correcting a total displacement of up to around 2 mm which is reachable with the expected alignment precision of the microscope.

Magnification	$V_{\textbf{Deflection 1}}$	$V_{\textbf{Deflection 2}}$	$V_{\textbf{Deflection 3}}$
410	$\pm$ 5.468 V	$\mp$8.164 V	$\mp$3.339 V
770	$\pm$ 5.273 V	$\mp$10.010 V	$\mp$3.281 V
1250	$\pm$ 5.195 V	$\mp$9.258 V	$\mp$4.043 V

Table 4.3: List of deflection voltages at each deflection stage for three different magnifications $M = 410, 770$ and 1250. All voltages have to be added to $-2.4\,\mathrm{kV}$ (floating voltage of the deflection plates).

Δy [mm]	$V_{\textbf{Deflection 2}}$ [V]
1	$\pm$ 5.078
2	$\pm$ 9.453
3	$\pm$ 13.906
4	$\pm$ 18.281

Table 4.4: List of deflection voltages to correct a total displacement of the upper microscope part.

Table 4.3 gives an example for the deflection voltages needed to correct the beam displacement induced by the lateral displacement of lens cylinders for three magnifications $M = 410, 770$ and 1250. All deflection plates will be floating on $-2400\,\mathrm{V}$ in the experiment, the listed voltages have to be added to the respective plates. It can be seen, that voltages below $V_{\mathrm{Deflection}} = 10\,\mathrm{V}$ are sufficient. Table 4.4 shows the necessary deflection voltages at the second deflection stage to correct for the misalignments used in the simulation. It becomes apparent, that deflection voltages are of the same order compared to voltages to correct for the lateral displacement of lens cylinders.

4.7.4. Switching jitter

To extract ions from the science chamber, repeller and extractor plate have to be switched on, whereas all other microscope voltages are constant during one experimental cycle. Therefore, the effect of a finite rise time of the electric field when switching on the repeller and extractor as well as a jitter between the repeller and extractor plates are included in the simulations. For simplicity a linear electric field ramp for both plates is assumed. A rise time of $t_r = 10$ ns and a jitter between both plates of $t_j = 1\,\mathrm{ns}$ have no influence on the imaging properties of the system.

4.7.5. Voltage stability

As a last analysis of the performance of the ion microscope the voltage stability of the power supplies, required to retain good imaging properties, is examined. Different parts of the microscope like electric field control, lens cylinders or deflection plates are assigned with either an absolute or relative noise level. Thus, the applied voltages on the electrodes vary for each ion.

Drift tubes The least influence on the imaging quality of the ion microscope originates from noise on the drift tube voltages as this will be a common noise that only affects the voltage ratio at the lens transitions leading to a minimally altered focal length of the lens.

Common noise on drift tube voltages is therefore neglected as the effect of a changing focal length is simulated by adding a relative noise level to the individual lens cylinders.

Lens cylinders Noise on the middle cylinders of each lens has roughly the same influence as noise on drift tube voltages. For each ion the ratio of V_2/V_1 will differ leading to slightly differing focal lengths. However, the image quality is barely affected by this effect as can be seen from the contrasts listed in Table 4.5. Noise on the lens cylinders up to a relative level of 10^{-4} is simulated without noticeably affecting the resolution of the test pattern on the detector.

Electric field control Absolute noise on the (ideally) grounded four electric field plates introduces inhomogeneities in the extraction field that significantly reduce the image quality at a certain noise level in the range of $V_{\mathrm{noise,pp}} = 10\,\mathrm{mV}$ yielding a contrast of $C = 0.66$. Even small quadrupole fields leading to deviations from the homogenous extraction field affect the imaging qualities as the ions initial kinetic energy is in the neV-regime and small electric field deviations influence the individual trajectories.

Deflection plates The deflection plates after each lens in the setup are the most sensitive part regarding voltage instabilities of the power supplies. This effect arises from the small deflection voltages required to correct for beam displacements. Owing to the comparatively large length of the deflection plates to minimize beam distortion, the absolute noise level of the power supplies has to be in the range of maximum 2 $\mathrm{mV_{pp}}$ as can be seen from the data in Table 4.5. To give an example of the effect of voltage instabilities of the deflection stages, a voltage difference of + 1 mV at the +y-deflection plate of the first deflection stage results in a displacement of an on-axis ion beam of $\Delta y \approx 27\,\mu\mathrm{m}$ in the detector plane at a magnification of $M \approx 1000$. At an aspired resolution of 100 nm this corresponds to a fourth of the lattice constant of the test pattern. However, the first deflection stage is the most sensitive whereas noise with 10 $\mathrm{mV_{pp}}$ at the third deflection stage does not alter the image contrast.

Elements	Relative noise	Absolute noise	Contrast y
Electric field control	-	2 mV_{pp}	1
	-	10 mV_{pp}	0.66
	-	20 mV_{pp}	0.23
Lens cylinders	$1 \cdot 10^{-5}$	-	1
	$5 \cdot 10^{-5}$	-	1
	$1 \cdot 10^{-4}$	-	1
Deflection plates	-	2 mV_{pp}	0.51
	-	4 mV_{pp}	0.15
	-	6 mV_{pp}	0.09

Table 4.5: Test of the final microscope design for required voltage stability. The list includes absolute noise on the electric field control and the deflection plates and relative noise on lens cylinders. The deflection plates are the most critical elements in the setup with a required voltage stability in the range of $V_{\text{noise,pp}} = 2\,\text{mV}$.

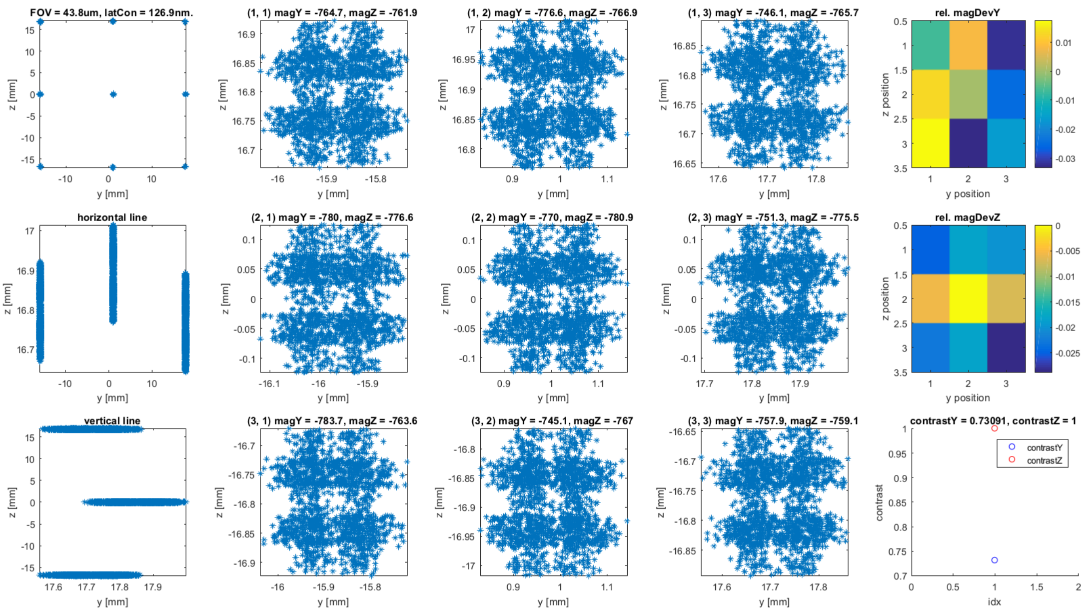

Figure 4.13: Image of a test pattern at a magnification of $M \approx 770$ with a lateral displacement of each lens cylinder of $\Delta y = 50\,\mu\text{m}$, a total displacement of the upper microscope part by 1 mm with respect to the lower part, a relative noise of $1 \cdot 10^{-4}$ on lens cylinders and drift tubes, absolute noise on every grounded part on the order of 20 mV_{pp} and absolute noise on deflection plates and electric field control on the order of 2 mV_{pp}.

Figure 4.13 shows a final test of the microscopes imaging quality at a magnification of

$M \approx 770$ under the following simulation conditions:

- Lateral displacement of each lens cylinder by $\Delta y = 50\,\mu\text{m}$
- total displacement of the upper microscope part by 1 mm with respect to the lower part
- relative noise of $1 \cdot 10^{-4}$ on lens cylinders and drift tubes
- absolute noise on ground on the order of 20 mV_{pp}
- absolute noise on deflection plates and electric field control on the order of 2 mV_{pp}

With the final simulation, requirements for the manufacturing precision, alignment precision and voltage stability to maintain a high imaging quality are given. At a magnification of $M \approx 770$ the test pattern with a lattice constant of 126.9 nm results in an image on the detector with a contrast of $C_y = 0.73$. The contrast in z-direction is not affected as mechanical misalignments are only simulated in y-direction.

5. Mechanical realization of the ion microscope

This section deals with the actual mechanical realization of the ion microscope. First, the complete setup including the mounting of different microscope parts is introduced. Then, mechanical details of the setup are outlined. Finally, the results of measuring an ion lens prototype to test the manufacturing precision are presented.

5.1. Complete setup

The actual mechanical realization of the ion microscope is illustrated as an Autodesk Inventor drawing in Figure 5.1. The upper drawing shows the whole ion microscope including the mountings for the lenses and cable guides. The microscope will be assembled in four parts where each part can be aligned separately. The first part is formed by

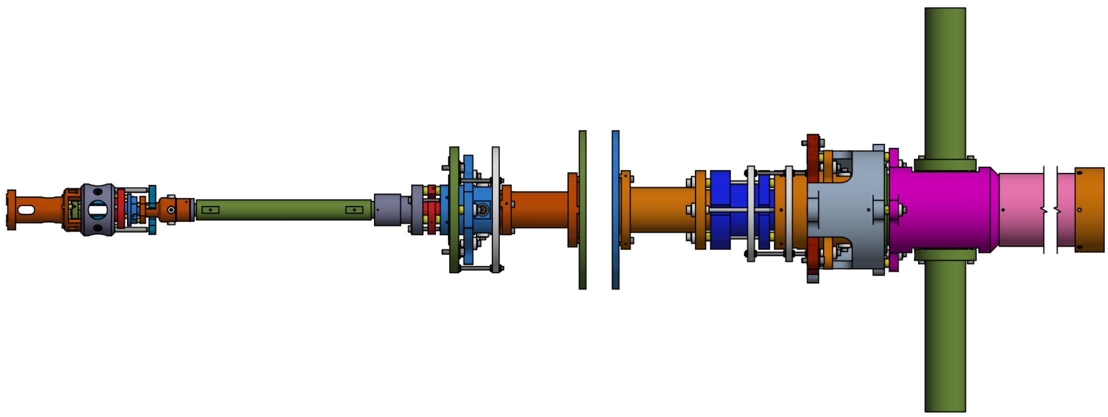

(a) Complete mechanical setup

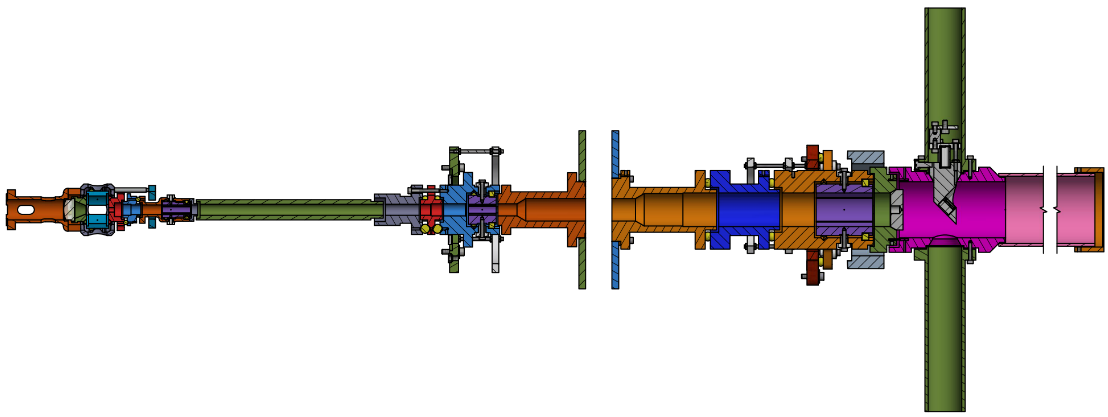

(b) Cross section of the complete mechanical setup

Figure 5.1: Top: Autodesk Inventor drawing of the complete ion microscope including lens mountings and cable guides. Bottom: Cut through the setup showing the insides of the electric field control, the mechanical realization of the deflection plates and the access for the optical mirror above the third lens.

the in-vacuum optical lens, the electric field control and the first lens with its deflection plates. It is designed in a way that it can be pre-mounted before implementing the stack into the science chamber. This ensures, apart from practical reasons, that the critical parts like electric field control and the first ion lens are intrinsically aligned. The second part of the microscope is formed by the second lens which is built onto an additional mounting ring, that can be screwed to a custom made intermediate shelf inside a vacuum tube with 150 mm diameter. The alignment of the second lens with respect to the first lens is realized by adjusting the position and angle of the mounting ring where the second lens up to the lower valve plate is connected to. The upper part of the ion microscope is also split in two independent parts, one containing the third lens and the deflection plates after the lens which has to be manufactured with high precision and the other containing the optical access with a movable in-vacuum mirror and the large drift tube leading to the detector. The part including the third lens is mounted with the help of a mounting ring that is used to adjust the position and angle of the lens with respect to the lower part. The mounting ring can be screwed into dowels that are welded into a CF-150 flange. The part containing the optical mirror has larger mechanical tolerances and is therefore mounted separately using the same technique as for the third lens with an additional mounting tube (gray element in Figure 5.1). Furthermore, it is ensured that mechanical forces originating from the linear bellow drive, used to move the optical mirror, do not affect the alignment precision of the third lens.

5.2. Ball bearing

The assembly of different electrodes is realized with high precision insulating ceramic balls made of aluminum oxide (Al_2O_3). The bearing balls are manufactured with grade 10 with a sphericity up to 0.25 µm, a nominal ball diameter tolerance of ± 1.3 µm and a maximum surface roughness (Ra) of 0.025 µm. To connect two lens cylinders, three bearing balls placed in 45°-subsidences, that are 120° apart, are used. Figure 5.2 shows a cross section of the first lens including a detail of the bearing. The three-point-bearing with the bearing balls ensures the lateral alignment of the lens electrodes. The final coaxiality was smaller than 50 µm for a testpiece manufactured in the faculty own mechanics workshop (see subsection 5.4).

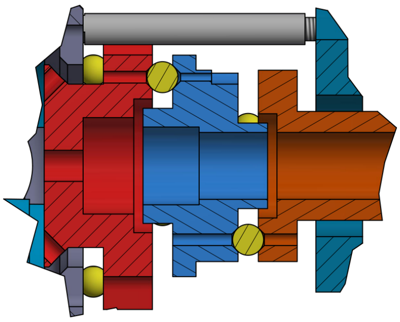

(a) Ball bearing of the first ion lens.

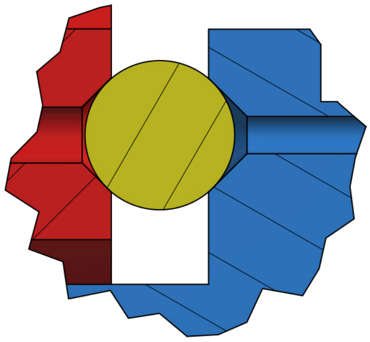

(b) Detail of the ceramic ball bearing to align individual lens cylinders.

Figure 5.2: (a) Cross section of the first ion lens to illustrate the assembly of the three lens cylinders using ceramic balls. (b) Detail of the ball bearing to assemble the ion lenses with high precision alumina (Al_2O_3) balls.

For the first lens bearing balls with a diameter of $d = 4\,\text{mm}$ are used to separate the lens cylinders with a distance of 1.2 mm. The insulating distance over the ceramic balls is chosen such that a maximum potential difference of 3.5 kV (assuming the maximum potential difference when a neighboring electrode is grounded) can be tolerated. For the second and third lens larger bearing balls can be used due to less critical spatial constraints and the balls to align and insulate neighboring lens cylinders have 8 mm diameter as well as the balls connecting the second and third lens with their respective mounting rings.

5.3. Optical mirror

To facilitate optical access for e. g. absorption imaging along the vertical axis, an optical mirror connected to a CF-16 linear bellow drive with a stroke length of maximum 100 mm has been designed. The bellow drive will be electrically insulated from the mounting of the mirror. During imaging of ions with the microscope the mirror will be 100 mm

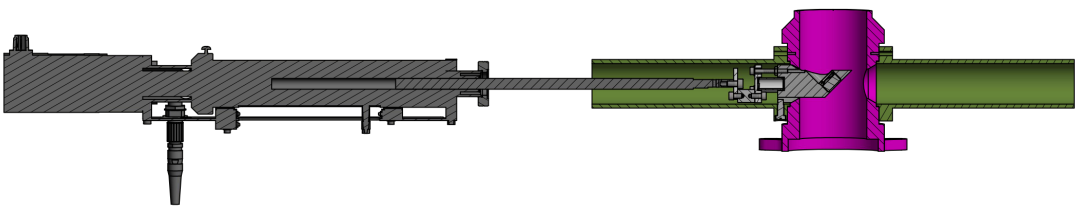

Figure 5.3: Assembly for the optical access in the vertical direction through the ion microscope. A silver mirror attached to a linear bellow drive can be moved inside the microscope to allow optical axis into the science chamber.

away from the center of the drift tube and the shielding tubes for both optical mirror and laser path will be set to the drift tube voltage of $-2.4\,\mathrm{kV}$ to avoid field inhomogeneities that could possibly disturb the ion trajectories. The correct alignment of the mirror is realized with a screw and a groove inside the mirror mount to prevent a rotation of the mirror inside the tube. The transverse position of the mirror is fixed by the conical shape of the mirror mount and the respective hole in the drift tube (see Figure 5.3).

5.4. Testing an ion lens prototype

(a) Prototype of a three-cylinder ion lens with 10 mm inner diameter.

(b) Survey of the lens prototype on a ZEISS PRISMO MTS 3D measuring machine.

Figure 5.4: (a) Prototype of a three-cylinder ion lens fabricated in the mechanical workshop of the physical institutes at the University of Stuttgart. (b) Survey of the ion lens prototype on a ZEISS PRISMO MTS 3D measuring machine. The coaxiality of the individual lens cylinders is measured as well as the cylindricity of each cylinder.

To test the achievable manufacturing precision of the mechanics workshop of the physical institutes at the University of Stuttgart, a prototype of an electrostatic three-cylinder lens has been developed. Figure 5.4(a) shows the ion lens prototype which consists of three stainless steel cylinders with an inner diameter of $d_i = 10\,\mathrm{mm}$, an outer diameter

of d_o =25 mm and a length of l = 20 mm. The distance between neighboring cylinders is 1 mm, both distance and especially the lateral alignment are realized using a three-point ball bearing with 4 mm alumina balls.
The ion lens prototype has been measured two times on a “Zeiss Prismo MTS 3D measuring machine” [2] and critical geometrical tolerances that could affect the performance of the microscope have been measured. In a first measurement, the circularity of the individual lens cylinders and their total cylindricity have been measured followed by a concentricity measurement of the stacked ion lens prototype. The concentricity thereby gives a measure for the quality of the ball bearings to connect the individual cylinders. As described in subsection 4.7, a lateral displacement of the middle lens cylinder with respect to the others which is characterized via the concentricity induces beam displacements and imaging errors such as astigmatism and coma. It was shown, that concentricities up to 50 µm are tolerable for a lens of this diameter. The results of the measurement are listed in Table 5.1.

Cylinder	Tolerance		Measured value
1	○	circularity 1	3 µm
	○	circularity 2	3 µm
	⌭	cylindricity	3 µm
2	○	circularity 1	3 µm
	○	circularity 2	2 µm
	⌭	cylindricity	3 µm
3	○	circularity 1	5 µm
	○	circularity 2	1 µm
	⌭	cylindricity	4 µm
2-1	◎	concentricity	13 µm
3-1	◎	concentricity	10 µm
3-2	◎	concentricity	23 µm

Table 5.1: Geometrical tolerances of the ion lens prototype before vacuum bake out.

The circularity of the lens cylinders was measured at two positions within each cylinder with which the cylindricity of the cylinders could be calculated. All circularities and cylindricities are thereby smaller than 5 µm. The concentricity was measured for each permutation of cylinder pairs. It can be seen that the measured concentricity with a maximum displacement of 23 µm between the second and third cylinder is well within the tolerances stated by the performed simulations.
To test the alignment of the lens cylinders for effects of thermal expansion, the lens

[2]First measurement at Gleason-Pfauter in Ludwigsburg

prototype has been implemented into a test vacuum chamber and baked out at a maximum temperature of 180° C. The temperature has been varied with a gradient of $2\,\mathrm{K\,min^{-1}}$. After the bake out, the lens prototype has been measured a second time on a 3D measuring machine to check for changes in the concentricity of the individual electrodes. Results are listed in Table 5.2. It becomes apparent that the concentricities have changed after the bake out but the maximum concentricity tolerance of 50.3 µm is still within the requirements for the precision of the ball bearings.

Cylinder	Tolerance		Measured value
2-1	◎	concentricity	50.3 µm
3-1	◎	concentricity	9.6 µm
3-2	◎	concentricity	36.1 µm

Table 5.2: Geometrical tolerances of the ion lens prototype after vacuum bake out. The temperature was increased with a gradient of $2\,\mathrm{K\,min^{-1}}$ up to a temperature of 180° C and then decreased with the same gradient until reaching room temperature.

Apart from testing the mechanical precision of the lens prototype the spark-over voltage over the ceramic insulators in vacuum has been measured with a requirement of at least 3.5 kV potential difference between two cylinders. A maximum voltage of 6 kV could be applied to the middle cylinder of the lens prototype (first and third were grounded) using a Heinzinger LNC-6000 power supply without spark-over. Higher voltages could not be applied as the maximum output voltage has been reached with 6 kV. However, the applied voltage is more than sufficient for the desired application and spark-overs over the ceramic balls at maximum potential differences of 3.5 kV at the first lens are not expected.

6. Summary and Outlook

In the scope of this thesis the design and simulation of a high-resolution ion microscope for an ultracold dual-species Rydberg experiment was accomplished.
The ion microscope was designed such that several experimental requirements are met. To avoid mechanical instabilities due to vibrations and to keep mechanical tolerances as small as possible, the ion-optical column was constructed as short as possible while still providing a magnification of at least 1000. An optimal length of 1350 mm was found. Besides, the design guarantees sufficient optical access for the beams forming the dipole trap, the photo-ionization, the excitation and the imaging of Rydberg atoms. To allow for optical access in the vertical microscope direction, a movable mirror on a linear bellow drive had to be integrated in the microscope design without disturbing the performance of the microscope. For maintenance of the detector without breaking the high-vacuum inside the experiment chamber, a valve was incorporated into the design causing the the microscope to be separated in two parts. Furthermore, an electrode geometry was designed that is on the one hand capable of compensating electric stray fields in the mV/cm regime and on the other hand offers the ability to effectively ionize and/or extract Rydberg atoms into the ion microscope. The performance of this electric field control was simulated using SIMION to determine the achievable field homogeneity in the center of the chamber.
For the efficient design and characterization of the ion microscope a comprehensive and powerful program was written to control the charged-particle simulation program SIMION. The program allows for the fully automated characterization of different geometries and scans over large parameter spaces. An optimal electrode configuration was found that provides a magnification of more than 1250 and a resolution of 100 nm in a volume of 27 µm lateral and 25 µm longitudinal extension. The ion microscope itself consists of three electrostatic three-cylinder-lenses with inner diameters of 8.6 mm, 10 mm and 30 mm, respectively. The first lens is operated asymmetrically serving as an immersion lens to put the ions on the potential of the MCP front plate at -2.4 kV. This lens is the only one that can be operated in the accelerating mode without requiring voltages exceeding 5 kV. Both second and third lens are operated symmetrically (einzel mode) and in the retarding lens mode.
The first lens produces an intermediate image which is then magnified by the second lens to produce another intermediate image. This second intermediate image is then magnified onto the detector. The extraction of Rydberg ions by pulsing of two extraction plates introduces an initial energy spread of ions over the size of the cloud. It was shown via simulations that the performance of the ion-optical column can be optimized by proper choice of intermediate image positions. The contrast on the detector was optimized by shifting the second intermediate image to compensate for this chromatic distortion. Various combinations of intermediate image positions with magnifications ranging from 80 up to 1250 are possible yielding a high contrast on the detector. The high contrast is reached over an extended depth of start of 25 µm and the maximum field of view to fill out 85 % of the active area of the detector after the magnification with the microscope. The simulations also account for non-rotationally symmetric elements in the system,

misalignments of lens cylinders and voltage instabilities of the power supplies. To compensate beam displacements, that are introduced by lateral displacements of individual lens cylinders or to compensate displacements of complete lenses with respect to each other, cylindrical deflection elements were developed and added after each lens. This distinguishes the microscope design from Stecker et al. [Ste+17] where displacements can not be compensated. Finally, the achievable resolution accounting for the mentioned imperfections in the system was determined.
Within this thesis, the actual mechanical design of the ion microscope was developed. A ball bearing with high precision ceramic balls is used for the assembly of the individual lenses. To verify that the machining tolerances of the faculty's mechanics workshop at the University of Stuttgart lie within the simulated requirements, an ion lens prototype was fabricated and measured on a 3D measuring machine. It was shown that lateral displacements were below the maximum tolerance of 50 µm. At this thime, most of the critical parts of the ion microscope are fabricated including for example the second and third lens.

Outlook: The next objective is the actual integration of the ion microscope into the experimental setup. This includes the alignment of the whole microscope as well as electrical connections inside and outside of the vacuum. To experimentally test the functionality and performance of the microscope, the optical transport from the MOT chamber to the science chamber has to be set up as well as a photo-ionization scheme which has to be implemented. However, there is also the possibility to field-ionize the Rydberg atoms. Furthermore, a heatable Lithium reservoir has to be designed and added to the existing experiment and the cooling laser system for Lithium has to be built.
With the completion of all technical tasks the study of heteronuclear Rydberg molecules can be initiated as well as the study of ultracold ion-atom scattering in the quantum regime using Rydberg molecules.

A. The cold Rydberg experiment

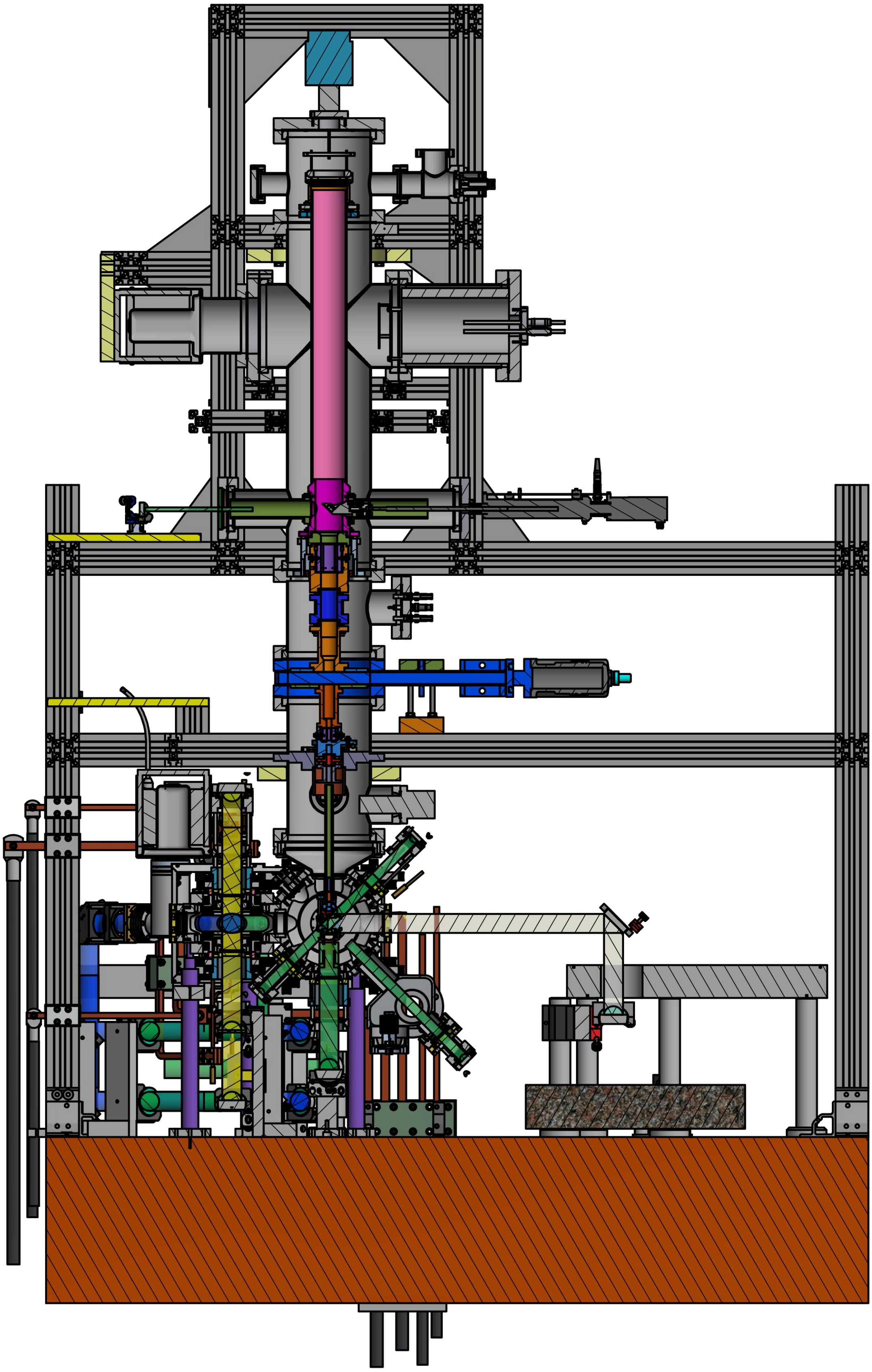

Figure A.1: Cross section of the complete setup.

B. Mechanical design of the ion microscope

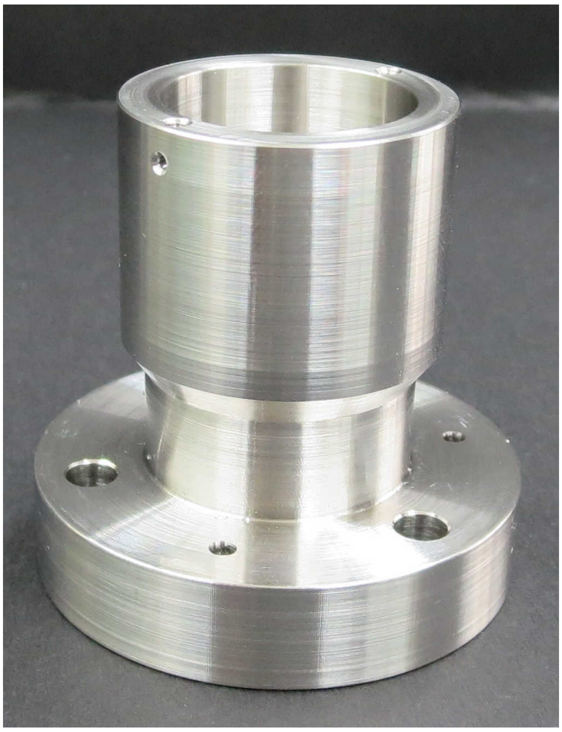

Figure B.1: First cylinder of the second lens.

Figure B.2: Second cylinder of the second lens.

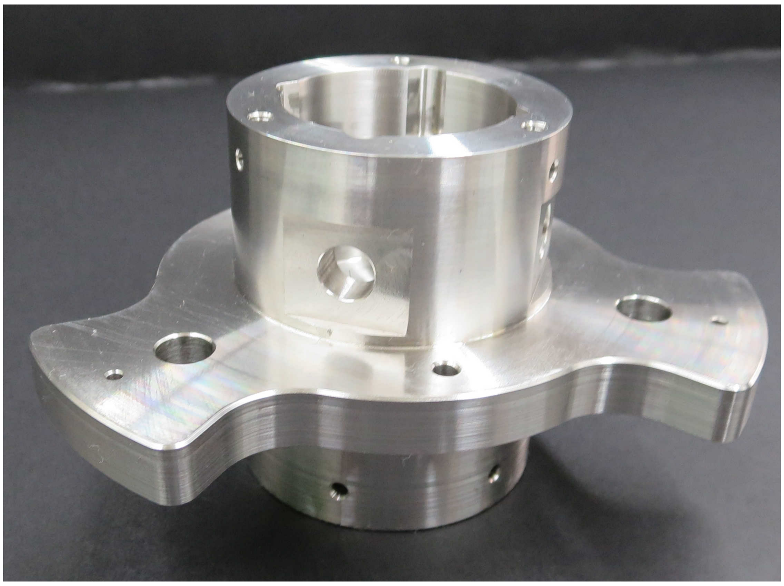

Figure B.3: Third cylinder of the second lens.

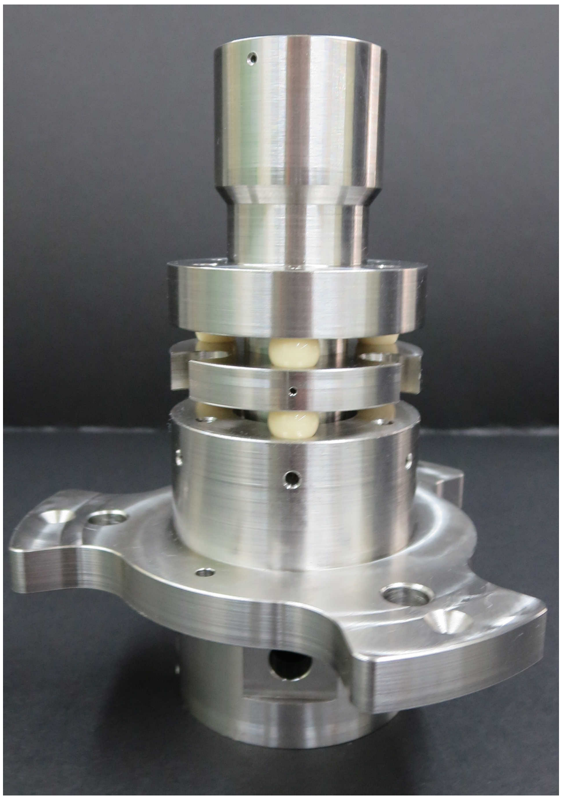

Figure B.4: Second lens assembled.

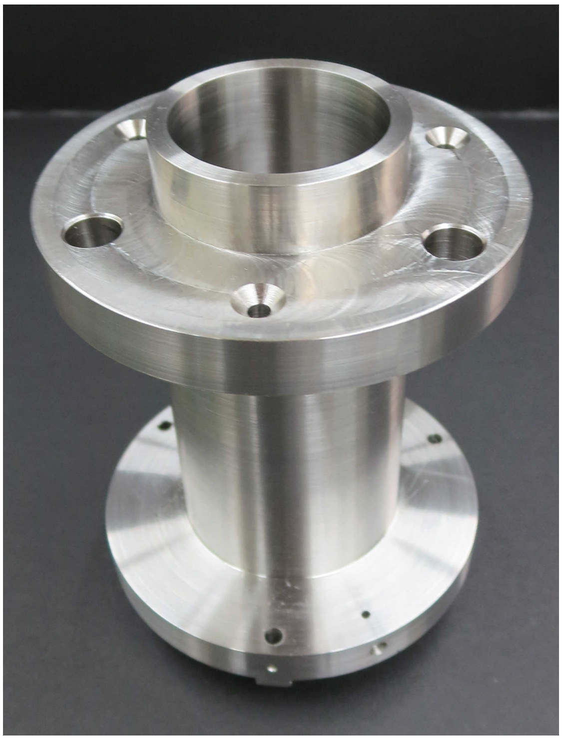

Figure B.5: First cylinder of the third lens.

Figure B.6: Second cylinder of the third lens.

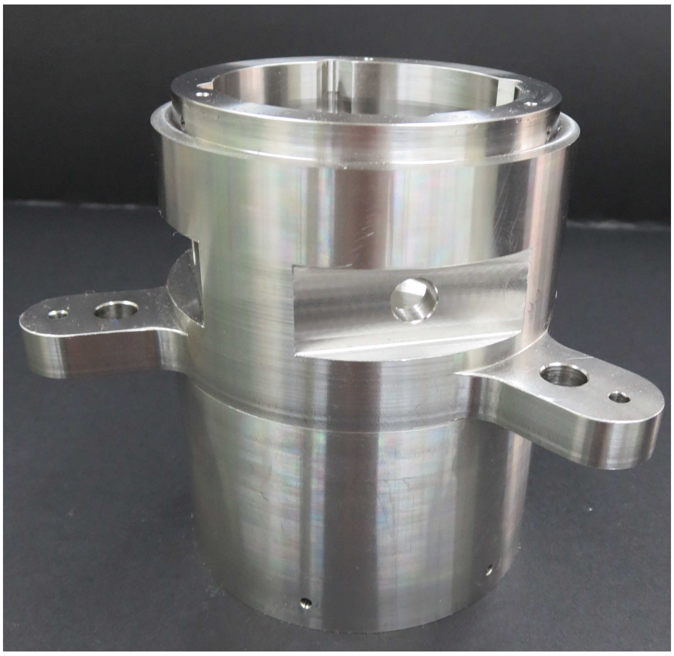

Figure B.7: Third cylinder of the third lens.

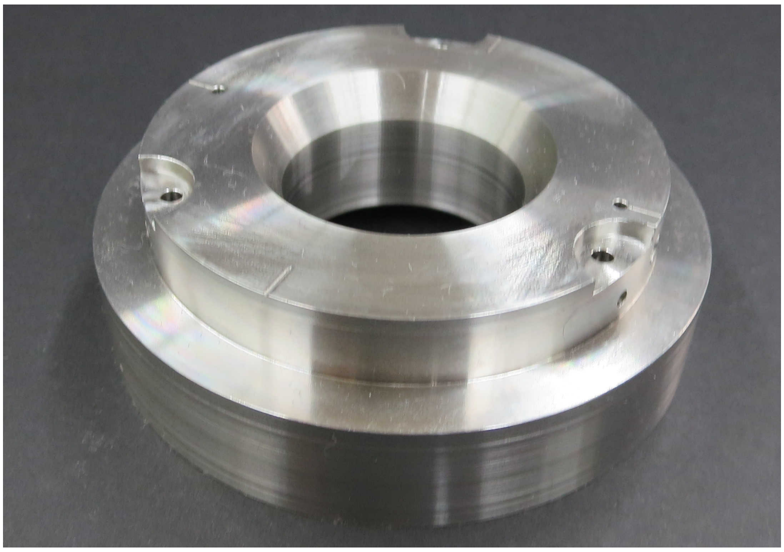

Figure B.8: Connection between third lens and drift tube for optical mirror.

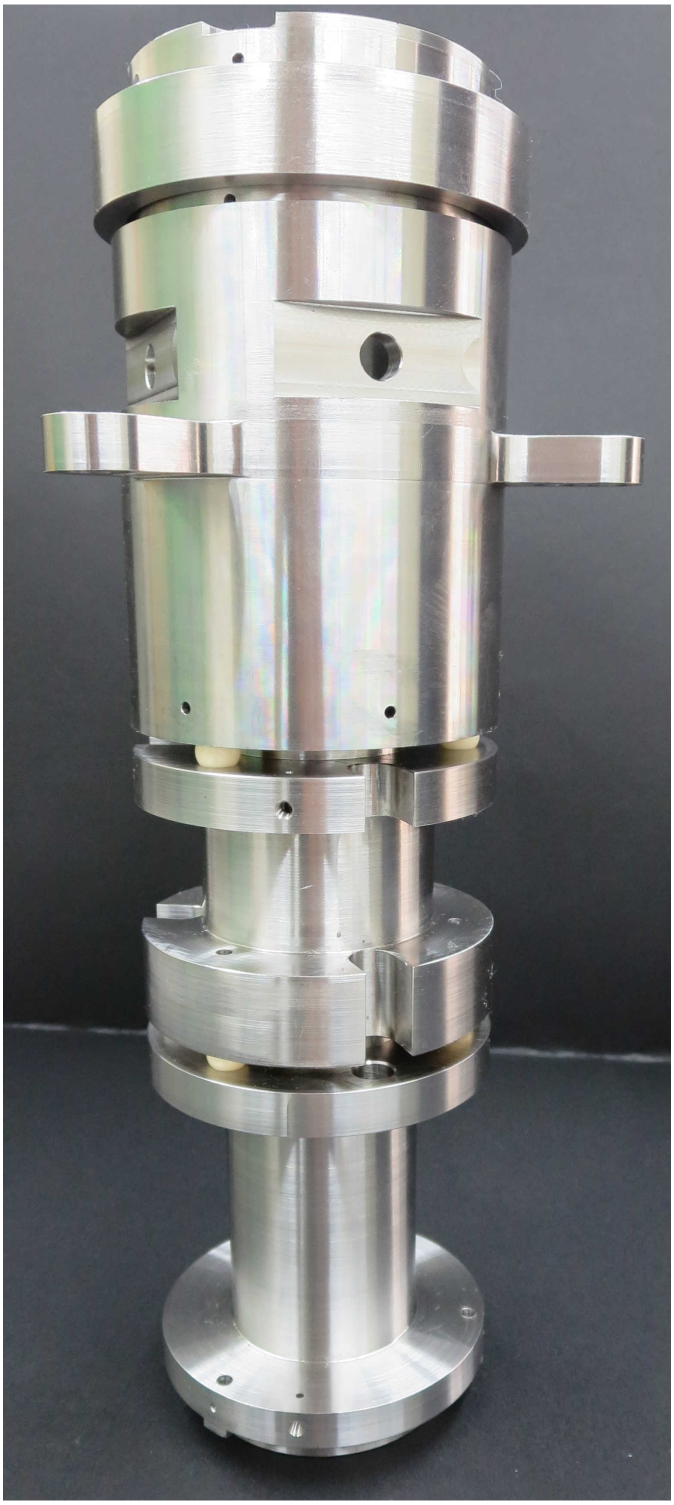

Figure B.9: Third lens assembled.

References

[And+95] M. H. Anderson, J. R. Ensher, M. R. Matthews, C. E. Wieman, and E. A. Cornell. "Observation of Bose-Einstein condensation in a dilute atomic vapor." In: *Science* **269**.5221 (1995), pp. 198–201.

[AR72] A. Adams and F. H. Read. "Electrostatic cylinder lenses II: Three element einzel lenses." In: *Journal of Physics E: Scientific Instruments* **5**.2 (1972), p. 150.

[Ard62] M. von Ardenne., ed. *Elektrostatische Ablenkung von Elektronen- oder Ionenstrahlen.* VEB Deutscher Verlag der Wissenschaften, 1962.

[Bak+09] W. S. Bakr, J. I. Gillen, A. Peng, S. Folling, and M. Greiner. "A quantum gas microscope for detecting single atoms in a Hubbard-regime optical lattice." In: *Nature* **462**.7269 (Nov. 2009), pp. 74–77.

[Bal+13] J. B. Balewski, A. T. Krupp, A. Gaj, D. Peter, H. P. Buchler, R. Low, S. Hofferberth, and T. Pfau. "Coupling a single electron to a Bose-Einstein condensate." In: *Nature* **502**.7473 (Oct. 2013), pp. 664–667.

[Ben+09] V. Bendkowsky, B. Butscher, J. Nipper, J. P. Shaffer, R. Low, and T. Pfau. "Observation of ultralong-range Rydberg molecules." In: *Nature* **458**.7241 (Apr. 2009), pp. 1005–1008.

[Ber+17] H. Bernien, S. Schwartz, A. Keesling, H. Levine, A. Omran, H. Pichler, S. Choi, A. Zibrov, M. Endres, M. Greiner, and V. Vuletic. "Probing many-body dynamics on a 51-atom quantum simulator." In: *arXiv:1707.04344* (July 2017).

[BO34] E. Brüche and S. O. *Geometrische Elektronenoptik.* Verlag von Julius Springer, 1934.

[Brü30] E. Brüche. "Strahlen langsamer Elektronen und ihre technische Anwerndung." In: *Forschung und Technik* (1930).

[BRW87] A. Benninghoven, F. Rudenauer, and H. Werner. *Secondary ion mass spectrometry: basic concepts, instrumental aspects, applications and trends.* John Wiley and Sons,New York, NY, Jan. 1987.

[Bus26] H. Busch. "Berechnung der Bahn von Kathodenstrahlen im axialsymmetrischen elektromagnetischen Felde." In: *Annalen der Physik* **25**.81 (1926), pp. 974–993.

[Bus27] H. Busch. "Über die Wirkung der Konzentrierungsspule bei der Braunschen Röhre." In: *Archiv für Elektrotechnik* **6**.18 (1927), pp. 583–594.

[Cam+17] F. Camargo, R. Schmidt, J. Whalen, R. Ding, G. Woehl Jr., S. Yoshida, J. Burgdörfer, F. Dunning, H. Sadeghpour, E. Demler, and T. Killian. "Creation of Rydberg Polarons in a Bose Gas." In: *arXiv:1706.03717* (Sept. 2017).

[CGV12] M. Cetina, A. T. Grier, and V. Vuletic. “Micromotion-Induced Limit to Atom-Ion Sympathetic Cooling in Paul Traps.” In: *Physical Review Letters* **109** (25 Dec. 2012), p. 253201.

[CKi95] G. C.King. *Chapter 5 - Electron and Ion Optics*. Ed. by F. Dunning and R. Hulet. Experimental Methods in the Physical Sciences. Elsevier Science, 1995.

[Cos+05] G. D. Costa, F. Vurpillot, A. Bostel, M. Bouet, and B. Deconihout. “Design of a delay-line position-sensitive detector with improved performance.” In: *Review of Scientific Instruments* **76**.1 (2005), p. 013304.

[Dav+95] K. B. Davis, M. .-.-O. Mewes, M. R. Andrews, N. J. van Druten, D. S. Durfee, D. M. Kurn, and W. Ketterle. “Bose-Einstein Condensation in a Gas of Sodium Atoms.” In: *Physical Review Letters* **75**.22 (Nov. 1995), pp. 3969–3973.

[DAW99] D. A. Dahl, A. D. Appelhans, and M. B. Ward. “A modular ion beam deflector.” In: *International Journal of Mass Spectrometry* **189**.1 (1999), pp. 47–51.

[DC89] J. Dalibard and C. Cohen-Tannoudji. “Laser cooling below the Doppler limit by polarization gradients: simple theoretical models.” In: *Journal of the Optical Society of America B* **6**.11 (Nov. 1989), pp. 2023–2040.

[Deh90] H. Dehmelt. “Experiments with an isolated subatomic particle at rest.” In: *Review of Modern Physics* **62** (3 July 1990), pp. 525–530.

[Dru84] I. Drummond. “The ion optics of low-energy ion beams.” In: *Vacuum* **34**.1 (1984). Vacuum Special Issue: Proceedings of the 3rd International Conference on Low Energy Ion Beams Loughborough University of Technology, UK, pp. 51–61.

[EE70] A. El-Kareh and J. El-Kareh. “VI - The Electrostatic Unipotential Lens.” In: *Electron Beams, Lenses, and Optics*. Ed. by A. El-Kareh and J. EL-Kareh. Academic Press, 1970, pp. 185–245.

[Ers95] J. Erskine. “6 - Electron Energy Analyzers.” In: *Atomic, Molecular, and Optical Physics: Charged Particles*. Ed. by F. Dunning and R. G. Hulet. Vol. 29, Part A. Methods in Experimental Physics. Academic Press, 1995, pp. 209–230.

[Gal05] T. Gallagher. *Rydberg Atoms*. Cambridge Monographs on Atomic. Cambridge University Press, 2005.

[GDS00] C. H. Greene, A. S. Dickinson, and H. R. Sadeghpour. “Creation of Polar and Nonpolar Ultra-Long-Range Rydberg Molecules.” In: *Physical Review Letters* **85**.12 (Sept. 2000), pp. 2458–2461.

[Gor+14] H. Gorniaczyk, C. Tresp, J. Schmidt, H. Fedder, and S. Hofferberth. “Single-Photon Transistor Mediated by Interstate Rydberg Interactions.” In: *Phys. Rev. Lett.* **113** (5 July 2014), p. 053601.

[Hed00] D. Heddle. *Electrostatic Lens Systems.* Institute of Physics Publishing, 2000.

[HH14] A. Härter and J. Hecker Denschlag. "Cold atom–ion experiments in hybrid traps." In: *Contemp. Phys.* **55**.1 (2014), pp. 33–45.

[Hig+05] J. M. Higbie, L. E. Sadler, S. Inouye, A. P. Chikkatur, S. R. Leslie, K. L. Moore, V. Savalli, and D. M. Stamper-Kurn. "Direct Nondestructive Imaging of Magnetization in a Spin-1 Bose-Einstein Gas." In: *Physical Review Letters* **95** (5 July 2005), p. 050401.

[HK70] D. W. O. Heddle and M. V. Kurepa. "The focal properties of three-element electrostatic electron lenses." In: *Journal of Physics E: Scientific Instruments* **3**.7 (1970), p. 552.

[HL67] K.-J. Hanszen and R. Lauer. "Chapter 2.2 - Electrostatic Lenses." In: *Focusing of Charged Particles.* Ed. by A. Septier. Academic Press, 1967, pp. 251–307.

[Hoe+13] A. L. Hoendervanger, D. Clément, A. Aspect, C. I. Westbrook, D. Dowek, Y. J. Picard, and D. Boiron. "Influence of gold coating and interplate voltage on the performance of chevron micro-channel plates for temporally and spatially resolved single particle detection." In: *Review of Scientific Instruments* **84**.2 (2013), p. 023307.

[Hon+16] R. Hong, A. Leredde, Y. Bagdasarova, X. Fléchard, A. García, P. Müller, A. Knecht, E. Liénard, M. Kossin, M. Sternberg, H. Swanson, and D. Zumwalt. "High accuracy position response calibration method for a micro-channel plate ion detector." In: *Nuclear Instruments and Methods in Physics Research Section A: Accelerators, Spectrometers, Detectors and Associated Equipment* **835** (2016), pp. 42–50.

[HP84] D. W. O. Heddle and N. Papadovassilakis. "The magnification behaviour of a five-element electrostatic lens." In: *Journal of Physics E: Scientific Instruments* **17**.7 (1984), p. 599.

[HRB76] E. Harting, F. Read, and J. Brunt. *Electrostatic lenses.* Elsevier Scientific Pub. Co., 1976.

[HRo09] H. H.Rose. *Geometrical Charged-Particle Optics.* Springer, 2009.

[Kar+15] T. Karpiuk, M. Brewczyk, K. Rzążewski, A. Gaj, J. B. Balewski, A. T. Krupp, M. Schlagmüller, R. Löw, S. Hofferberth, and T. Pfau. "Imaging single Rydberg electrons in a Bose–Einstein condensate." In: *New Journal of Physics* **17**.5 (2015), p. 053046.

[KDM99] W. Ketterle, D. Durfee, and D. M. Stamper-Kurn. "Making, probing and understanding Bose-Einstein condensates." In: *arXiv:cond-mat/9904034* (Apr. 1999).

[KDS99] W. Ketterle, D. Durfee, and D. M. Stamper-Kurn. “Making, probing and understanding Bose-Einstein condensates.” In: *Bose-Einstein Condensation in Atomic Gases*. Ed. by S. Stringari, M. Inguscio, and C. E. Wieman. Proceedings of the International School of Physics “Enrico Fermi” Course CXL. IOS Press, 1999, pp. 67–176.

[Kha+16] R. I. Khakimov, B. M. Henson, D. K. Shin, S. S. Hodgman, R. G. Dall, K. G. H. Baldwin, and A. G. Truscott. “Ghost imaging with atoms.” In: *Nature* **540**.7631 (Dec. 2016). Letter, pp. 100–103.

[KR32] M. Knoll and E. Ruska. “Beitrag zur geometrischen Elektronenoptik. I.” In: *Annalen der Physik* **404**.5 (1932), pp. 607–640.

[KZ08] W. Ketterle and M. W. Zwierlein. “Making, probing and understanding ultracold Fermi gases.” In: *Ultracold Fermi Gases*. Ed. by M. Inguscio, W. Ketterle, and C. Salomon. Proceedings of the International School of Physics “Enrico Fermi”, Course CLXIV. IOS Press, 2008, pp. 95–287.

[Lab+16] H. Labuhn, D. Barredo, S. Ravets, S. de Léséleuc, T. Macrì, T. Lahaye, and A. Browaeys. “Tunable two-dimensional arrays of single Rydberg atoms for realizing quantum Ising models.” In: *Nature* **534**.7609 (June 2016). Letter, pp. 667–670.

[Lei+03] D. Leibfried, R. Blatt, C. Monroe, and D. Wineland. “Quantum dynamics of single trapped ions.” In: *Review of Modern Physics* **75** (1 Mar. 2003), pp. 281–324.

[Lie49] G. Liebmann. “Measured Properties of Strong "Unipotential" Electron Lenses.” In: *Proceedings of the Physical Society. Section B* **62**.4 (1949), p. 213.

[Lie89] H. Liebl. “Ion Probe Microscopy.” In: *Advances in Optical and Electron Microscopy* **11** (1989), pp. 101–151.

[Löw+12] R. Löw, H. Weimer, J. Nipper, J. B. Balewski, B. Butscher, H. P. Büchler, and T. Pfau. “An experimental and theoretical guide to strongly interacting Rydberg gases.” In: *Journal of Physics B: Atomic, Molecular and Optical Physics* **45**.11 (2012), p. 113001.

[MD08] D. Manura and D. Dahl. *SIMION (R) 8.0 User Manual*. Scientific Instrument Services, Jan. 2008.

[ME15] E. R.-C. for Microscopy and S. with Electrons (ER-C) et al. “FEI Titan G3 50-300 PICO.” In: *Journal of large-scale research facilities* **1**.A34 (2015).

[Mep+10] R. Meppelink, R. A. Rozendaal, S. B. Koller, J. M. Vogels, and P. van der Straten. “Thermodynamics of Bose-Einstein-condensed clouds using phase-contrast imaging.” In: *Physical Review A* **81** (5 May 2010), p. 053632.

[Mun88] E. Munro. “Finite difference programs for computing tolerances for electrostatic lenses.” In: *Journal of Vacuum Science & Technology B: Microelectronics Processing and Phenomena* **6**.3 (1988), pp. 941–948.

[Orl08] J. Orloff. *Handbook of Charged Particle Optics*. CRC Press, 2008, pp. 161–208.

[OS79] J. Orloff and L. W. Swanson. "An asymmetric electrostatic lens for field-emission microprobe applications." In: *Journal of Applied Physics* **50**.4 (1979), pp. 2494–2501.

[Pau90] W. Paul. "Electromagnetic traps for charged and neutral particles." In: *Review of Modern Physics* **62** (3 July 1990), pp. 531–540.

[Pey+12] T. Peyronel, O. Firstenberg, Q.-Y. Liang, S. Hofferberth, A. V. Gorshkov, T. Pohl, M. D. Lukin, and V. Vuletic. "Quantum nonlinear optics with single photons enabled by strongly interacting atoms." In: *Nature* **488**.7409 (Aug. 2012), pp. 57–60.

[Pic32] J. Picht. "Beiträge zur Theorie der geometrischen Elektronenoptik." In: *Annalen der Physik* **407**.8 (1932), pp. 926–964.

[PPM82] J. V. Prodan, W. D. Phillips, and H. Metcalf. "Laser Production of a Very Slow Monoenergetic Atomic Beam." In: *Physical Review Letters* **49**.16 (Oct. 1982), pp. 1149–1153.

[RAS71] F. H. Read, A. Adams, and J. R. Soto-Montiel. "Electrostatic cylinder lenses. I. Two element lenses." In: *Journal of Physics E: Scientific Instruments* **4**.9 (1971), p. 625.

[Rea83] F. H. Read. "A 'movable' electrostatic lens." In: *Journal of Physics E: Scientific Instruments* **16**.7 (1983), p. 636.

[Rid78] G. H. N. Riddle. "Electrostatic einzel lenses with reduced spherical aberration for use in field-emission guns." In: *Journal of Vacuum Science and Technology* **15**.3 (1978), pp. 857–860.

[RT90] D. Roy and D. Tremblay. "Design of electron spectrometers." In: *Reports on Progress in Physics* **53**.12 (1990), p. 1621.

[Sch+13] A. Schwarzkopf, D. A. Anderson, N. Thaicharoen, and G. Raithel. "Spatial correlations between Rydberg atoms in an optical dipole trap." In: *Physical Review A* **88** (6 Dec. 2013), p. 061406.

[Sch+15] P. Schauß, J. Zeiher, T. Fukuhara, S. Hild, M. Cheneau, T. Macri, T. Pohl, I. Bloch, and C. Gross. "Crystallization in Ising quantum magnets." In: *Science* **347**.6229 (2015), pp. 1455–1458.

[Sch+16] M. Schlagmüller, T. C. Liebisch, H. Nguyen, G. Lochead, F. Engel, F. Böttcher, K. M. Westphal, K. S. Kleinbach, R. Löw, S. Hofferberth, T. Pfau, J. Pérez-Rios, and C. H. Greene. "Probing an Electron Scattering Resonance using Rydberg Molecules within a Dense and Ultracold Gas." In: *Phys. Rev. Lett.* **116** (5 Feb. 2016), p. 053001.

[Sch+17] T. Schmid, C. Veit, N. Zuber, R. Löw, T. Pfau, M. Tarana, and M. Tomza. "Rydberg molecules for ion-atom-scattering in the ultracold regime." In: *arXiv:1709.10488v1* (2017).

[Sch36] O. Scherzer. “Über einige Fehler von Elektronenlinsen.” In: *Zeitschrift für Physik* **101**.9 (1936), pp. 593–603.

[Sch47] O. Scherzer. “Sphärische und chromatische Korrektur von Elektronenlinsen.” In: *Optik* 2 (1947), pp. 114–132.

[Ste+17] M. Stecker, H. Schefzyk, J. Fortágh, and A. Günther. “A high resolution ion microscope for cold atoms.” In: *New Journal of Physics* **19**.4 (2017), p. 043020.

[SUD05] O. Sise, M. Ulu, and M. Dogan. “Multi-element cylindrical electrostatic lens systems for focusing and controlling charged particles.” In: *Nuclear Instruments and Methods in Physics Research Section A: Accelerators, Spectrometers, Detectors and Associated Equipment* **554**.1 (2005), pp. 114–131.

[SUD07] O. Sise, M. Ulu, and M. Dogan. “Aberration coefficients of multi-element cylindrical electrostatic lens systems for charged particle beam applications.” In: *Nuclear Instruments and Methods in Physics Research Section A: Accelerators, Spectrometers, Detectors and Associated Equipment* **573**.3 (2007), pp. 329–339.

[SWM10] M. Saffman, T. G. Walker, and K. Mølmer. “Quantum information with Rydberg atoms.” In: *Review of Modern Physics* **82** (3 Aug. 2010), pp. 2313–2363.

[TKH90] C. Trager-Cowan, S. M. Kay, and D. W. O. Heddle. “Multiple-element electrostatic lenses: I. The five-element lens.” In: *Measurement Science and Technology* **1**.8 (1990), p. 738.

[Tom+17] M. Tomza, K. Jachymski, R. Gerritsma, A. Negretti, T. Calarco, Z. Idziaszek, and P. S. Julienne. “Cold hybrid ion-atom systems.” In: *arXiv:1708.07832v1* (2017).

[Tra+90] C. Trager-Cowan, R. B. Miller, S. M. Kay, and D. W. O. Heddle. “Multiple-element electrostatic lenses: II. A multiple disc lens.” In: *Measurement Science and Technology* **1**.8 (1990), p. 747.

[Vin60] J. Vine. “Numerical investigation of a range of unipotential electron lenses.” In: *British Journal of Applied Physics* **11**.9 (1960), p. 408.

[Wei60] W. Weitsch. “Über eine Zusatzlinse zur Kompensation der Farbabhängigkeit der Vergrößerung im elektostatischen Elektronenmikroskop.” In: *4th International Conference on Electron Microscopy* (1960), pp. 48–53.

[Win13] D. J. Wineland. “Nobel Lecture: Superposition, entanglement, and raising Schrödinger’s cat.” In: *Review of Modern Physics* **85** (3 July 2013), pp. 1103–1114.

[ZW18] D. Zhang and S. Willitsch. “Cold ion chemistry.” In: *Cold Chemistry: Molecular Scattering and Reactivity Near Absolute Zero*. Ed. by O. Dulieu and A. Osterwalder. The Royal Society of Chemistry, 2018.

Danksagung

An dieser Stelle möchte ich noch einigen Personen danken, die zum Gelingen dieser Arbeit beigetragen haben. Dies sind im Besonderen:

- **Prof. Dr. Tilman Pfau**, der mir die Möglichkeit gegeben hat nach meiner Bachelorarbeit auch meine Masterarbeit am 5. Physikalischen Institut zu schreiben.
- **Prof. Dr. Gert Denninger** in seiner Funktion als Mitberichter dieser Arbeit.
- **Thomas Schmid**, **Christian Veit** und **Nicolas Zuber** für die tolle Zusammenarbeit an diesem großen und zeitaufwändigen Projekt und die großartige Unterstützung vor allem beim Entwickeln des mechanischen Designs und der Erstellung unzähliger technischer Zeichnungen.
- **Dr. Robert Löw** für die netten Diskussionen und hilfreichen Ratschläge.
- **Felix Schiefer** vom Institut für Maschinenelemente für die Möglichkeit zur Vermessung des Linsenprototypen.
- Allen Mitarbeitern vom 5. Physikalischen Institut für die tolle Atmosphäre am Institut.